A pion-argon cross section measurement in the ProtoDUNE-SP experiment with cosmogenic muon calibration

by

Ajib Paudel

MSc, Tribhuvan University, Nepal, 2012

AN ABSTRACT OF A DISSERTATION

submitted in partial fulfillment of the
requirements for the degree

DOCTOR OF PHILOSOPHY

Department of Physics
College of Arts and Sciences

KANSAS STATE UNIVERSITY
Manhattan, Kansas

2021

Abstract

Neutrinos are tiny mysterious fundamental particles with small cross sections. Through neutrino physics, scientists across the world are trying to answer many intriguing questions about nature such as the dominance of matter over antimatter, CP violation in the lepton sector, number of supernovas in the early universe, etc. Detection of neutrinos requires massive particle detectors and intense neutrino beam owing to their small cross section. Deep Underground Neutrino Experiment (DUNE) is a next-generation neutrino experiment that is planned to start taking data beginning in 2026. DUNE will consist of 4 massive detectors, the first of which will be using single-phase liquid argon time projection chamber (LArTPC) technology. The ProtoDUNE-SP experiment is a prototype of the DUNE built at the CERN neutrino platform and uses the same detector technology that will be used in DUNE first module. The ProtoDUNE-SP experiment collected months of test beam and cosmic ray data beginning in September 2018. It was built to provide a testbed for the installation of detector parts for DUNE, showing long-term stability of the detector, understanding detector response for different test beam particles (including protons, pions, electrons, kaons, muons), and measurement of hadron-argon cross sections.

When a particle passes through LArTPC electron-ion pairs are produced. To reconstruct the position and energy of a particle passing through the medium knowledge of ionization electron drift velocity is essential. The electron drift velocity is distorted by an excess positive charge built up in the detector, known as space charge. This study discusses a novel technique for measuring the ionization electron drift velocity using cosmic-ray muons. The technique uses tracks that travel the entire drift distance of the TPC for drift velocity determination. Secondly, the study discusses a method for converting the charge deposited into energy. The method is carried out in two steps. In the first step detector response for energetic cosmic ray muons crossing the entire the TPC is used to make the charge deposition uniform throughout the TPC, and in the second step stopping cosmic-ray muons are used for determining the energy scale. Finally, the study discusses a pion-argon cross section measurement based on reweighting of Monte Carlo simulations using J. Calcutt's Geant4Reweight framework. Neutrinos cannot be directly detected; they are identified based on the interaction products. Pions are a common interaction product in a neutrino interaction. For precise modeling of neutrino event generators, it is essential to understand the pion-argon interaction. Pion-argon cross section measurement serves as an important input for neutrino interaction models. The results of the pion-argon total reaction cross section using the Geant4 reweighting technique are found to be in good agreement with Geant4 predictions. The many studies carried out in the ProtoDUNE-SP experiment will be useful for current and future neutrino experiments using LArTPC technology including ICARUS, MicroBooNE, DUNE.

A pion-argon cross section measurement in the ProtoDUNE-SP experiment with cosmogenic muon calibration

by

Ajib Paudel

MSc, Tribhuvan University, Nepal

A DISSERTATION

submitted in partial fulfillment of the
requirements for the degree

DOCTOR OF PHILOSOPHY

Department of Physics
College of Arts and Sciences

KANSAS STATE UNIVERSITY
Manhattan, Kansas

2021

Approved by:

Major Professor
Glenn Horton-Smith

Copyright

Abstract

Neutrinos are tiny mysterious fundamental particles with small cross sections. Through neutrino physics, scientists across the world are trying to answer many intriguing questions about nature such as the dominance of matter over antimatter, CP violation in the lepton sector, number of supernovas in the early universe, etc. Detection of neutrinos requires massive particle detectors and intense neutrino beam owing to their small cross section. Deep Underground Neutrino Experiment (DUNE) is a next-generation neutrino experiment that is planned to start taking data beginning in 2026. DUNE will consist of 4 massive detectors, the first of which will be using single-phase liquid argon time projection chamber (LArTPC) technology. The ProtoDUNE-SP experiment is a prototype of the DUNE built at the CERN neutrino platform and uses the same detector technology that will be used in DUNE first module. The ProtoDUNE-SP experiment collected months of test beam and cosmic ray data beginning in September 2018. It was built to provide a testbed for the installation of detector parts for DUNE, showing long-term stability of the detector, understanding detector response for different test beam particles (including protons, pions, electrons, kaons, muons), and measurement of hadron-argon cross sections.

When a particle passes through LArTPC electron-ion pairs are produced. To reconstruct the position and energy of a particle passing through the medium knowledge of ionization electron drift velocity is essential. The electron drift velocity is distorted by an excess positive charge built up in the detector, known as space charge. This study discusses a novel technique for measuring the ionization electron drift velocity using cosmic-ray muons. The technique uses tracks that travel the entire drift distance of the TPC for drift velocity determination. Secondly, the study discusses a method for converting the charge deposited into energy. The method is carried out in two steps. In the first step detector response for energetic cosmic ray muons crossing the entire the TPC is used to make the charge deposition uniform throughout the TPC, and in the second step stopping cosmic-ray muons are used for determining the energy scale. Finally, the study discusses a pion-argon cross section measurement based on reweighting of Monte Carlo simulations using J. Calcutt's Geant4Reweight framework. Neutrinos cannot be directly detected; they are identified based on the interaction products. Pions are a common interaction product in a neutrino interaction. For precise modeling of neutrino event generators, it is essential to understand the pion-argon interaction. Pion-argon cross section measurement serves as an important input for neutrino interaction models. The results of the pion-argon total reaction cross section using the Geant4 reweighting technique are found to be in good agreement with Geant4 predictions. The many studies carried out in the ProtoDUNE-SP experiment will be useful for current and future neutrino experiments using LArTPC technology including ICARUS, MicroBooNE, DUNE.

Table of Contents

List of Figures

List of Tables

Acknowledgments

It is my pleasure to acknowledge the people who in different ways helped me get one step closer to my doctorate. I would like to thank Kansas State University for providing me the opportunity to work on a doctorate in Physics.

I consider myself very fortunate to have Professor Glenn Horton-Smith as my supervisor. He has been very kind and helpful throughout my Ph.D. years. Ph.D. is often presented as a dreadful experience, however, for me, it has been a pleasant and memorable 6 years, largely because of having a wonderful supervisor. It has always been fun to work with him. He is an inspiration for anyone who knows him. He always respects everyone, is always calm and composed and makes everyone feel they capable of doing great things.

I would like to thank Professor Tim Bolton for accepting me in the neutrino Physics group at K-State and providing continuous support and guidance. I would like to thank Dr. Tingjun Yang from whom I learned a great deal of physics and technical aspects of research during my stay at Fermilab. His guidance and belief in me immensely helped me grow as a better researcher and made me more confident in my work. I consider myself lucky to have been able to collaborate with him for most of my thesis works and many other projects. I am grateful to Dr. Flavio Cavanna who always supported my work and shared his ideas which I could implement in my work. His consistent encouragement always motivated me to put in the extra effort. I am thankful to my Ph.D. supervisory committee members and chairperson for their precious time.

I owe a deep sense of gratitude to the collaborators from the ProtoDUNE-SP experiment without whom this study won't have been possible. I would like to specially mention Dr. Heng-Ye Liao, Jake Calcutt, and Dr. Hans Wenzel for their help in the pion-argon cross

section study.

It is my privilege to thank my Professors from St. Edmunds college and Tribhuvan University from where I completed my BSc and MSc in Physics respectively. I would like to thank my school teachers.

Finally, I would like to thank my family members and close friends who have been by my side through thick and thin.

Dedication

To my father whom I can proudly say: *“now I have the highest degree one can earn in physics”.*

Chapter 1

Theoretical background

1.1 Introduction

Neutrinos are the most abundant particles in the Universe, yet the most mysterious ones. They rarely interact with matter and thus carry with them information from the beginning of the cosmos. Through many experiments in the field of neutrino physics, scientists across the globe are trying to answer the most intriguing questions in nature including why the Universe is made of matter and not antimatter, are there more types of neutrinos awaiting discovery, do protons decay, and many more. In this chapter, I will discuss the Standard Model[1–3] of particle physics and the role of neutrinos in the Standard Model. I will further discuss neutrino interactions and the significance of hadron-argon cross section measurement for neutrino science study.

1.2 The Standard Model of particle physics

The Standard Model is a result of the theories and discoveries of thousands of physicists since the 1930s. The latest addition to the model is the Higgs boson which was discovered in 2012. In particle physics, an elementary or a fundamental particle is the one that is not composed of other particles. There are 17 fundamental particles described in the Standard

Model. The Standard Model includes the electromagnetic, strong, and weak forces and their carrier particles. When it comes to the force between fundamental particles, gravity is negligibly weak.

Figure 1.1 shows the constituents of the Standard Model. The constituents of the Standard model can be broadly classified as fermions and bosons based on their spin. Fermions in the Standard Model include 3 generations of leptons and quarks. The lightest and the most stable particles make up the first generation, whereas the second and the third generation are comprised of less stable and heavier particles.

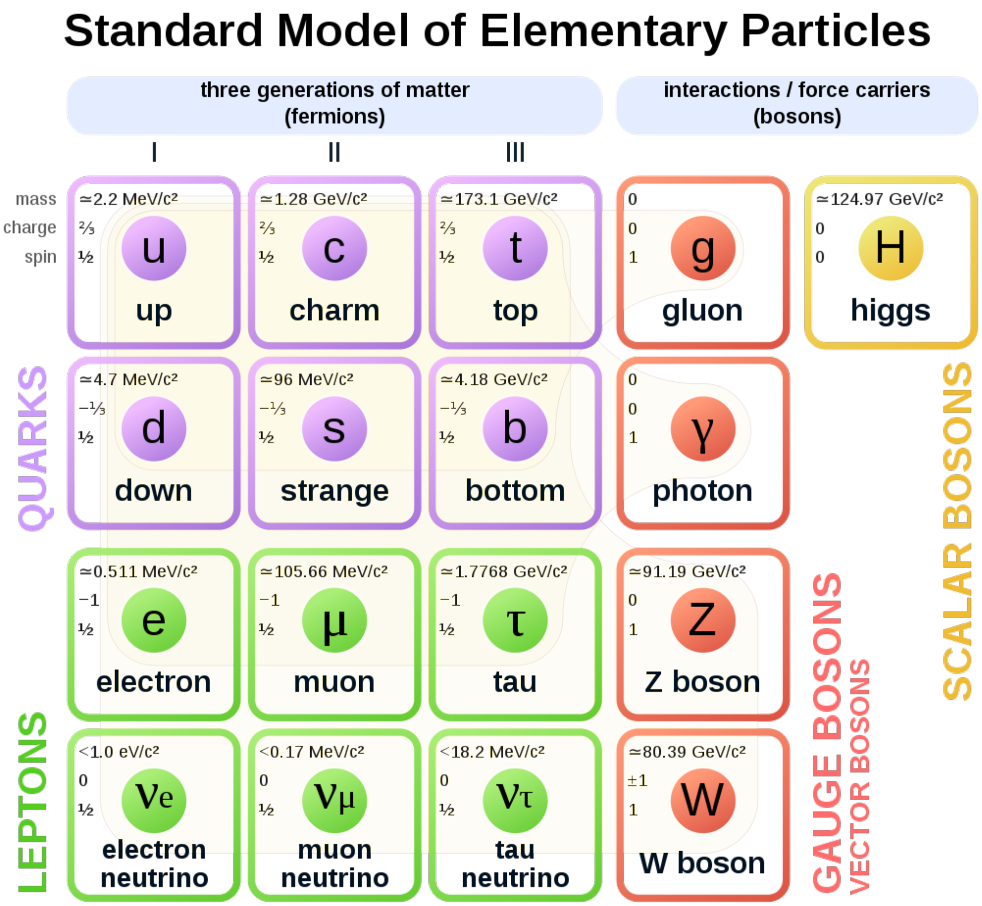

Figure 1.1: Elementary particles of the Standard Model. The figure is taken from Wikipedia[2].

Bosons include the force carriers. There are four fundamental forces in the Universe;

gravity being the weakest of all is excluded from the Standard Model. The strong and the weak nuclear forces have a short range, while the electromagnetic force has an infinite range. The strong nuclear force is the strongest of all, followed by the electromagnetic force and the weak nuclear force. Each fundamental force has its boson as a charge carrier. The strong nuclear force is carried by the “gluons”, the electromagnetic force is carried by the “photons” and the weak nuclear force is carried by the “W and Z bosons”. The latest addition to the Standard Model, the Higgs boson, was observed in the ATLAS and the CMS experiments at CERN’s Large Hadron Collider in 2012[4;5]. The Higgs boson is the exchange particle of the Higgs field which generates particle mass.

The Standard Model although gives the best description of the subatomic world, it does not give a complete picture. There are many questions the Standard Model does not adequately explain including gravity, dark matter, dark energy, neutrino masses, matter-antimatter asymmetry. There are many ongoing or proposed experiments such as Deep Underground Neutrino Experiment[6] (DUNE) which attempts to address some of the questions that the Standard Model cannot explain. Neutrinos play a major role in addressing questions beyond the Standard Model.

1.3 Neutrinos and their properties

The neutrino was first postulated by Wolfgang Pauli in December 1930 to explain the energy spectrum of beta decay. They are very important in cosmology and particle physics as they can travel cosmological distances without being absorbed thus carrying information from the edge of the Universe. Unlike other leptons in the Standard Model, they cannot be directly observed. They are detected only through their weak interactions. They come in three flavours, namely electron neutrino (ν_e), muon neutrino (ν_μ) and tau neutrino (ν_τ). The flavor of neutrino is identified by the flavor of the charged lepton produced in the neutrino interaction. In the next subsection, I will briefly discuss weak interaction, the only type of interaction that neutrinos exhibit.

1.3.1 The Weak Interaction

The electromagnetic, weak, and strong interaction can be understood in the framework of the Standard Model. The weak interaction is a short range force, and much weaker than the strong or the electromagnetic force for the same range. It is the only interaction that can change the flavor of quarks and violate parity-symmetry. For an interaction to occur there should be an exchange of a boson or force carriers between the interacting particles. In a weak interaction typically two fermions exchange one of three types of force carriers, namely W^+, W^- or Z bosons. These bosons are much heavier than the interacting particles which is an unusual feature explained by the Higgs mechanism.

Weak isospin and weak hypercharge: For an interaction to occur the particles must be carrying the charge of the interaction. For instance, only quarks carry the color, the charge of quantum chromodynamics, and hence only quarks can exhibit strong interaction. Only electrically charged particles can undergo electromagnetic interaction by the exchange of photons. Similarly, for weak interactions to occur the interacting particles must possess a property called weak isospin (T_3). All the fermions in the Standard Model carry weak isospin, making all of them eligible for the weak interaction. However, there are certain selection rules for the interaction to be allowed. All the left-handed fermi particles in the Standard Model have a weak isospin value of $+1/2$ or $-1/2$, and all right-handed fermi particles have isospin of 0. Similarly, all the left-handed fermi anti-particles have 0 isospin and all the right-handed fermi anti-particles have $+1/2$ or $-1/2$ weak isospin. Table 1.1 shows the weak isospin for fermions in the standard model, their antiparticles will have opposite weak isospin. In any interaction, weak isospin value must be conserved.

Table 1.1: Weak isospin T_3 for left handed fermions in the standard model

Fermion symbol	Weak Isospin
e^-, μ^-, τ^-, d, s, b	$-1/2$
ν_e, ν_μ, ν_τ, u, c, t	$+1/2$

Weak interactions can be classified into “charged-current weak interaction” and “neutral-current weak interaction”. The charged current weak interaction is mediated by $W^{\pm}$ boson and the neutral current interaction is mediated by Z boson. In a typical charged current neutrino interaction, a charged lepton (with charge ±1) can absorb a W boson (with charge ∓1) and get converted into a corresponding charge-less neutrino. Whereas, in neutral-current interaction, a lepton or a quark interacts via Z boson.

1.3.2 Neutrino physics so far

Neutrinos are never directly observed, they are detected based on the charged lepton involved in the interaction. For instance, when a ν_μ interact with matter a charged muon is produced which infers the interacting particle being a ν_μ. The Standard Model treats neutrinos as massless particles and does not predict the mixing of neutrino flavor. Both neutrino non-zero mass and mixing have been shown experimentally.

Solar neutrino problem: A large flux, $2 \times 10^{38}\ \nu_e/sec$, of electron neutrinos are produced during nuclear fusion in the Sun. Although neutrinos have a very small cross section, they can be detected by a sufficiently large detector. Several distinct processes are contributing to the nuclear fusion in the Sun. The main fusion process is what is known as the pp cycle[1], which occurs in 3 steps:

$$\begin{aligned} p + p &\rightarrow D + e^{+} + \nu_e \\ D + p &\rightarrow {}^{3}_{2}He + \gamma \\ {}^{3}_{2}He + {}^{3}_{2}He &\rightarrow {}^{4}_{2}He + p + p \end{aligned}$$

However, the energy of the neutrinos produced through the pp cycle is very low, $E_\nu < 0.5\ MeV$ so they are very difficult to detect. The neutrinos originating from the β decay of ${}^{8}B$ are the highest energy solar neutrinos with up to 15 MeV energies. The first experiment to detect the solar neutrinos took place in the Homestake Gold Mine in Lead, South

Dakota in the late 1960s (popularly known as Homestake experiment[7]). The experiment used a radiochemical technique to measure the flux of the solar neutrinos. 615 tonnes of perchloroethylene (C_2Cl_4), a dry-cleaning fluid, was placed 1478 meters underground. An electron neutrino can interact with ^{37}Cl atom transforming it into a radioactive isotope ^{37}Ar, which can be extracted and counted.

$$\nu_e + {}^{37}Cl \rightarrow {}^{37}Ar + e^-$$

The rate of neutrino interaction detected was only 0.48 ± 0.04 per day while the expected neutrino interaction rate was 1.7 interactions per day. This apparent deficit in the number of solar neutrinos detected is known as the solar neutrino problem[8].

Results from the Homestake experiment and other solar neutrino experiments such as Super-Kamiokande[9] demonstrated the deficit of electron neutrinos coming from the Sun. Another solar neutrino experiment, the Sudbury Neutrino Observatory (SNO) experiment[10] in Canada was designed to measure ν_e and the total neutrino flux. The results from the SNO experiment shows that the total flux of neutrinos from the Sun is consistent with the theoretical prediction, but instead of just ν_e, there is large ν_μ and/or ν_τ component. However, the fusion reactions in the Sun can only produce ν_e, so the detection of ν_μ or ν_τ provides evidence of neutrino flavor transformations. Neutrino flavor transformations can be explained by the phenomenon of neutrino oscillation.

Neutrino oscillation in three flavor paradigm: Neutrino oscillations requires non-zero neutrino masses and flavor mixing in the lepton sector. The Standard Model predicts neutrinos as mass-less. Understanding the mechanism behind neutrino mass is among the unresolved mysteries of particle physics and which leads us to explore physics beyond the Standard model. The three-flavor paradigm requires introducing distinct non-zero mass states for at least two neutrinos. The neutrino mass eigenstates are defined as ν_1, ν_2, ν_3. They are distinct from the neutrino weak or flavor eigenstates ν_e, ν_μ, ν_τ. The flavor eigenstates are related to the mass eigenstates by a 3×3 unitary matrix U[1],

$$\begin{pmatrix} \nu_e \\ \nu_\mu \\ \nu_\tau \end{pmatrix} = \begin{pmatrix} U_{e1} & U_{e2} & U_{e3} \\ U_{\mu 1} & U_{\mu 2} & U_{\mu 3} \\ U_{\tau 1} & U_{\tau 2} & U_{\tau 3} \end{pmatrix} \begin{pmatrix} \nu_1 \\ \nu_2 \\ \nu_3 \end{pmatrix} \tag{1.1}$$

Here the matrix U is referred to as neutrino mixing matrix or the Potecorvo-Maki-Nakagawa-Sakata (PMNS) matrix and is given by,

$$\begin{pmatrix} U_{e1} & U_{e2} & U_{e3} \\ U_{\mu 1} & U_{\mu 2} & U_{\mu 3} \\ U_{\tau 1} & U_{\tau 2} & U_{\tau 3} \end{pmatrix} = \begin{pmatrix} c_{12}c_{13} & s_{12}c_{13} & s_{13}e^{-i\delta} \\ -s_{12}c_{23} - c_{12}s_{23}s_{13}e^{i\delta} & c_{12}c_{23} - s_{12}s_{23}s_{13}e^{i\delta} & s_{23}c_{13} \\ s_{12}s_{23} - c_{12}c_{23}s_{13}e^{i\delta} & -c_{12}s_{23} - s_{12}c_{23}s_{13}e^{i\delta} & c_{23}c_{13} \end{pmatrix} \tag{1.2}$$

Here $s_{ij} = sin\theta_{ij}$ and $c_{ij} = cos\theta_{ij}$. The three flavor neutrino oscillation can be explained in terms of three mixing angles $(\theta_{12}, \theta_{23}, \theta_{13})$, three mass squared splittings $(\Delta m^2_{21}, \Delta m^2_{31}, m^2_{32})$ only 2 of which are independent, and CP violating factor δ. Experiments such as Super-Kamiokande, KamLAND, T2K, NOvA, and Daya Bay have firmly established the existence of neutrino oscillations and have measured most elements of the 3x3 PMNS matrix, a notable exception being δ_{CP}. The detailed results can be found in[11].

1.4 Beyond Standard Model

Neutrino mass and neutrino oscillation can not be explained within the framework of the Standard model. This leads to the search for physics beyond the Standard model that could explain the anomalies without interfering with the rest of the Standard model. In this section, we discuss a few open questions in neutrino physics that the current and future neutrino experiments aim to resolve.

Majorana or Dirac[12]: If a particle and its antiparticle are distinct they are called Dirac particles otherwise they are called Majorana particles. In 1957, physicists showed the neutrinos have left-handed spin i.e., the direction of spin and motion are opposite and the anti-neutrinos have right-handed spin i.e., the direction of spin and the direction of motion is the same. This indicates neutrinos are Dirac particles. However as neutrinos have mass, it is possible to change the observer's frame of reference so that the direction of motion is reversed. For different observers, there will be ambiguity in the direction of motion of neutrinos thus causing ambiguity in the handedness of the neutrinos. If neutrinos are Majorana particles, there is a possibility of observing neutrinoless β decay.

Sterile neutrinos: Sterile neutrinos are hypothetical neutrinos that interact via gravity unlike other neutrinos in the Standard Model which interact only via the weak interaction force[13;14]. They are proposed to be neutrinos with right-handed chirality. Their existence is theoretically well-motivated since all other known fermions have been observed with both left and right chirality. In the mid-1990s, the Liquid Argon Scintillator Detector[15] (LSND) located at Los Alamos National Laboratory in New Mexico found some evidence of sterile neutrinos but the results could not be replicated and were set aside. Another experiment MiniBooNE[16] at Fermi National Accelerator Laboratory located near Chicago, has found some evidence of sterile neutrinos again. The search for sterile neutrinos is an active area of particle physics.

CP violation in Lepton Sector: The C-symmetry or charge conjugation symmetry means the symmetry of physical laws under charge-conjugation, where charge conjugation refers to the changing of signs of all charges relevant to the forces, not just the electric charge. The P-symmetry refers to the invariance of physical laws under parity inversion i.e., changing the sign of all three spatial coordinates in 3D. CP-symmetry is a product of two transformations (C and P) which was initially thought to be an absolute symmetry. It was discovered that the weak force did not follow C or P symmetry. Physicists then came up with the idea of CP symmetry where both the charge and parity are transformed together and considered it to be the absolute symmetry in nature. For example, if we take the mirror image of left-handed neutrinos and transform the charge we get right-handed anti-neutrinos, which exists. CP violation was first discovered in kaons[17]. Amongst the elementary particles, CP violation has been observed in quarks, however, it has never been observed in neutrinos[18]. Through various ongoing and future experiments such as DUNE, physicists are searching for experimental evidence of CP violation in the lepton sector. The existence of CP violation allows the distinction between matter and antimatter which is important to explain the observed imbalance of matter over antimatter in the Universe[19].

Neutrino mass hierarchy: With the discovery of neutrino oscillation it is now established that the neutrinos have mass, but the masses of three types (m_1, m_2 and m_3) are different. Solar neutrino oscillation experiments have determined the difference of the square of masses m_1 and m_2 ($\Delta m^2_{12} = m^2_1$-m^2_2)[20]. Furthermore, the atmospheric neutrino experiments have determined the difference of the square of masses m_1 and m_3 ($\Delta m^2_{13} = m^2_1$-m^2_3). However, the signs of Δm^2_{12} and Δm^2_{13} is unknown, this is known as neutrino mass hierarchy problem. It is unknown if $m_2 - m_1 < m_3 - m_1$ (Normal mass hierarchy) or $m_2 - m_1 > m_3 - m_1$ (Inverted mass hierarchy). The mass hierarchy affects of the sensitivity of CP violation measurements and also the sensitivity to determine if neutrinos and anti-neutrinos are the same particle or different.

1.5 Neutrino interactions

The neutrinos rarely interact with matter and there is no direct way of identifying neutrinos. Neutrinos are identified from their interaction products, so it is very important to understand how neutrino interacts with matter. The neutrino interactions can be broadly classified into two categories:

- **Neutral-current neutrino interaction:** In a neutral current (NC) interaction, the neutrino before and after the interaction does not change. An example of a NC interaction is,

$$\nu_\mu + N \rightarrow \nu_\mu + hadrons \tag{1.3}$$

where N is the nucleus. These kind of interactions are mediated by Z bosons.

- **Charged-current neutrino interaction:** In a charged current (CC) neutrino interaction, the neutrino transforms into a lepton of the same flavor as incident neutrino. It is mediated by $W^{\pm}$ boson. Following are some of the examples of charged current neutrino interaction:

  Quasi-Elastic Scattering (QE):

  $$\nu_l + n \rightarrow l^- + p \tag{1.4}$$

  Resonant pion production:

  $$\nu_\mu + N \rightarrow \mu^- + \Delta^{++} \rightarrow \mu^- + p + \pi^+ \tag{1.5}$$

  $$\nu_\mu + N \rightarrow \mu^- + \Delta^{+} \rightarrow \mu^- + n + \pi^+ \tag{1.6}$$

  Deep Inelastic scattering (DIS): It refers to the head-on collision between a neutrino and a parton inside the nucleon. In such interactions hadronization occurs with subsequent abundant production of mesons and nucleons.

  Pions are very common interaction products of neutrino interactions in the energy range significant to the DUNE experiment. In the next section, I will discuss the interaction of pions with Ar.

1.6 Pion-argon interaction

The energy and the flavor of a neutrino are determined based on the identity and energy of products of a neutrino interaction. Pions are the final state products of most neutrino interactions significantly above the pion as evident from equations 1.3, 1.5 and 1.6 . To simulate the neutrino interaction in argon we need to know how the interaction products travel through the medium as well as their behavior inside the target nucleus. Different Monte Carlo event generators have been used to simulate the neutrino interactions in the liquid Ar including GENIE[21], Geant4[22], FLUKA[23] etc. One of the major ingredients for any neutrino generator to be successful is its ability to model the interaction of the products of a neutrino interaction. The models of interaction are often validated with experimental data or tuned based on the experimental results. However, the study of the pion-argon cross section has been rare or non-existent. LArIAT (Liquid Argon In A Test Beam) experiment at Fermilab has done some study of the total pion-argon cross section in the momentum range of 0.1-1.1 GeV/c[24;25]. No other experimental studies of the pion cross section have been done previously. In ProtoDUNE-SP experiment[26] we have collected π^+ beam data in the momentum range of 1-7 GeV/c, which provides a great opportunity for the experimental measurement of pion-argon cross section in a wide energy range. Below is a classification of different π^+-nucleus interaction channels[25]:

1. **Pion Absorption, σ_{abs}:** In this interaction there is no pion in the final state as shown in figure 1.2 (bottom). The interactions are listed below:

$$\begin{aligned} \pi^+(nn) &\rightarrow np\ (Two\ body\ absorption) \\ \pi^+(nnn) &\rightarrow nnp\ (Three\ body\ absorption) \\ \pi^+(nnp) &\rightarrow npp\ (Three\ body\ absorption) \\ \pi^+(nnnp) &\rightarrow ppnn\ (Multi\ body\ absorption) \end{aligned}$$

2. **Charge Exchange, σ_{cex}:** In charge exchange interaction the final state has a neutral pion (π^0) as shown in figure 1.2 (top),

$$\pi^+ \ + n \rightarrow \Delta^+ \rightarrow \pi^0 + p$$

3. **Inelastic Scattering, σ_{inel}:** In inelastic interaction, pion interacts with a nucleus

knocking out one or more nucleons:

$$\pi^+ \ + {}^{40}Ar \rightarrow \pi^+ + {}^{39}Ar^* \ + \ n$$

$$\pi^+ \ + {}^{40}Ar \rightarrow \pi^+ + {}^{39}Cl^* \ + \ p$$

$$\pi^+ \ + {}^{40}Ar \rightarrow \pi^+ + {}^{38}Cl^* \ + \ np$$

4. **Pion Production,** $\sigma_{\pi prod}$**:** In this interaction, final state has more than 1 pion:

$$\pi^+ \ + \ N \rightarrow \geq \ 2\pi \ + \ nucleons$$

5. **Elastic Scattering,** σ_{el}**:** In elastic interaction the system is in ground state after the interaction:

$$\pi^+ \ + N \ \rightarrow \ \pi^+ \ + \ N$$

For inclusive cross section study, the interaction of π^+ with the nucleus listed above can be broadly classified into two channels, the elastic channel comprising the elastic interaction (σ_{el}) and the reaction channel comprising of the first four categories of interaction listed above. Electromagnetic processes and weak processes such as pion decay are excluded in the cross section study.

$$\sigma_{reac} \ = \ \sigma_{abs} \ + \ \sigma_{cex} \ + \ \sigma_{inel} \ + \ \sigma_{\pi prod} \tag{1.7}$$

1.6.1 Previous results of pion-nucleus cross section

Figure 1.4 shows the results of pion-nucleus cross section in the resonance region[27] for various nuclei.

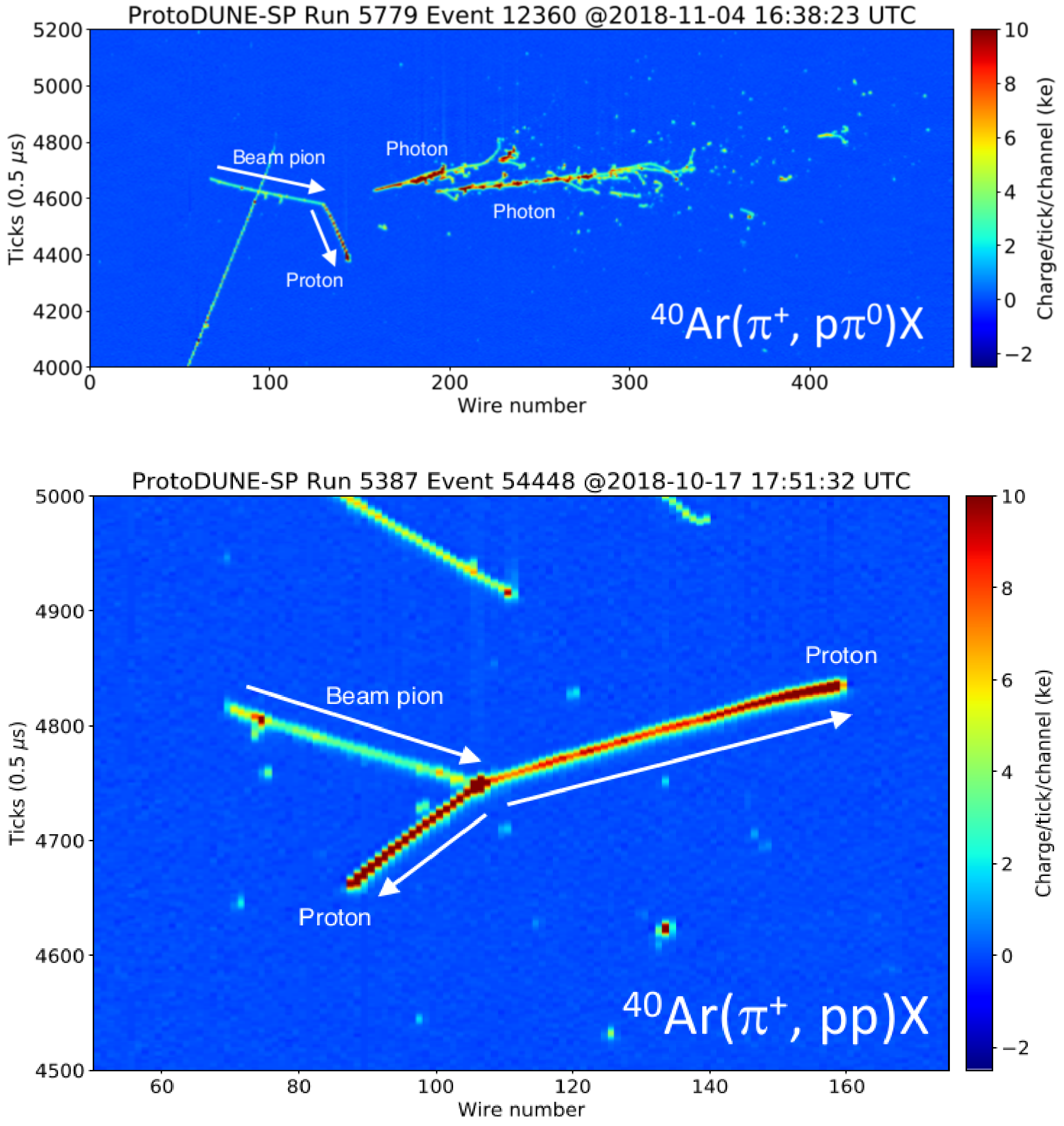

Figure 1.2: Figure shows candidate pion charge exchange interaction (top) and candidate pion absorbtion interaction (bottom) for ProtoDUNE-SP experiment [26]. Photons themselves do not leave any track, however they produce electron showers based on which they can be identified.

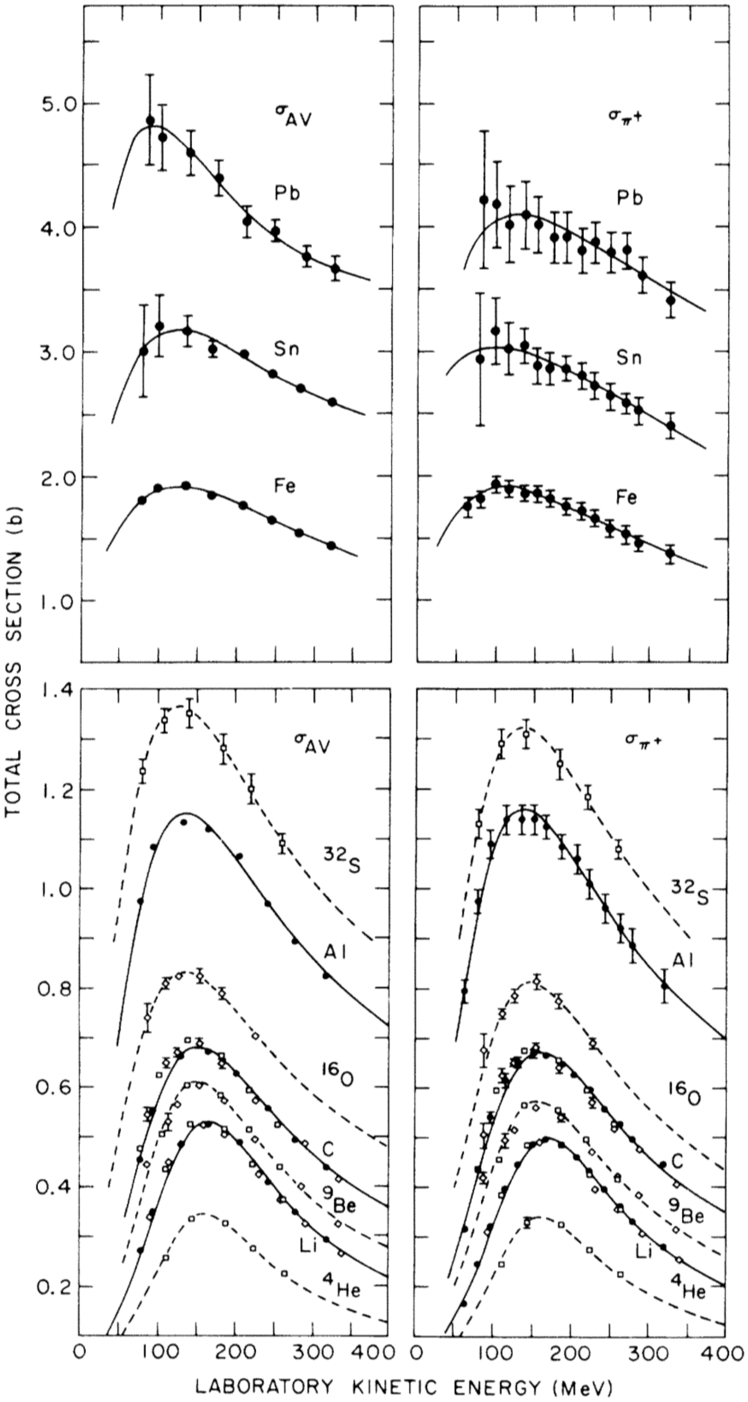

Figure 1.3: Pion-nucleus total cross section on various nuclei in the resonance region. Left plots are for $\sigma_{AV}=\frac{\sigma_{\pi^+}+\sigma_{\pi^-}}{2}$ and right plots are for σ_{π^+}. The plots are taken from[27].

1.6.2 Geant4 prediction of π^+ cross section on argon:

As there has not been any previous direct measurement of π^+ cross section on argon, Geant4 uses the results of pion cross section on other nuclei and predicts the pion-argon cross section based on the cross section dependence on atomic mass (A). Figure 1.4 shows the dependence of pion-nucleus cross section on A for different interaction channels[28]. Figure 1.5 shows the Geant4 v10.5 prediction for π^+-argon cross section. The results of ProtoDUNE-SP analysis of π^+-argon cross section is discussed in chapter 5.

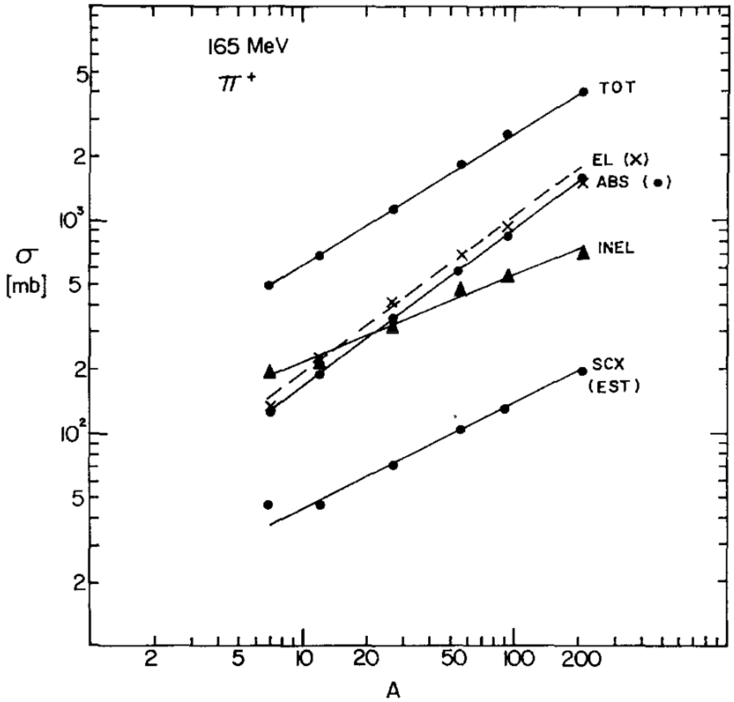

Figure 1.4: Pion-nucleus cross section for different interaction channel vs atomic mass (A). The figure is taken from[28].

Figure 1.6 shows the π^+ total elastic and reaction cross section on carbon. The data for the plot is taken from[29;30], the Geant4 cross section prediction is taken from[31].

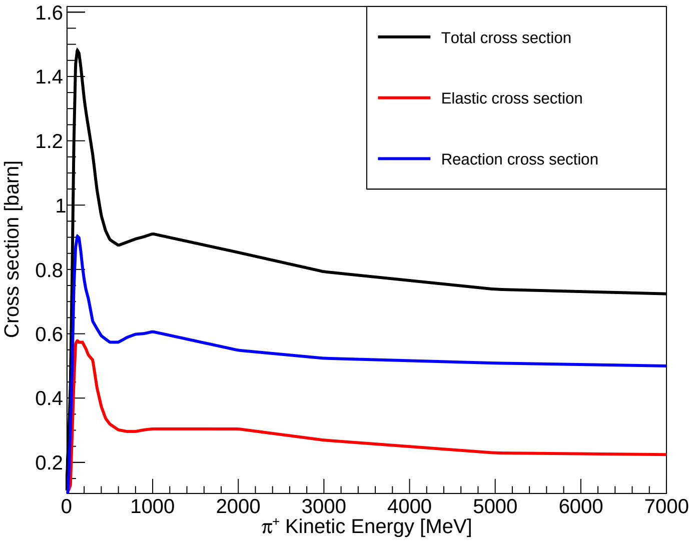

Figure 1.5: Geant4 v10.5 π^+-argon cross section prediction.

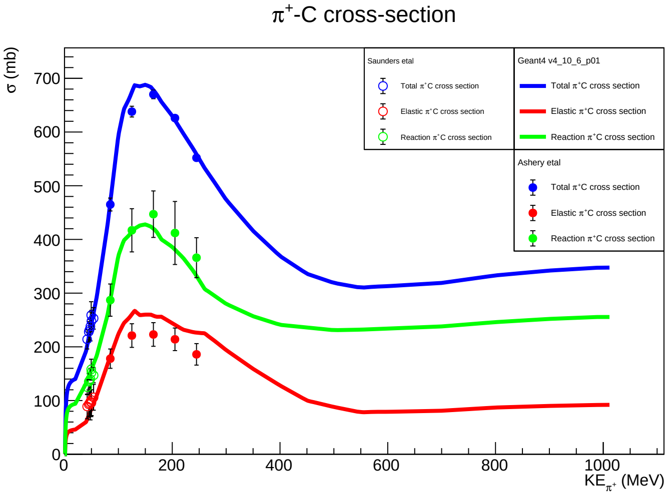

Figure 1.6: The plot shows π^+ cross section on carbon. The data points are taken from the references[29;30]

Chapter 2

DUNE and ProtoDUNE-SP

Our current knowledge of particle physics does not explain some of the most intriguing questions in particle physics. The Deep Underground Neutrino Experiment (DUNE[32–35]) is a leading-edge, international experiment for neutrino science and seeks to make groundbreaking discoveries to answer the following questions[6]:

- Why is the early Universe dominated by matters rather than antimatter? Could neutrinos be the reason that the Universe is made of matter rather than antimatter? DUNE aims to explore the phenomenon of neutrino oscillations and through the mechanism of charge-parity violation (CP violation) DUNE aims to discover matter-antimatter asymmetries in neutrino-mixing. More precise measurement of neutrino mixing parameters and determination of neutrino mass ordering may reveal new fundamental symmetries of nature.

- Do protons decay? This could reveal a relationship between the stability of matter and the Grand Unification theory.

- DUNE's gigantic size will allow observation of thousands of neutrinos from core-collapse supernovae in the Milky Way galaxy. Neutrinos emitted in the supernova burst can potentially carry with them the information of the evolution of the Universe. This would allow a rare opportunity for us to investigate the processes inside a newly-formed neutron star and an opportunity to witness the birth of a black hole. DUNE will run for a few decades during which there is every possibility of one or more supernovae burst occurring in the Milky way galaxy.

DUNE has around 1300 collaborators from over 32+ countries and 200+ institutions. It is to be hosted by the Fermi National Accelerator Laboratory (Fermilab) near Chicago, in Illinois, and is funded by the U.S. Department of Energy. Figure 2.1 shows the major components of the DUNE experiment. A high-intensity neutrino source is generated from a megawatt-class proton accelerator at Fermilab, a near detector installed just downstream of the neutrino beam and massive neutrino far detectors 1.5 km underground and 1300 km away from Fermilab at the Sanford Underground Research Facility (SURF) in South Dakota. The DUNE Far Detector (DUNE FD) will consist of four LArTPC modules, each of which will have an active volume of at least 10 kt. The total liquid argon volume in the cryostat will be ≈17.5 kt. Two different LArTPC technologies are planned to be used for the first two DUNE FD modules: the single-phase (SP) technology in which the medium inside the cryostat is liquid argon and the dual-phase (DP) in which a layer of gaseous argon above liquid argon is used. The first DUNE FD module will certainly use single-phase liquid argon time projection technology, however, the technology to be used for the second DUNE FD module is not yet fixed. Considering the scale of the experiment and the amount of resources that will be used for the experiment, a full-scale prototype for both the single-phase and dual-phase technology has been built at the CERN neutrino platform. Figure 2.2 shows the two DUNE prototypes, the ProtoDUNE-SP[36] and the ProtoDUNE-DP[37] detectors built at the CERN neutrino platform. Here, I will describe briefly the ProtoDUNE-SP and ProtoDUNE-DP prototypes, the rest of the chapter will focus on the ProtoDUNE-SP experiment on which my analysis is based.

- In the SP technology the ionization charge drifts in the liquid argon under the action of an electric field, figure 2.3 (left). There are 3 read-out planes, two induction, and a collection plane. The technology was pioneered in the ICARUS project[39]. The tech-

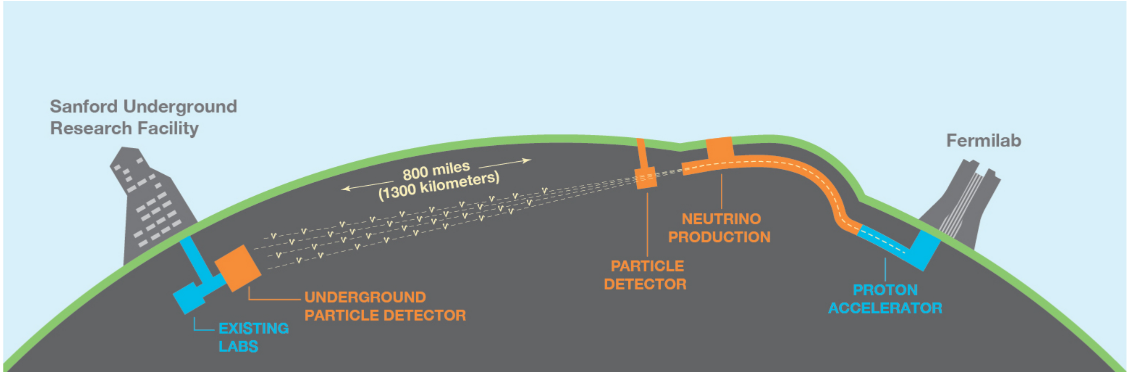

Figure 2.1: Schematic diagram for Long Baseline Neutrino Experiment[6]

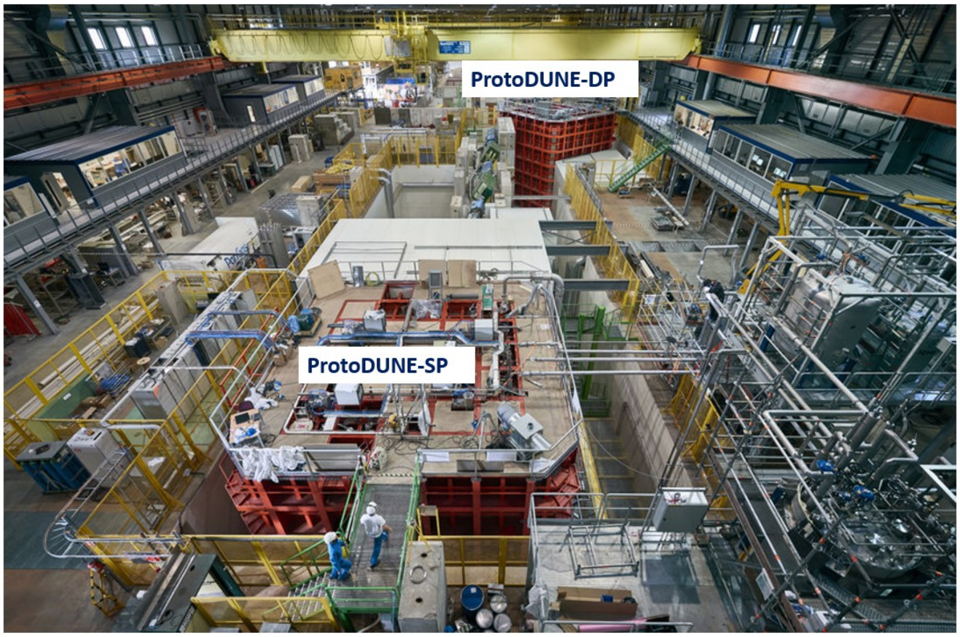

Figure 2.2: ProtoDUNE-SP and ProtoDUNE-SP detector built at the CERN neutrino platform.

nology is matured and has been successfully used in many neutrino science experiments including LArIAT[40], ArgoNeut[41], MicroBOONE[42].

- In the DP technology we use a vertical drift where the ionization charge drifts upwards in liquid argon and is transferred to a layer of gaseous argon above the liquid, figure 2.3 (right). This technology was pioneered by the WA105 DP demonstrator collaboration[37] at CERN. The signal is amplified in the gas phase using large electron multipliers. A big advantage of signal amplification is we no more need the stringent

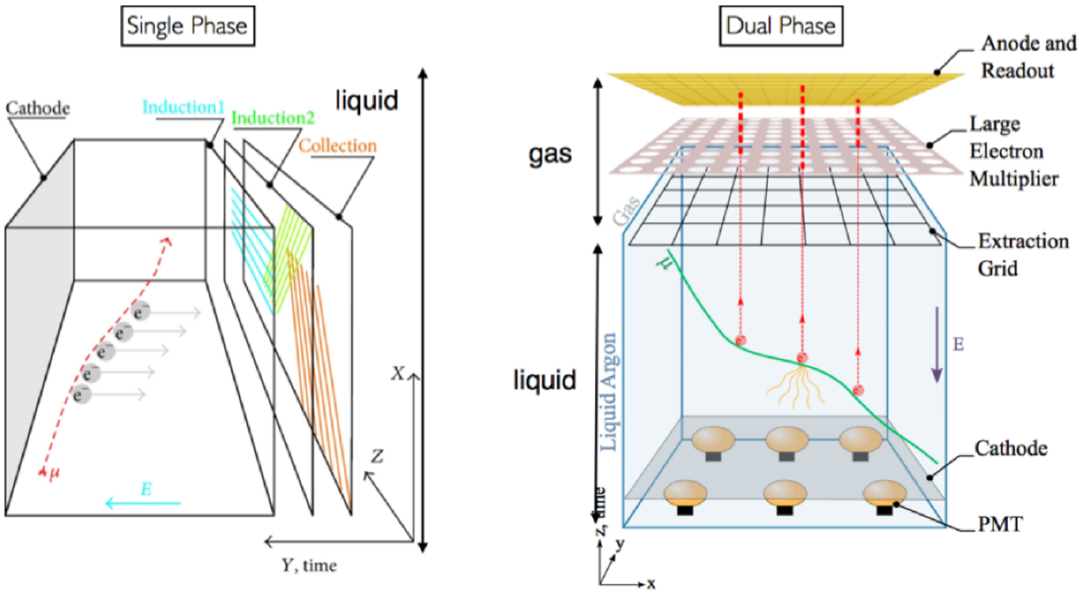

Figure 2.3: (Left figure) Single phase TPC and readout, (right figure) Dual phase TPC and readout. Figures are taken from the reference[38].

requirement on the electronic noise.

2.1 ProtoDUNE-SP experiment

The first DUNE FD module will use the single-phase liquid argon time projection chamber technology (LArTPC), the same technology used in the ProtoDUNE-SP experiment. The active volume of the ProtoDUNE-SP detector is 7.2 × 6.1 × 7.0 m^3. This is the largest monolithic LArTPC built to date. It is built in an extension of the ENH1[43] hall in the North Area, where a dedicated charged-particle test beamline is provided by the CERN neutrino platform. Different species of beam particles including p, π^+, K^+, e^+, μ^+ in the momentum range 0.3 GeV/c to 7 GeV/c are directed into the Time Projection Chamber (TPC). The principal goals with which the ProtoDUNE-SP detector was built are as follows:

- ProtoDUNE-SP serves as a testbed for the designing, production, and installation procedures for the DUNE-FD first module. This experiment will validate the design based on the detector performance for cosmic and beam data. For this purpose, the components used in the ProtoDUNE-SP TPC are full-sized components that will be used in the DUNE FD.

- In ProtoDUNE-SP we collected a large sample of test-beam data which helps to understand the detector response for different particle species.
- As the DUNE FD is planned to run for a few decades, the stability of the detector over a long period has to be demonstrated. ProtoDUNE-SP will provide a useful takeaway for risk mitigation for the DUNE-FD. ProtoDUNE-SP has run successfully for over 600 days before it was taken down to upgrade it for the second run, this itself indicates the long-term operational stability of the detector.

Described below are the major components of the ProtoDUNE-SP detector:

2.1.1 The cryostat

The ProtoDUNE-SP TPC is installed in a cryostat. A membrane cryostat technology[44] supported by outer steel structure is used in ProtoDUNE-SP. The membrane cryostat technology is widely used for the transportation and storage of Liquified Natural Gas(LNG)[45] and the technology is owned by two companies, Gaztransport & Technigaz (GTT) from France and Ishikawajima-Harima Heavy Industries Co. (IHI) Japan. Figure 2.4 shows the various parts a membrane cryostat is made of. Stainless steel primary membrane contains the liquid and gaseous argon. Different layers surrounding the primary membrane provide heat insulation. The support structure which can be steel or concrete is where the pressure is transferred. For ProtoDUNE-SP the internal dimensions of cryostat are 8.5 m × 7.9 m × 8.5 m, along x, y and z direction respectively. The cryostat is filled with liquid argon except for a region of 0.3 m at the top, where the absolute pressure of 1050 mbar is maintained. There is built a network of steel beams inside the cryostat which supports the TPC.

2.1.2 Liquid argon purification system

Historically, different sensitive mediums have been used in particle detectors, ranging from water to many inert gases. However, for a TPC we require a medium that is transparent to

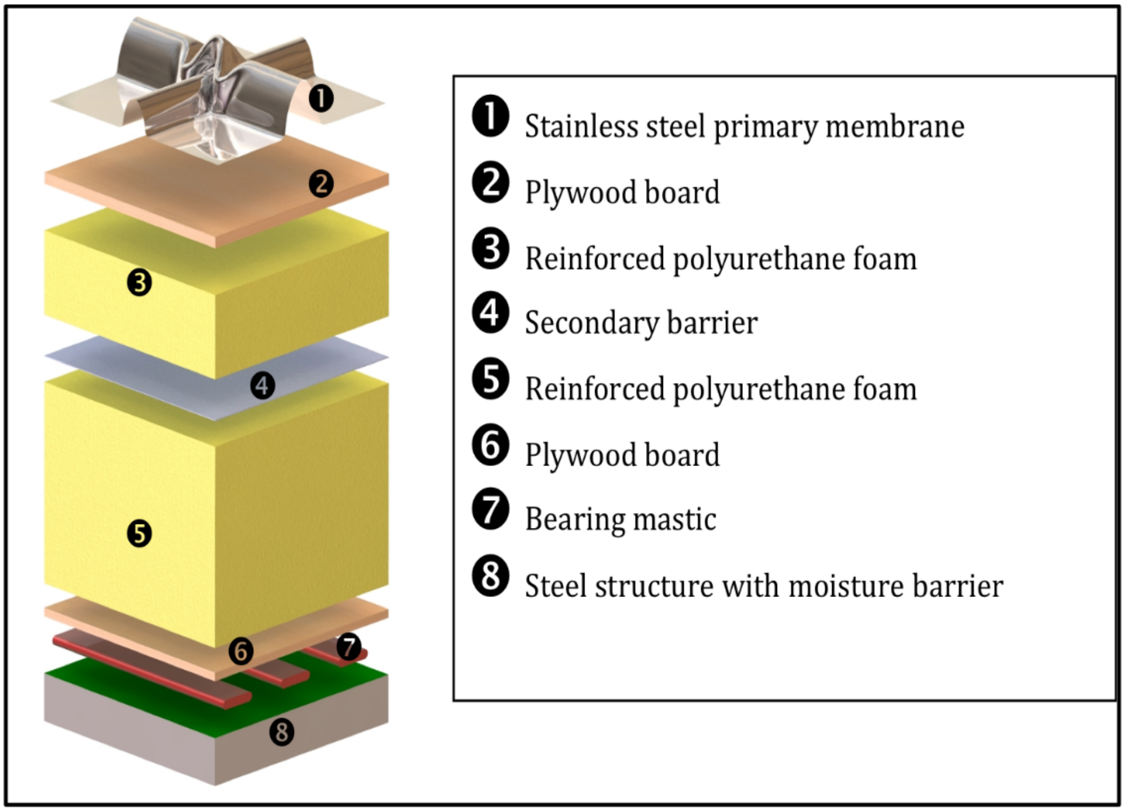

Figure 2.4: Membrane cryostat technology used in ProtoDUNE-SP detector. The figure is taken from the reference[46].

ionization electrons. Inert gases are best suited as a sensitive medium for a TPC as they do not capture the ionization electrons drifting under the action of an applied electric field. Table 2.1 shows the properties of inert gases.

Property	He	Ne	Ar	Kr	Xe
Boiling point at 1 atm (K)	4.2	27.1	87.3	120.0	165.0
Density (g/cm^3)	0.125	1.2	1.4	2.4	3.0
Radiation Length (cm)	755.2	24.0	14.0	4.9	2.8
dE/dx (MeV/cm)	0.24	1.4	2.1	3.0	3.8
Scintillation (γ/MeV)	19000	30000	40000	25000	42000
Scintillation λ (nm)	80	78	128	150	175

Table 2.1: Properties of inert gases[47].

Argon has a higher boiling point compared to He or Ne. For neutrino detectors we require a medium of higher density as the neutrino cross-section is very low and higher density will increase the chances of interaction; argon has a density of 1.4 g/cm^3 which makes it suitable to be used as a medium for neutrino detectors. In addition, other inert gases in the table namely krypton and xenon are very expensive, and building a neutrino detector with those mediums may not be sustainable. Water is electro-negative, it captures the electrons drifting towards the anode, so water cannot be considered as a medium for TPCs.

Further, for the successful operation of a LArTPC, we need a pure sample of liquid argon. The liquid argon from the industrial supplier has contaminants such as water, oxygen, and nitrogen at parts per million level each. Water and oxygen being electro-negative will capture the drifting electrons thus making it difficult to receive any signal at the anode. We need to remove the contaminants by a factor of at least 4 for smooth TPC operation. The purification technique for liquid argon is described in[48]. In ProtoDUNE-SP we use a purification system that uses the same technology that was developed for ICARUS. Figure 2.5 shows the main components of the liquid argon purification system. The liquid argon passes through three circulation loops. The liquid leaves the cryostat through a penetration in the sidewalls, pumped as a liquid through a set of filters, and reintroduced into the cryostat at the bottom. A complete volume turnover takes 4.5 days.

2.1.3 The Time Projection Chamber

A time projection chamber (TPC) is a type of particle detector with a volume of liquid or gas in an electric field to perform particle energy and trajectory reconstruction. The history of TPC dates back to the late 1970s, when David R. Nygren, an American physicist, at Lawrence Berkeley Laboratory invented the first TPC[49]. In 1977, Carlo Rubbia proposed a liquid argon time projection chamber (LArTPC) with a view of using them for neutrino detection[50]. A LArTPC uses liquid argon as a sensitive medium. The technology was pioneered in the ICARUS program[51] in which the first large-scale LArTPC named T600 detector was built in the Gran Sasso laboratory, Italy. ICARUS started working in May

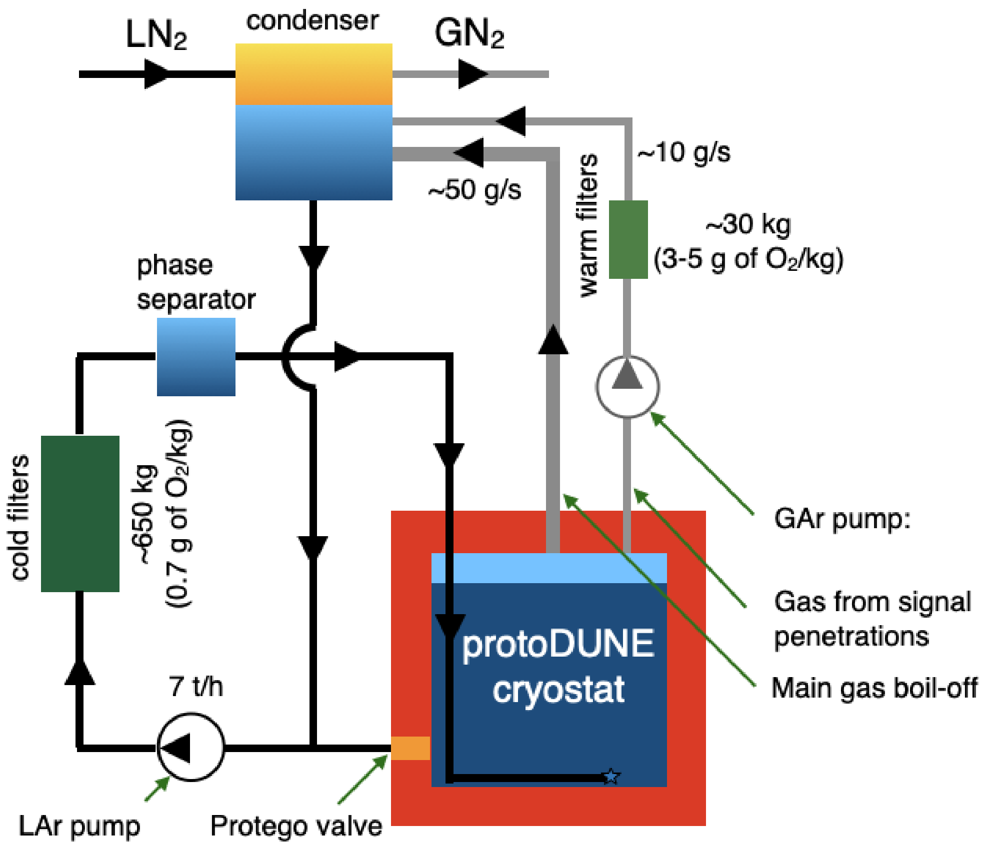

Figure 2.5: A schematic of the argon purification system at NP04. The figure is taken from[26].

2010, collecting cosmic data as well as neutrino beam data from the CNGS[52] (CERN to Gran Sasso) neutrino beam. The detector contained a volume of 600 tons of liquid argon. Since then there have been a few more large-scale liquid argon time projection chambers in the US. The ArgoNeuT and the MicroBooNE detectors built at Fermilab have already collected years of neutrino beam data. The ProtoDUNE-SP detector at the CERN neutrino platform started taking data in September 2018. Work is in progress for the building of a massive neutrino detector, Deep Underground Neutrino Experiment (DUNE), which will use LArTPC technology.

A TPC consists of a cathode and an anode. A potential difference is applied between the cathode and the anode. When a charged particle passes through liquid argon it causes ionization, creating electron-ion pairs. The electrons drift under the action of an electric field towards the anode where they are collected. For ProtoDUNE-SP the TPC is divided into two halves with a cathode plane assembly (CPAs) in the center, at x=0 in the yz plane. There are anode Anode Plane Assemblies (APAs) on either side of the cathode at a distance of ±3.6 m. In ProtoDUNE-SP coordinate system, x is the drift coordinate, y is the vertical direction and z is along the wire planes. The two drift volumes of the TPC are of dimensions 3.6 m × 6.1 m × 7.0 m along x, y and z direction respectively. The major components of ProtoDUNE-SP TPC (figure 2.6) are described below:

Cathode Plane Assemblies and Field Cage: The cathode plane assembly comprises 6 vertically stacked CPAs each being 1.15 m wide and 6.1 m high. The cathode plane is biased to a nominal voltage of -180 kV. If the cathode were electrically conducting an electric breakdown when releasing the stored energy could affect the integrity of the detector elements, endangering the front-end electronics. The CPA panels are therefore made from FR4, a fire-retardant fiberglass epoxy composite material. Furthermore, these panels are coated with Kapton film with a resistivity of ~ 3.5 M Ω/sq. A field cage (FC) assembly is used to surround the four open sides of the two drift volumes. These are used to maintain a uniform electric field inside the TPC.

Anode Plane Assemblies: The anode plane on each side of CPA consists of 3 APA. Each APA has a rectangular stainless steel frame of 2.3 m width and 6.1 m height. There are four planes of wires bonded on each APA. The wire planes are in a different orientation as shown in figure 2.7. In the order of increasing distance from the cathode plane, the wire planes are oriented as Grid (G) (vertical), the U plane (+35.7° with vertical), the V plane (-35.7°), and the X plane (vertical). A bias voltage is applied between the wire planes such that the ionization electrons pass through the G, U, and V planes without being captured, and finally get collected at the X plane, hence X plane is also known as the collection plane, and U, V planes are known as induction planes. In ProtoDUNE-SP, on the TPC-side there are 2 × 2880 Grid plane wires which are not instrumented and there are 2 × 2400, 2 ×

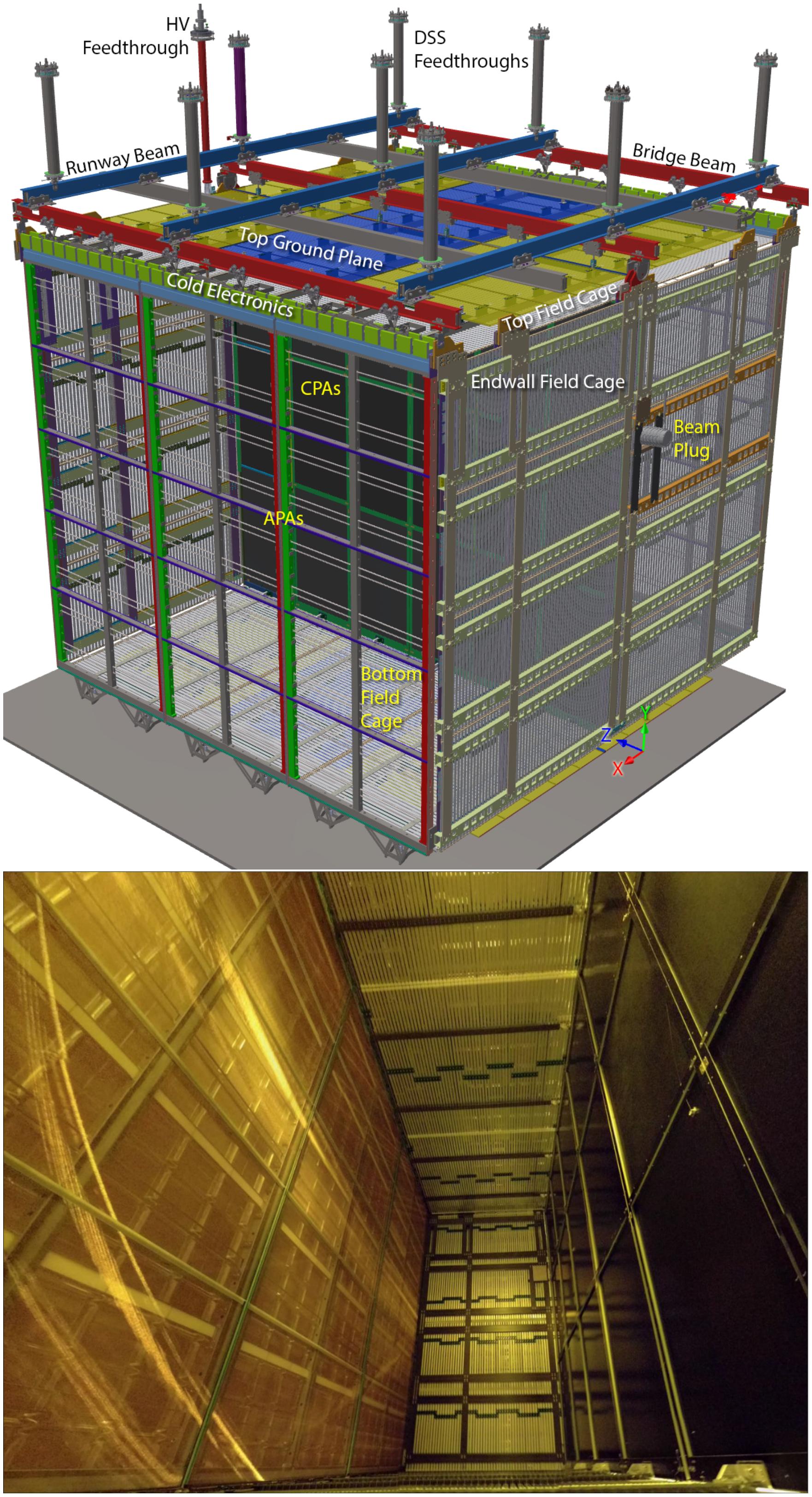

Figure 2.6: Top:Figure shows a view of the ProtoDUNE-SP TPC with its major components labeled and Bottom: Figure shows a photo of one of the two drift volumes with APAs on the left side and CPA on the right. The figures are taken from the reference[26]

2400, and 2 × 1440 instrumented U, V, and X plane wires respectively. In addition, there are 2 × 1440 instrumented collection plane wires on the cryostat side. In total there are 15360 instrumented wires in the ProtoDUNE-SP TPC, which are connected to 15360 different channels. The wire pitch for the G and X wires is 4.79 mm and the wire pitch for the U and V wires is 4.67 mm. There is a gap of 4.75 mm between different wire planes.

Cold electronics: The U, V, and X wires on the APA are read out by front-end motherboards (FEMBs) installed close to the wire boards on top of each APA. The FEMBs amplify, shape, digitize and transmit signals from all the TPC channels to the warm interface electronics through cold data cables.

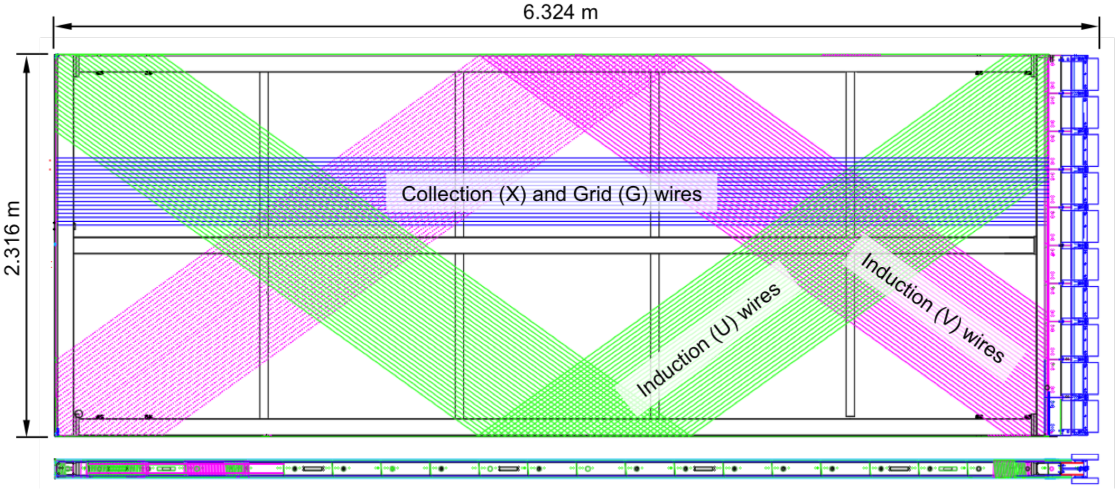

Figure 2.7: Sketch of ProtoDUNE-SP APA. Figure shows the APA turned on its side, the orientation of different wire planes in the APA with respect to each other can be seen. The figure is taken from reference[35].

Beam Plug: The materials in the cryostat and the layer of liquid argon in between the cryostat and the TPC causes a particle to lose energy before entering the TPC. A "beam plug" [36] is therefore installed in ProtoDUNE-SP which allows the passage of beam particles into the TPC with minimum energy loss. The beam enters the TPC about 30 cm away from the cathode on the negative x side at a height of ∼425 cm. The beam plug is placed such that the beam enters the TPC through the beam plug. Figure 2.6 shows the location of the beam plug in the TPC. Figure 2.8 shows the drawing (left) and a photo (right) of the beam plug used in ProtoDUNE-SP. The beam plug is filled with nitrogen at a nominal pressure of 1.3 bar to balance the hydro-static pressure of liquid argon and also to avoid HV breakdown by maintaining high dielectric strength.

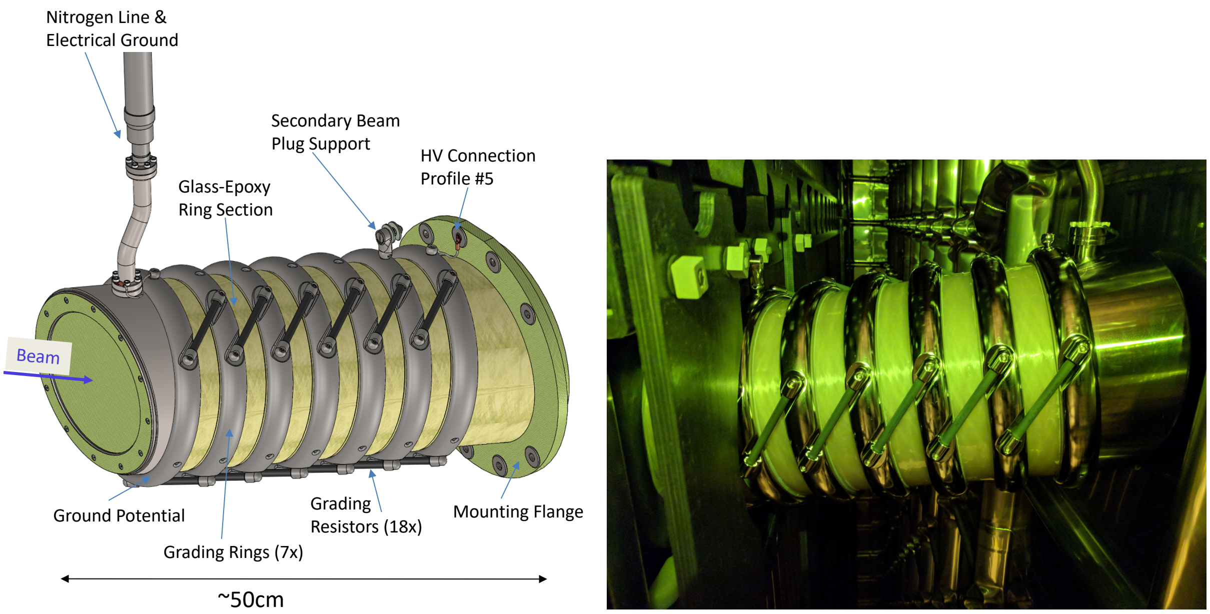

Figure 2.8: Drawing of the beam plug (left) and an image of the beam plug installed inside the cryostat (right). The figures are taken from the reference[26].

2.1.4 Photon Detectors

When a charged particle passes through a LArTPC, in addition to the ionization electrons scintillation light is also emitted. The scintillation light is used in most LArTPCs to determine the time at which the particle enters the TPC, also known as t_0. At a nominal field of 500 V/cm approximately 2.4×10^4 vacuum ultraviolet photons are created per MeV of energy deposited[26]. To detect these photons, a photon detector system (PDS) is installed in the ProtoDUNE-SP detector. The photon detectors are integrated into the APAs, occupying the space between two mesh planes. Silicon photo-multiplier tubes[53] is used to convert the light to electrical signals, which are transmitted out of the cryostat using copper cables. The photon detector system captures a fraction of light emitted in the TPC, which can be calibrated to obtain the energy deposited by a particle as it passes through the medium.

2.1.5 Data acquisition, timing and trigger system

The main role of a data acquisition system (DAQ) is to read the signal generated in the detector and reduce the data volume for permanent storage using online triggering and compression techniques. In ProtoDUNE-SP two candidate readout solutions are under test, the RCE (ATCA-based)[54;55] and FELIX (PCIe-based)[56;57]. RCE and FELIX are used simultaneously, with some APAs using RCE readout and some using the FELIX readout. The ProtoDUNE-SP timing system provides a 50 MHz clock multiplexed on a data stream that is broadcast to all endpoints[26]. To perform event selection a hardware triggering system was designed. The major component of the trigger system is the Central Trigger Board (CTB) which is a custom printed circuit board. The readout decisions are made by the timing system which communicates with Central Trigger Board through various commands. For each triggered readout, the TPC data consists of 6000 consecutive samples of each ADC, which are digitized at a rate of 2MHz (which corresponds to a time of 0.5 μs which is called a “tick”), for a total time of 3 ms. The data readout starts 250 μs before the trigger time.

2.1.6 Signal processing and event reconstruction

Each TPC readout channel records a waveform. The waveform is a linear transformation of the current on the connected wire as a function of time. The signal is a convolution of the effect of induced currents due to drifting as well as collecting charge and the response of the front-end electronics. In the signal processing stage from the input waveform, the distribution of charge arrival times and positions are produced. These distributions are used in subsequent reconstruction steps. The event reconstruction is carried out in two distinct steps:

1. **Hit finding:** A hit represents a charge deposition on a single wire at a given time. The hit finding algorithm fits peaks in the wire waveform. The algorithm searches for candidate hits in the waveform and fits them to a Gaussian shape. Figure 2.9 shows an example of a fitted waveform in which 3 hits are reconstructed.

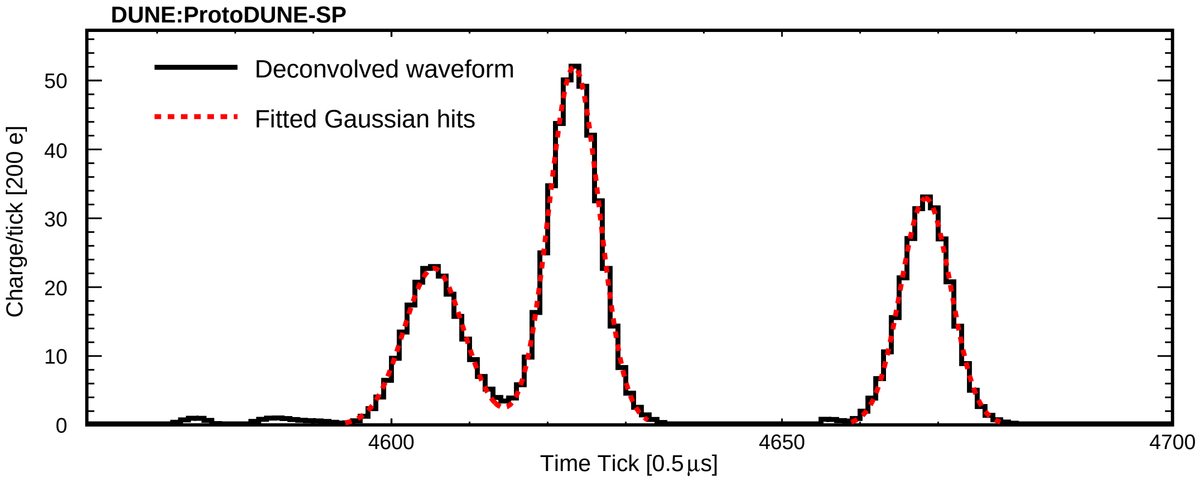

Figure 2.9: An example of a reconstructed waveform on a single wire from ProtoDUNE-SP data. The figure is taken from the reference[26].

2. **Pattern recognition with Pandora:** In ProtoDUNE-SP, pattern recognition is performed using the Pandora software package[58], which has been successfully used in other LArTPCs such as MicroBooNE[59]. Multiple algorithms are used to build up the overall picture of the interaction in the detector. For reconstructed hits, in each wire plane, a separate 2D clustering is carried out. Dedicated algorithms then match views corresponding to 3 different wire planes. Information from all the 3 views is used to reconstruct the three-dimensional hits. Figure 2.10 shows examples of reconstructed events in ProtoDUNE-SP experiment.

2.1.7 Beamline instrumentation

ProtoDUNE-SP uses the tertiary extension of CERN H4 beamline[60]. A highly energetic primary proton beam of momentum 400 GeV/c is extracted from the CERN Super Proton Synchrotron (SPS) and is directed towards a beryllium target producing a hadron beam with a momentum of 80 GeV/c. The secondary beam is then made incident on a copper or a tungsten target, producing a very low energy (VLE) beam, in the 0.3-7 GeV/c momentum range. Tungsten target is used for momenta below 4GeV/c and the copper target is used for higher momenta. The H4-VLE beamline then transports the tertiary beam to the

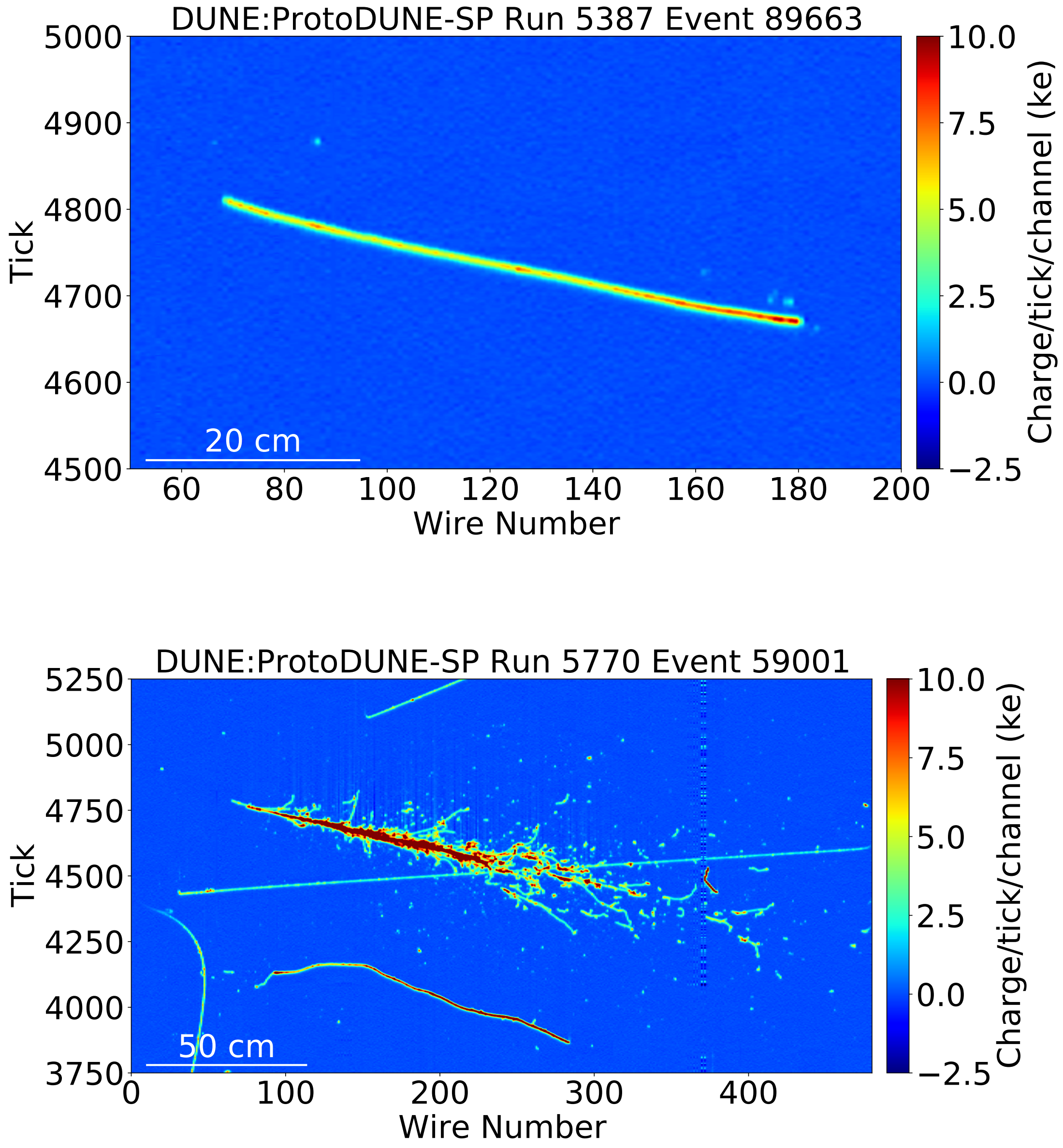

Figure 2.10: figure shows a 1 GeV/c stopping proton candidate (top) and a 6 GeV/c electron candidate (bottom) for ProtoDUNE-SP data[26]. In the bottom event display we can also see cosmic ray muon tracks passing close to the electron shower.

ProtoDUNE-SP detector after making the desired momentum selection.

Figure 2.11 shows the components of the beamline instrumentation. There are 8 profile monitors (XBPFs), which are scintillating fiber detectors, and are used for measuring spatial coordinates as the beam passes through the beamline. Using the spatial coordinates the trajectory of the particle can be projected to the detector front face[61]. The information is used to reconstruct the momentum of the beam particle. There are 3 trigger counters (XBTF) that are used to measure the time of flight (TOF) for the beam particles. The resolution of the TOF measurement is 900 ps. In addition, there are two Cerenkov counters (XCETs), the internal pressure of these counters is tuned to tag different particles at different momenta.

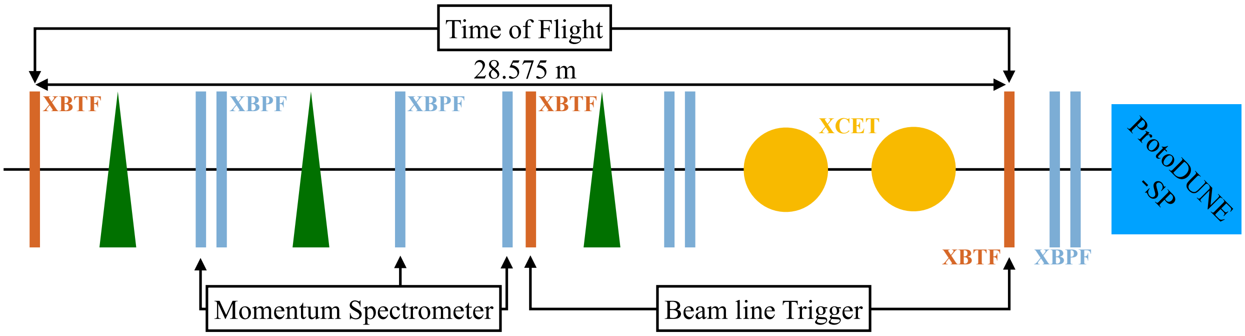

Figure 2.11: Figure shows the relative positions of the trigger counters (XBTFs), bending magnets (triangles), profile monitors (XBPFs) and Cerenkov detectors (XCETs) in the H4-VLE beam line. Figure is taken from the reference[26].

2.1.8 Particle identification logic

A combination of TOF and Cerenkov information is used to identify beam particles across the whole momentum range, 0.3-7 GeV/c. Table 2.2 summarizes the TOF and Cerenkov information for different particle species. Based on the distance between the TOF monitors (28.575 m) and the particle's momentum and its mass the TOF for different particles can be estimated. Figure 2.12 shows the observed and expected TOF for different beam particles (K, e, μ, π, p, and d) used in ProtoDUNE-SP.

Table 2.2: A summary of beam line instrumentation logic used in the identification of particle types. For the high-pressure Cerenkov (XCET-H) and the low-pressure Cerenkov (XCET-L), zero and one represent the absence and presence of a signal respectively. Table is taken from the reference[26].

		Momentum (GeV/c)			
		1	**2**	**3**	**6 - 7**
e	TOF (ns)	0, 105	0, 105	–	–
	XCET-L	1	1	1	1
	XCET-H	–	–	1	1
μ / π	TOF (ns)	0, 110	0, 103	–	–
	XCET-L	0	0	0	1
	XCET-H	–	–	1	1
K	TOF (ns)	–	–	–	–
	XCET-L	–	–	0	0
	XCET-H	–	–	0	1
p	TOF (ns)	110, 160	103, 160	–	–
	XCET-L	0	0	0	0
	XCET-H	–	–	0	0

2.2 LArSoft framework for simulation, reconstruction, and analysis:

The LArSoft[62] "project/collaboration provides an integrated, art-based, experiment-agnostic set of software tools for LAr neutrino experiments to perform simulation, reconstruction, and analysis". The software works for all planned and running LArTPC experiments at Fermilab and is written in C++ and built on the ROOT[63] data analysis software and the **art** event processing framework[64].

Monte Carlo event generators and Geant4 are used for the simulation of the passage of a particle through the detector. LArSoft provides an interface for event generators and Geant4. In ProtoDUNE-SP there are three main sources of particles: the beam particles coming from the beamline, the cosmic ray particles, and the beam halo particles which come from both beamline and other upstream sources. There are different generating processes for each type of particle. Beam particles are generated using the G4Beamline event generator which is used by CERN as standard too for beamline simulation. Cosmic-ray events are

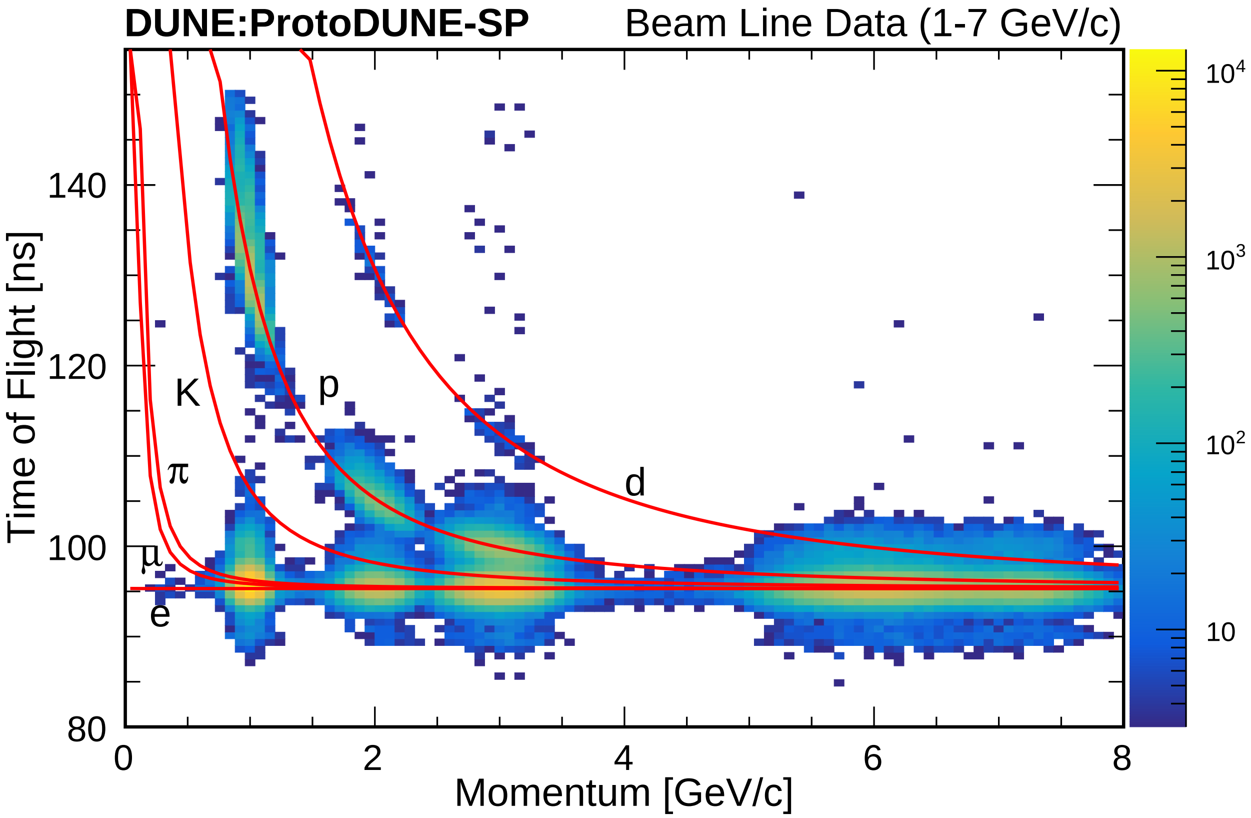

Figure 2.12: The distribution of particles' time of flight against reconstructed momentum from several runs at various beam reference momenta. The red curves are predictions for e, μ, π, K, p and deuterons (d) in order of increasing time of flight. The figure is taken from[26].

simulated with CRY[65] event generator or CORSIKA[66].

The GDML files[67] store the detail of the detector geometry. These files are generated by the GeGeDe geometry[68] system and contain all the specifications of the detector including location sizes, shapes, and material content of the detector components, the active liquid argon volume, and the surrounding materials, and the experimental hall. The active volume is divided into small cubes called voxels. Geant4 tracks particles as they pass through the active volume with each step ending at the voxel boundary and calculates the energy deposited by each particle in each step. The simulation of ionization and scintillation photons is performed by one of the two algorithms: a dedicated parameterization that depends on the electric field and the ionization density[69], or NEST[70], which is tuned to previous noble-liquid experimental results. Thousands of drifting electrons and photons are produced per cm of charged particle track in the detector. Computational techniques are incorporated in LArSoft to provide efficient simulation without loss of accuracy. All the factors which affect the ionization charge produced in the detector such as electron attachment to impurities, space charge effect, diffusion, which are discussed in section 3.1, are simulated in LArSoft.

After the simulation of particles passing through the medium a Pandora Software package is used to reconstruct the particle trajectory and energy. In the Monte-Carlo simulation, we attempt to replicate the ProtoDUNE-SP data as closely as possible. With time there is development in computational techniques and improvement in the understanding of detector physics. To incorporate the improvement in the technology and the understanding of detector physics new Monte-Carlo samples are produced on a timely basis. The Monte-Carlo samples act as an important tool to validate the ProtoDUNE-SP data results.

Chapter 3

Detector calibration

LArTPC provides excellent position and energy reconstruction of a particle passing through the medium. However, there are several factors including Space Charge Effect (SCE), attenuation due to electro-negative impurities in liquid argon such as O_2 and H_2O, diffusion which affects the position and energy reconstruction of the incident particle. These factors distort the particle trajectory as well as cause non-uniformity in the charge deposition in various parts of the detector. In the detector calibration procedure, we first remove the non-uniformity in charge deposition and secondly determine an absolute scale factor to convert deposited charge into deposited energy by a particle as it passes through the medium, which enables us to measure the energy of the incident particle. In this chapter, I will discuss in detail the various sources of non-uniformity in charge deposition followed by the discussion of the calibration technique I developed for ProtoDUNE-SP detector, which uses cosmogenic muons as a standard candle for charge and energy scale calibration. The cosmic muon-based calibration technique for a LArTPC was first developed in the MicroBooNE experiment[71]. In the chapter, I will discuss the charge and energy calibration study I did for ProtoDUNE-SP. The study has been published in[26].

3.1 Non-uniformity in charge deposition

As a particle passes through a LArTPC it ionizes the argon inside the TPC producing electron-ion pairs. A strong electric field is applied between the cathode and the anode planes. In ProtoDUNE-SP a nominal electric field of $\sim 500\ V/cm$ was used, which corresponds to a potential difference of $\sim 180\ kV$ between the anode and cathode plane in the TPC. The ionization electrons drift towards the anode under the influence of the applied electric field. A bias voltage is applied between the wire planes in such a way that the electrons pass through the induction wires producing bipolar signals and finally get collected at the collection wires. Energy reconstruction for different views (wire planes) is carried out based on the charge received at the anode. A range of factors causes non-uniformity in the charge deposition in various parts of the detector. Here, I will discuss some of the factors that cause non-uniformity in the charge deposition.

3.1.1 Space Charge Effect

The space charge effect is the most dominant cause of non-uniformity in charge deposition for a LArTPC built at the surface of the earth. As ProtoDUNE-SP is built at the surface of the earth each minute $\sim 10,000$ cosmic ray muons are incident per m^2 of the detector surface area[72]. These muons create electron-ion pairs in the detector. During the beam data taking ProtoDUNE-SP was running at an average electric field of 0.4867 kV/cm and the average recorded temperature was 87.68 K. At an electric field of 0.4867 kV/cm and temperature of 87.68 K, the average electron drift velocity is 1.56 mm/μs. Walkowiak[73] carried out studies to relate electric field to the drift velocity in a parametric form. A similar study has been done in the ICARUS experiment[39] to relate the electric field to the drift velocity. A LArSoft package[74] combines the Walkowiak's and ICARUS studies in different electric field and temperature regions which I used for converting electric field into drift velocity and vice versa. The positive ion drift velocity is not very well known. However, based on[75–77], positive ion drift velocity is at least 5 orders of magnitude lower than the electron drift velocity. The electrons owing to their relatively higher drift velocity move swiftly to the anode, where they are collected, while the bulky positively charged ions slowly drift towards the cathode. As soon as we turn on the electric field, the excess positive charge starts to build up in the detector. This excess positive charge known as space charge creates its own electric field. The resultant electric field is now a combination of the applied electric field and space charge-induced electric field. The resultant electric field is no longer only along the drift direction, a transverse component of the electric field is also introduced in the detector. The space charge effect in addition to distorting the applied electric field distorts the particle trajectory termed spatial distortion. The resultant electric field is now a function of the position coordinates x, y, and z.

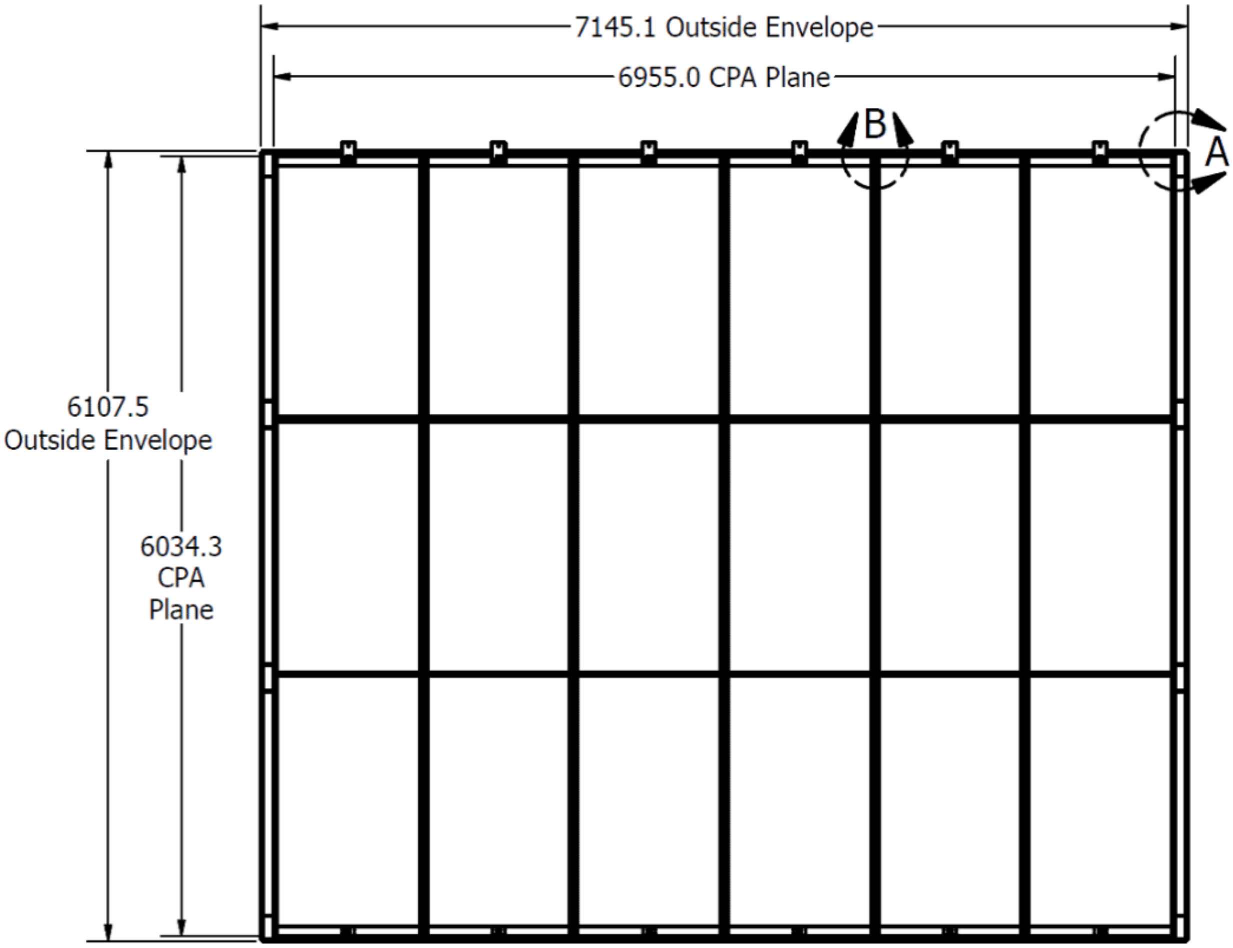

Figure 3.1: Cathode Plane Assembly frames in ProtoDUNE-SP. The figure is taken from[36].

Figure 3.1 shows the drawing of the ProtoDUNE-SP cathode plane assembly (CPA)[36] which consists of 18 modules. The modules hold the CPA panel which is $\sim 3mm$ thick. The frames are $\sim 3.0\ cm$ thick and present on both sides of the CPA panel. These frames are made up of FR4 material. Particles pass through the frame without producing ionization electrons. Cathode-anode crossing cosmic-ray muons are used to produce an image of the CPA panel. The selection of cathode-anode crossing tracks is made based on the time difference between the maximum and minimum peak times for the hits on the track segment confined to a drift volume (either $x < 0$ or $x < 0$ drift volume). Figure 3.2 shows the difference of the maximum and the minimum peak times (ΔT) for cosmic-ray muon track segments for protoDUNE-SP data in a drift volume. The cathode-anode crossing tracks have the maximum possible value of ΔT as they have to cover the entire drift volume. In figure 3.2 the tracks with ΔT lying in the dotted region is selected as cathode-anode crossing tracks. For $x > 0$ region the selected tracks have a ΔT values between $4580 - 4610$ time ticks ($2290 - 2305\mu$s) and for $x < 0$ the selected tracks have drift times between $4590 - 4620$ time ticks ($2295 - 2310\mu$s). There is a small difference in the cathode-anode drift times on the two drift volumes which could be caused by different reasons including cathode-anode distance possibly not being the same on the two drift volumes.

Figure 3.3 shows the image of the CPA panel made using cosmic-ray muons. The plot is made using tracks that cross the cathode and an anode plane. The plot shows the distribution of reconstructed y and z position of the hit closest to CPA (or in other words the hit in a track taking the longest time to reach the anode plane) for the sample of cathode-anode crossing tracks selected based on the ΔT distribution as discussed above. Due to the ΔT cut, the tracks passing through the frames do not appear on the plot as for those tracks cathode-anode drift distance is shorter owing to the portion of the track passing through the frames leaving no ionization. The gaps in the figure 3.3 correspond to the location of the frames. As can be seen from figure 3.1, CPA frames are straight bars (7 horizontal bars and 4 vertical bars). However, in the image of the frames in figure 3.3, the bars are no longer straight. The transverse component of the electric field introduced by the space charge effect causes the ionized charge to displace along the y and z direction which makes the image of the frame appear curved. The distortion along y and z coordinates appear to be smaller towards the center of the CPA. Near the edges of the CPA, a distortion of $\sim 30\ cm$ is observed.

The space charge effect also distorts the electric field along the drift direction which leads to non-uniform drift electric field and hence non-uniform drift velocity. Thus the x position reconstruction which is done using a constant drift velocity is also affected by space charge. The space charge distorts the 3D trajectory of a particle. When a particle passes through the TPC we use the charge deposited per unit length of the track(dQ/dx) for energy reconstruction. The dQ corresponds to the charge corresponding to a hit and dx is the spacing between hits also known as pitch. Space charge effect affects dx as well as dQ which is discussed in section 3.1.2.

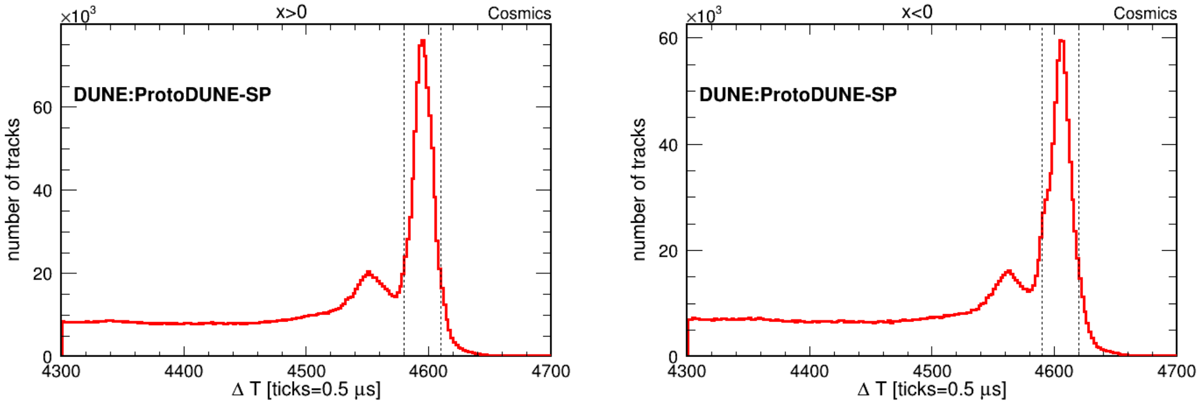

(a) $x > 0$ (b) $x < 0$

Figure 3.2: Cathode-anode crossing track selection based on the drift times for $x > 0$ region (a), and $x < 0$ region (b). The tracks inside the dotted lines are selected as cathode-anode crossing tracks. The leading peak is due to the cathode-anode crossing tracks passing through the frames.

3.1.2 Recombination Effect

As ionization electrons are produced in a medium the interaction with the surrounding medium thermalizes the ionisation electrons which may recombine with the parent ion under the influence of the Coulomb field of the pair, or may recombine with nearby ions. Reattachment with the parent ion is the dominant recombination process based on Osnager

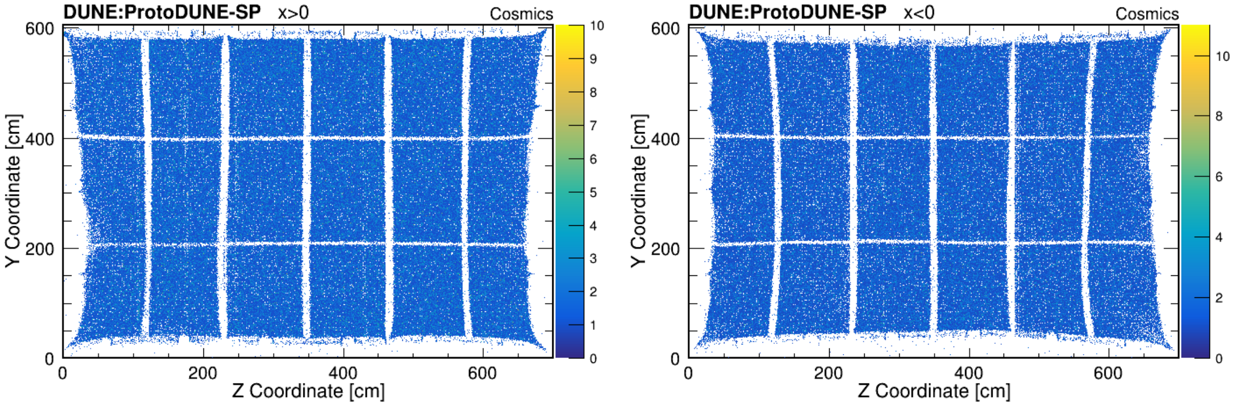

(a) $x > 0$

(b) $x < 0$

Figure 3.3: Cathode-anode crossing track selection based on the drift times for $x > 0$ region (a), and $x < 0$ region (b). The tracks inside the dotted lines are selected as cathode-anode crossing tracks.

geminate theory[78]. A global model cannot describe the recombination at all energies and electric field. Different recombination models have been developed for a LArTPC with some pioneering work done in ICARUS[51] and ArgoNeut experiment[79]. ICARUS was the first experiment to study the recombination effect for varying stopping power (dE/dx) and electric field($\mathscr{E}$). Figure 3.4 shows the recombination factors, which is the fraction of electrons remaining after recombination takes place, for different models used in a LArTPC as a function of the stopping power (dE/dx) at fixed electric field of 0.5 kV/cm. The ICARUS data is well described by the Birk's model[80] as shown in equation 3.1,

$$\mathscr{R}_{ICARUS} = \frac{A_B}{1 + k_B.(dE/dx)/\mathscr{E}} \tag{3.1}$$

with $A_B = 0.800 \pm 0.003$ and $k_B = 0.0486 \pm 0.0006$ $(kV/cm)(g/cm^2)/MeV$.

Stopping power (dE/dx) is reconstructed using the equation 3.2,

$$dE/dx = (dQ/dx)/(\mathscr{R}W_{ion}) \tag{3.2}$$

where $W_{ion} = 23.6 \times 10^{-6}$ MeV/electron (the work function of argon). Using Birk's form[79] of the recombination the stopping power is given by equation 3.3,

$$dE/dx = \frac{dQ/dx}{A_B/W_{ion} - k_B(dQ/dx)/\mathscr{E}} \tag{3.3}$$

As the denominator in equation 3.3 approaches 0 the value of dE/dx becomes very high, however this issue is not present in the inverse Box model equation[79],

$$dE/dx = (exp(\beta W_{ion}.(dQ/dx)) - \alpha)/\beta \tag{3.4}$$

All the recombination models require knowledge of the electric field. As the electric field is non-uniform in the presence of SCE, this leads to non-uniformity in dQ/dx values in different parts of the TPC. Thus the accurate determination of electric field as a function of position coordinates becomes very important for reliable energy reconstruction.

3.1.3 Attenuation due to electro-negative impurities

The electro-negative impurities such as O_2 and H_2O present in liquid argon absorb the electrons traveling towards the anode. This results in a lower number of electrons reaching the anode. As a result, the signal received at the anode gets attenuated. The charge loss due to electro-negative impurities depends on the drift time or equivalently drift distance, the longer the charge has to drift in argon more likely it is to be absorbed by the impurities.

$$Q(t_{\text{drift}}) = Q(0) \times e^{-\frac{t_{\text{drift}}}{\tau}} \tag{3.5}$$

$$Q(x_{\text{drift}}) = Q(0) \times e^{-\frac{x_{\text{drift}}/v_{\text{drift}}}{\tau}} \tag{3.6}$$

where

Q(0) = charge liberated and observed for 0 drift,

Q(t_{drift}) = charge reaching the anode if a charge Q(0) is liberated in the TPC and takes time

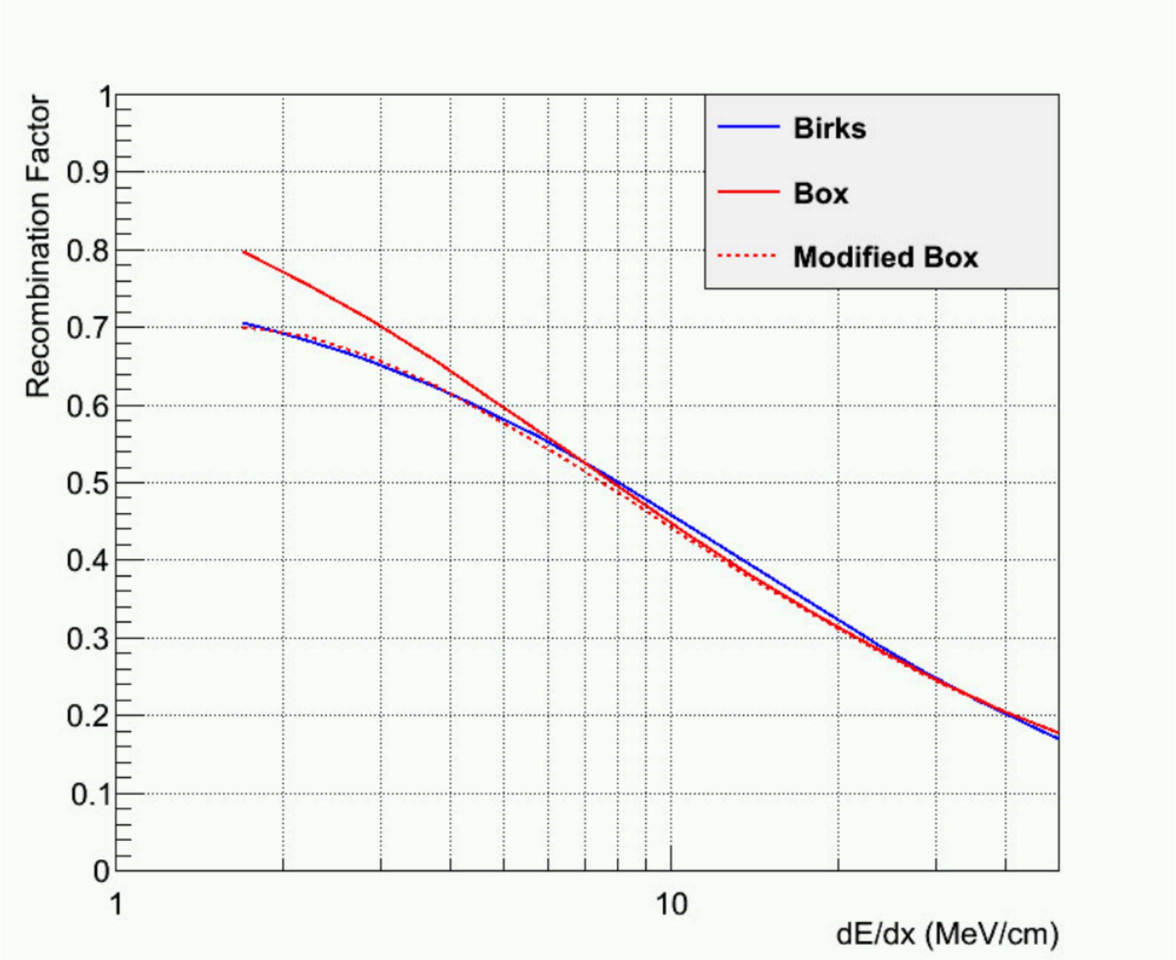

Figure 3.4: Recombination as a function of stopping power (dE/dx) for various recombination model used in LArTPC. The Birk's equation using ICARUS parameters (blue curve), the "canonical" Box model with $\alpha = 1$ and $\beta = 0.83$ (red curve) and the modified Box model with $\alpha = 0.93$ and $\beta = 0.30$ (dotted red curve). The plot is taken from the ArgoNeuT recombination analysis publication[79].

t_{drift} to reach the anode,

τ = ionisation electron lifetime, which is indicative of the purity of liquid argon,

v_{drift} = electron drift velocity in liquid argon,

x_{drift} = drift distance to the anode.

An advanced liquid argon purification system is used in ProtoDUNE-SP which is described in section 2.1.2. Purity monitors are used for recording the liquid argon purity, besides, the lifetime can also be measured using energetic cosmic ray muons following equation 3.6.

3.1.4 Diffussion

Diffusion is responsible for the spreading of charge along the direction of motion and in the direction transverse to the direction of motion of electrons. The smearing along the drift direction is known as longitudinal diffusion and the smearing along the transverse direction is known as transverse diffusion. The diffusion changes the width and the peak value of a signal. The longitudinal smearing increases with drift distance and follows the equation 3.7.

$$\sigma_{\mathrm{t}}^2 = \sigma_0^2 + \frac{2D_{\mathrm{L}}x}{v_{\mathrm{d}}^3} \tag{3.7}$$

where

σ_{t} is the rms width of a hit with drift time t.

σ_0 is the inherent pulse width, it is a convolution of wire and electronics response and depends on the detector properties.

v_{d} is average the electron drift velocity

D_{L} is the longitudinal diffusion constant

x is the drift distance

Transverse diffusion causes the charge to spread to the adjacent wires. As tracks pass through the TPC at different angles, we observe a combined effect of longitudinal and transverse diffusion on the signal waveform we record at the anode.

3.1.5 Other non-uniformity causes

The remaining sources of non-uniformity are mainly detector-specific sources. These include non-uniform wire response, electronics gain variation for different TPC channels, distortion caused by electron diverters which are placed in between APA gap to move the charge away from the gap, shorted TPC channel. A dedicated calibration technique to remove the electronics gain variation has been developed in ProtoDUNE-SP. Other, sources of non-uniformity are removed using detector response for cosmic ray muons as described in the next section.

3.2 Charge calibration

The detector calibration is carried out in two steps, the charge calibration, and the energy calibration. In the charge calibration, we remove the non-uniformity in the energy deposition to make the detector response uniform throughout the TPC. In the energy calibration, which is discussed in detail in the next section, we determine a constant scaling factor to convert charge deposition into energy. This section focuses on the charge calibration procedure. We carry out the charge calibration using energetic through-going cosmic ray muons. The energy loss per unit length for muons is uniform for a wide range of kinetic energy[11]. From figure 3.5 we can see for a few GeV of momentum above the minimum ionizing value the variation in dE/dx is small. We use the detector response for energetic cosmic ray muons as a data-driven correction to remove the non-uniformity in charge deposition. The charge calibration is carried out in two steps, YZ calibration, and X calibration. Here, I describe the selection of events that I use to carry out the charge calibration.

3.2.1 Event selection

The tracks used for the charge calibration analysis have to be energetic (should not stop inside the TPC) and well reconstructed. The following selection criteria have to be met by the tracks selected for charge calibration.

- **Fiducial volume requirements:** I define a fiducial volume V1, which is a rectangular prism such that the points inside the volume satisfy $|x| < 350$ cm, 40cm$< y <$ 560cm, and 40cm$< z <$ 655cm. I require both the ends of the track to be outside the fiducial volume V1. This requirement is to ensure that the track selected is not stopping inside the TPC or in other words, the portion of the track inside the fiducial volume V1 lies in a uniform energy loss (dE/dx region. As can be seen from figure 3.5 near the stopping point of the muons (momentum lower than minimum ionizing value) the stopping power (dE/dx) changes significantly for a small change in momentum.
- **Angular requirements:** The reconstruction capability of a LArTPC is limited for

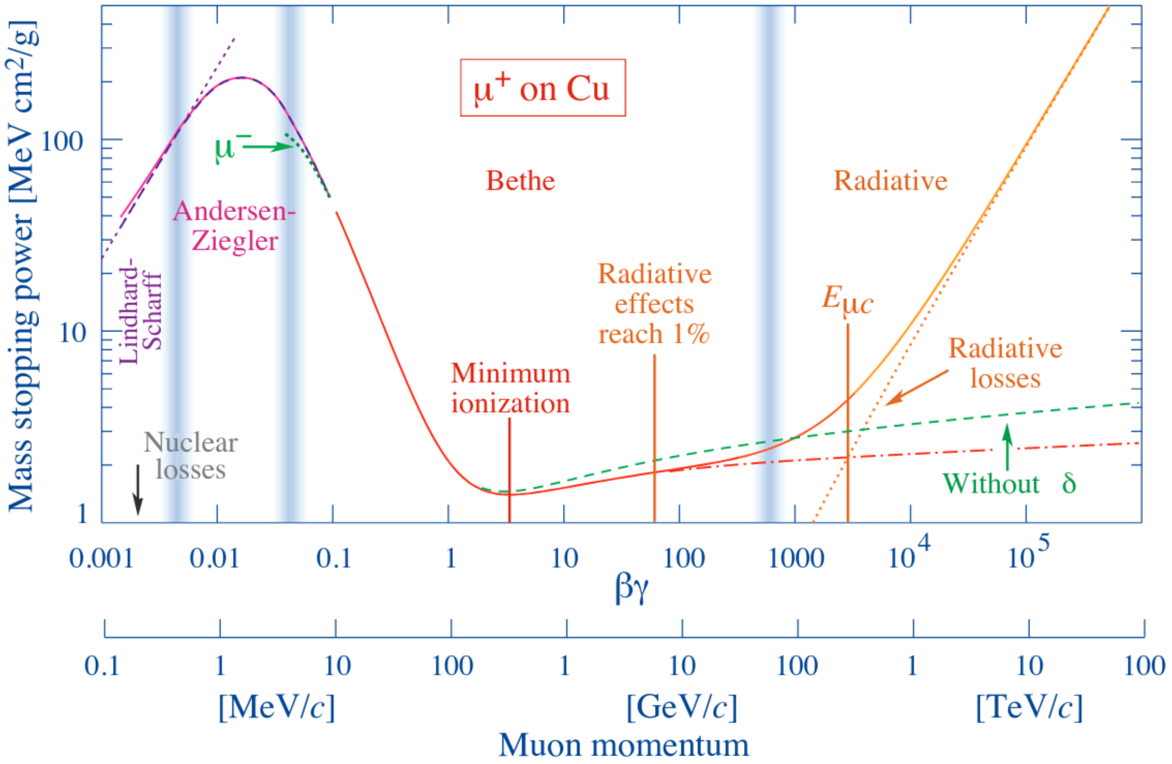

Figure 3.5: μ^+ stopping power in copper as a function of momentum in Cu. In a wide momentum range $\sim 1-5$ GeV the mass stopping power (dE/dx) variation is small. The figure is taken from the particle data group[11].

tracks passing parallel to a wire or moving parallel to the drift direction. For such tracks, all the charge from the incident particle gets deposited in a single wire thus leading to the poor reconstruction of the deposited charge. In ProtoDUNE-SP 3 different wire planes are at different angular orientation, a poorly reconstructed in one of the wire planes could be well reconstructed in the remaining views. This is one of the advantages of using multiple wire planes at different angular orientations. We define two angles θ_{xz} (which is the angle made by the projection of a track on the xz plane with the z direction) and θ_{yz} (which is the angle made by the projection of a track on the yz plane with the z direction). Figure 3.6 shows θ_{xz} and θ_{yz} for coordinate system used in ProtoDUNE-SP. We make a distribution of average dQ/dx vs θ_{xz} and θ_{yz} for 3 different planes using through-going cosmic ray muons. From figure 3.7, 3.8 and 3.9 it is evident that the tracks at certain angular orientation have a very low dQ/dx. The angular cuts are data-driven and different for various wire planes. Following are the angular cuts used for the 3 planes:

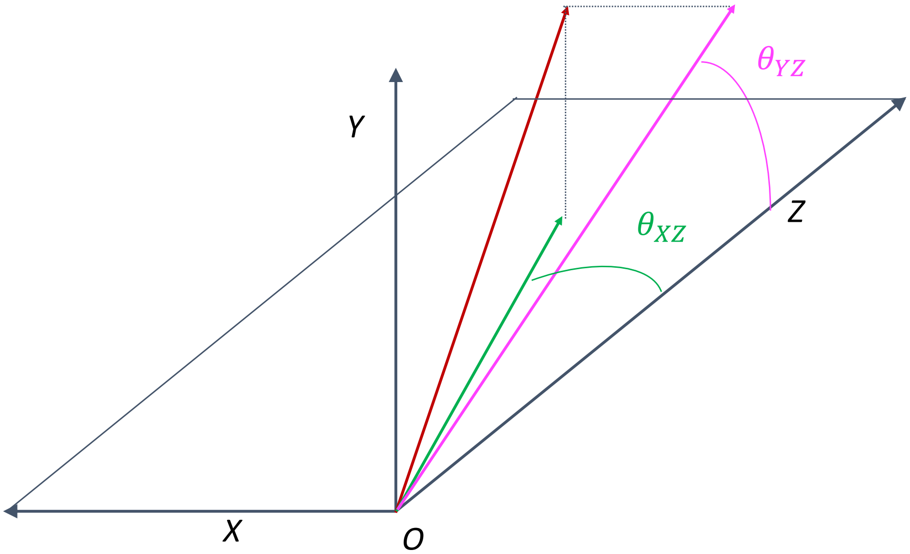

Figure 3.6: θ_{xz} and θ_{yz} definition based on the coordinate system used in ProtoDUNE-SP detector. The figure is taken from[26].

- For collection plane the tracks with $65° < |\theta_{xz}| < 115°$ and $70° < |\theta_{yz}| < 110°$ are removed figure 3.7. The selection criteria is the same for both drift volumes.
- For induction (V) plane there are different angular requirements for the two drift volume based on the average dQ/dx distribution figure 3.8:
  * For $x < 0$, I select the tracks with $\theta_{xz} > 130°$ and θ_{yz} not lying between 80° and 100°.
  * For $x > 0$, I select the tracks with $\theta_{xz} < 40°$ and $\theta_{yz} <$ not lying between 80° and 100°.
- For induction (U) plane as well the angular requirements are different on the two drift volumes based on the average dQ/dx distribution figure 3.9::

- For $x < 0$, I select the tracks with $\theta_{xz} < 40°$ and $\theta_{yz} <$ not lying between $80°$ and $100°$.
- For $x > 0$, I select the tracks with $\theta_{xz} > 130°$ and $\theta_{yz} <$ not lying between $80°$ and $100°$.

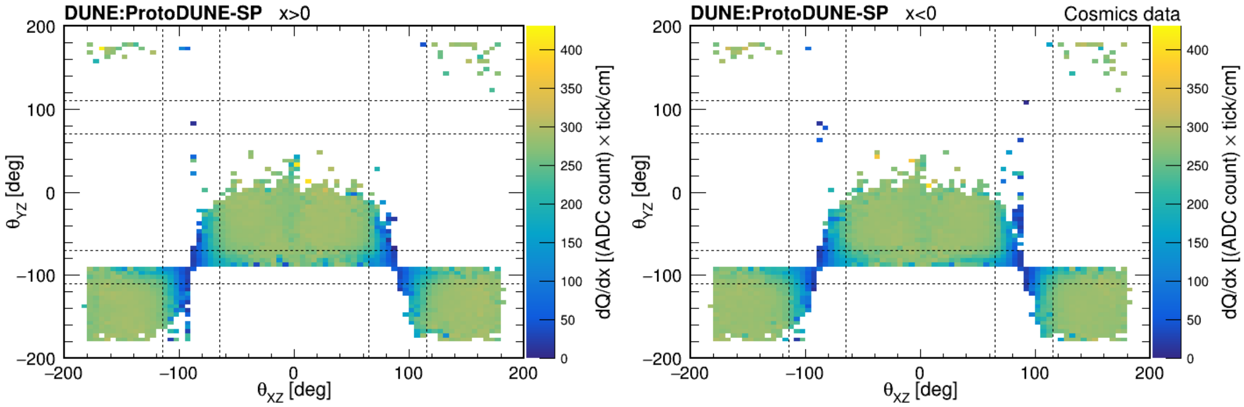

(a) $x > 0$ (b) $x < 0$

Figure 3.7: Average dQ/dx distributions for ProtoDUNE-SP Run 5770 as functions of θ_{xz} and θ_{yz} in the collection plane. The color scale represents average dQ/dx. The regions inside the dashed lines show the track incident angles excluded for the collection plane. 106764 through-going cosmic ray muon tracks were used in making the plots, which constitutes 24.8% of the total number of cathode-crossing tracks in Run 5770. The plots are for collection plane and taken from[26]

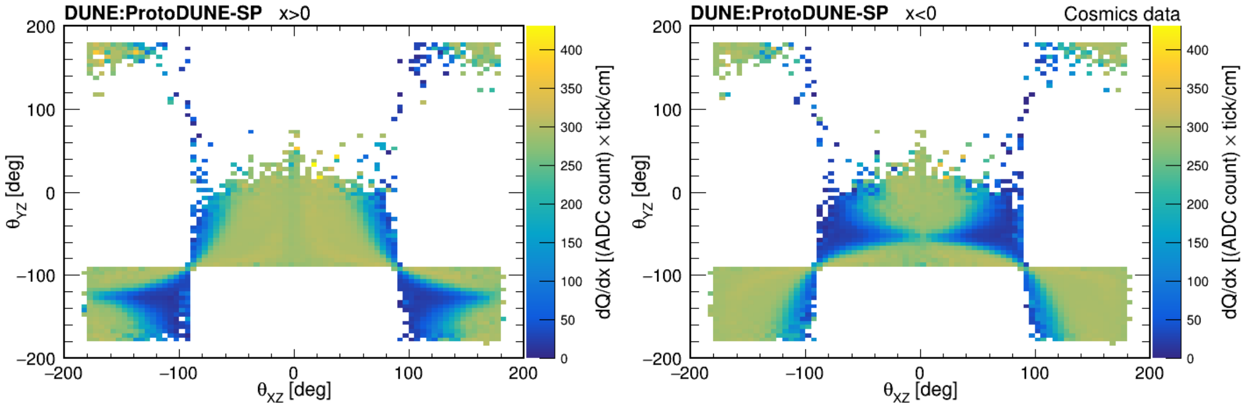

(a) $x > 0$ (b) $x < 0$

Figure 3.8: Average dQ/dx distributions for ProtoDUNE-SP Run 5770 as functions of θ_{xz} and θ_{yz} in the induction (V) plane. The color scale represents average dQ/dx.

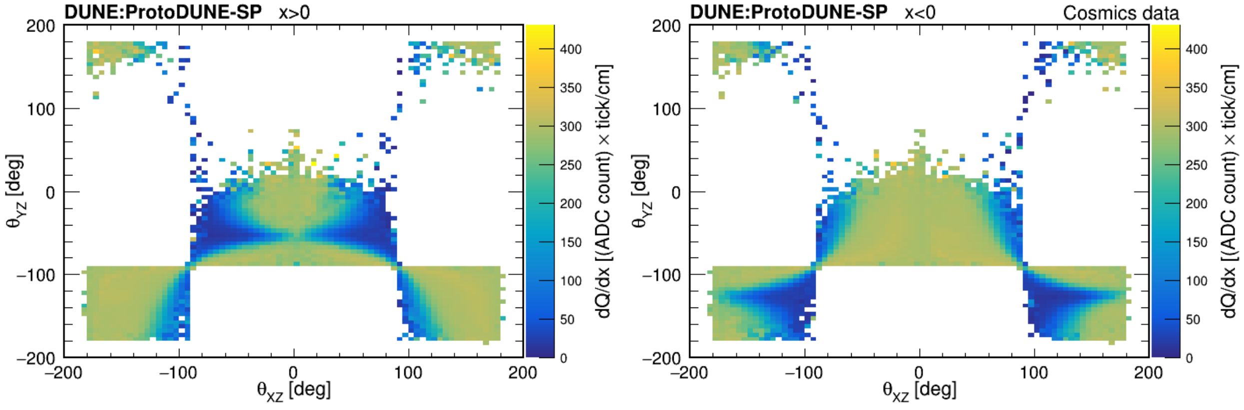

(a) $x > 0$

(b) $x < 0$

Figure 3.9: Average dQ/dx distributions for ProtoDUNE-SP Run 5770 as functions of θ_{xz} and θ_{yz} in the induction (U) plane. The color scale represents average dQ/dx.

Tracks passing the above selection criteria are used for charge calibration (or dQ/dx calibration). Electronics gain variation is removed from the pulser data as discussed in detail in the ProtoDUNE-SP performance paper[26] and SCE is removed using data-driven electric field and spatial distortion map[26]. The remaining non-uniformity in dQ/dx caused by impurities in liquid argon, non-uniform wire response, residual SCE after dedicated SCE calibration, etc are removed using the detector response for through-going cosmic ray muons as a standard candle. The charge calibration is carried out in two steps:

- **YZ correction factors:** Different anode wires may have slightly different wire responses leading to different transparency, this may lead to a difference in the measured waveform in different wires for the same charge collected at the anode. Also, the grid plane on the APA 3 was found to be disconnected during data taking, this caused APA 3 to behave differently compared to other APAs. There is a gap of $2cm$ between adjacent APAs, electron diverters are placed to push away the charge from the gap towards the active APA wires. However, this led to the charge collected in the wires near the APA boundary being low. Transverse diffusion causes the charge to smear to the adjacent wires. All these factors cause non-uniformity on the charge deposition, the non-uniformity being y and z dependent. To the first approximation, we assume the yz distortion is independent of x and the correction factors are averaged over x in a drift volume. To correct for this non-uniformity we divide the yz plane in the two ProtoDUNE drift volumes into many 5 cm×5 cm bins. Considering the dQ/dx values of all the hits lying in a particular bin, the median dQ/dx value is calculated for each bin and denoted $(dQ/dx)^{\text{local}}_{\text{YZ}}$. Further, we calculate the median dQ/dx value considering the hits in the entire drift volume, which is denoted $(dQ/dx)^{\text{global}}_{\text{YZ}}$. We chose the median value as there will be some hits with very large dQ/dx values mainly coming from the delta rays, these will dominate the mean value, thus considering the median value is a better indicator of the charge deposited in each bin. The YZ correction factor is then defined as[26]

$$C(y,z) = \frac{(dQ/dx)^{\text{global}}_{\text{YZ}}}{(dQ/dx)^{\text{local}}_{\text{YZ}}}. \tag{3.8}$$

Figure 3.10 shows the median dQ/dx values as a function of y and z coordinates for the collection plane for ProtoDUNE-SP run 5770. Except for a few bins the dQ/dx value is quite uniform which exhibits the excellent performance of the detector. The low dQ/dx bins on the $X < 0$ plot appearing to divide the yz plane into 3 parts corresponds to the location of the grounded electron diverters. The electron diverters were installed to push the charge away from the gap between the APAs, this inadvertently causes the charge to move away from the nearby regions thus leading to low charge collection in the active region close to APA boundaries. Besides, there are some bins with distinctly low dQ/dx such as the ones on the corner of the TPC on both drift volumes, these are due to detector physical structure. Some stripes can be seen in the distribution which results from a malfunctioning TPC channel. Figure 3.11 shows the YZ correction factors as a function of y and z coordinate for run 5770. The yz correction factors are close to 1 for the majority of the distribution.

- **X correction factors:** The dQ/dx values along the drift direction (x coordinate) are affected by many factors including attenuation due to electro-negative impurities, longitudinal diffusion, remaining SCE distortion not removed by the dedicated SCE

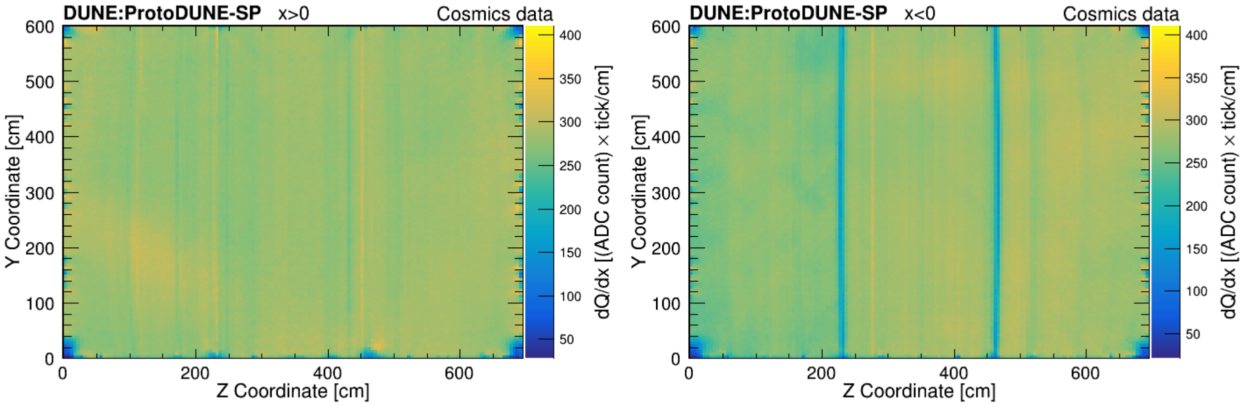

(a) $x > 0$ (b) $x < 0$

Figure 3.10: Median dQ/dx distributions for ProtoDUNE-SP Run 5770 as functions of y and z coordinate. The color scale represents the median dQ/dx. The plots are for collection plane and taken from[26].

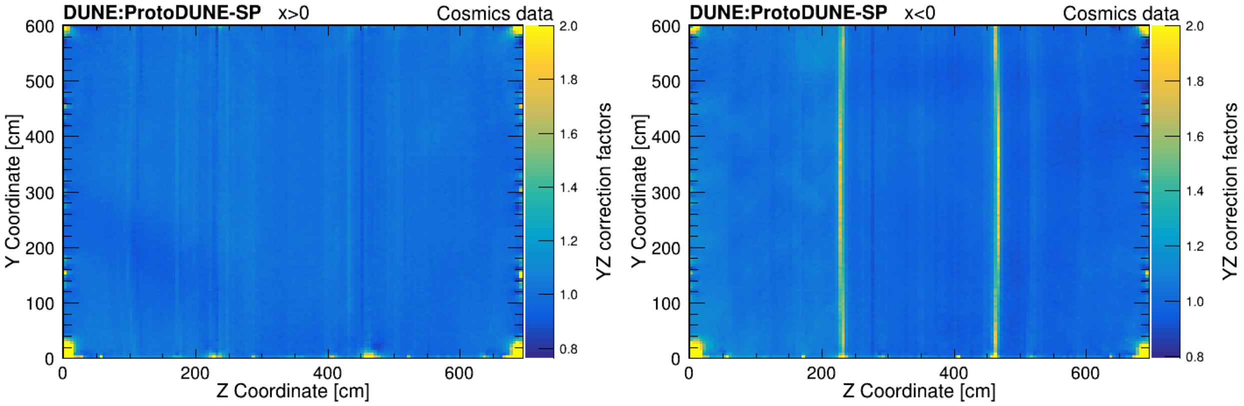

(a) $x > 0$ (b) $x < 0$

Figure 3.11: YZ correction factors factors for collection plane for run 5770 (a)$x > 0$, (b)$x < 0$. The plots are taken from[26].

calibration. We first, remove the non-uniformity along the yz direction applying the YZ correction factors to each hit based on the y and z position of the hit. The remaining non-uniformity is only x dependent. To carry out the X calibration we divide the total drift volume into multiple 10 cm bins along the drift direction. The median dQ/dx value for each bin is calculated, termed as $(dQ/dx)_{\mathrm{X}}^{\mathrm{local}}$ and the median dQ/dx value for the entire TPC is calculated termed as $(dQ/dx)_{\mathrm{X}}^{\mathrm{global}}$. The X correction factor is defined as[26]

$$C(x) = \frac{(dQ/dx)_{\mathrm{X}}^{\mathrm{global}}}{(dQ/dx)_{\mathrm{X}}^{\mathrm{local}}}. \tag{3.9}$$

Moreover, the hits in the bin closest to the anode plane are least affected by any non-uniformity as they have to travel a negligible distance to arrive at the anode. After applying the YZ and X correction factors we normalize the calibrated dQ/dx value to the average of the dQ/dx values at the two APAs. After all the steps of charge calibration, we recover the expected dQ/dx value in the absence of any non-uniformity. The normalization factor is given by

$$N_Q = \frac{(dQ/dx)^{\mathrm{anode}}}{(dQ/dx)^{\mathrm{global}}}. \tag{3.10}$$

The corrected dQ/dx value is given by,

$$(dQ/dx)_{\mathrm{corrected}} = N_Q C(y,z) C(x) (dQ/dx)_{\mathrm{reconstructed}} \tag{3.11}$$

where $(dQ/dx)_{\mathrm{reconstructed}}$ is the measured dQ/dx value in ADC/cm.

Figure 3.12a shows the median dQ/dx as a function of x coordinate for ProtoDUNE-SP run 5770. Plot shows the dQ/dx value decreases exponentially as the distance from the anode increases. This behaviour is due to the absorption of ionisation electrons by electronegative impurities such as O_2 and H_2O as they drift in argon towards the anode. We can determine the electron lifetime fitting plot to equation 3.5. The electron lifetime for the distribution shown in the plot 3.12a is $\sim 12\ ms$. Figure 3.12 shows the X correction factors as a function of x coordinate for ProtoDUNE-SP run 5770.

Figure 3.13 shows the plot of dQ/dx distribution for through-going cosmic ray muons before and after charge calibration. We can see the width of the dQ/dx distribution is narrower after charge calibration. Once we derive the correction factors to make dQ/dx distribution

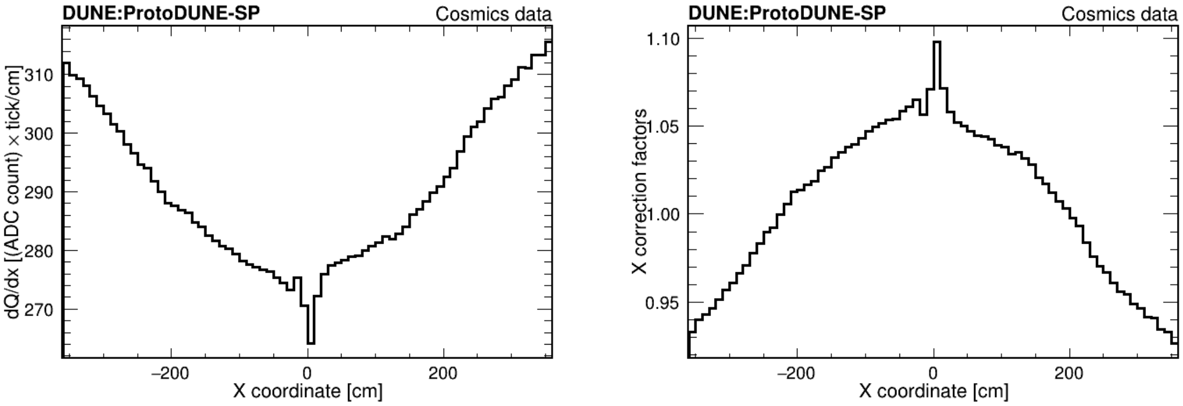

(a) dQ/dx vs x

(b) X correction factors

Figure 3.12: Median dQ/dx vs x (a) and the corresponding X correction factors (b), for ProtoDUNE-SP Run 5770. The plots are for collection plane and taken from[26].

uniform throughout the TPC, we select a sample of stopping cosmic ray muons to carry out the energy scale calibration (or dE/dx calibration) in which we determine an absolute scale factor to convert the charge into energy.

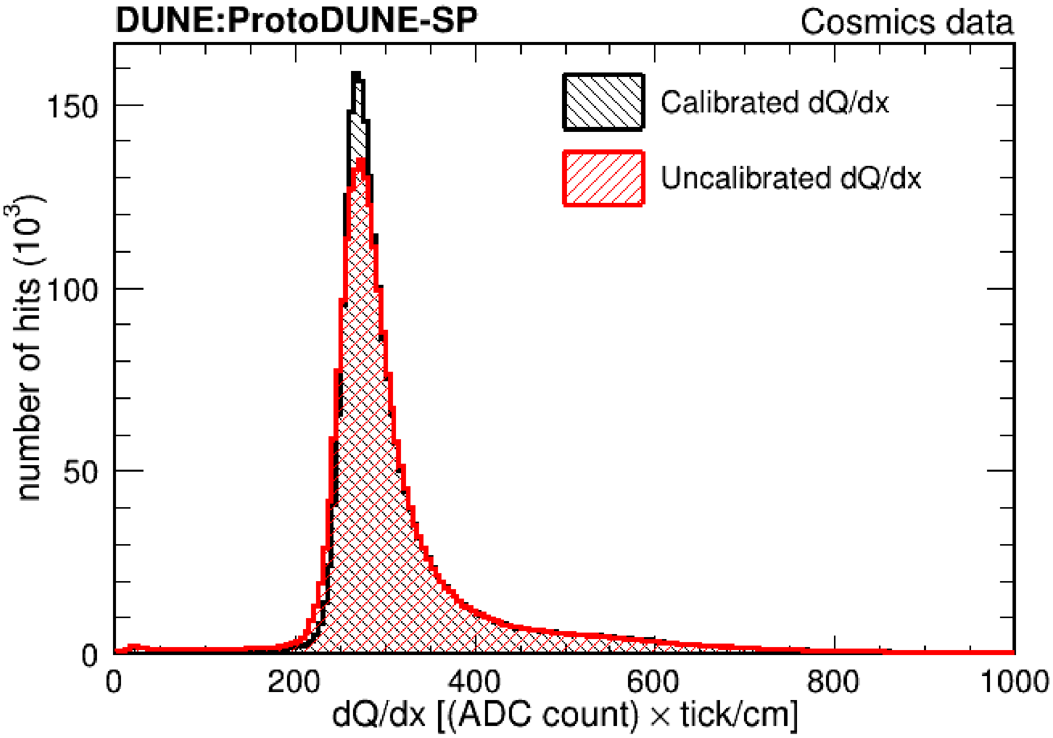

Figure 3.13: dQ/dx distribution for through-going cosmic ray muons before and after charge calibration. The plot is taken from[26].

3.3 Energy scale calibration:

Energy calibration is carried out using cosmic ray muons which stop inside the TPC. For stopping muons we have a portion of the track for which dE/dx is theoretically known to better than 1%. The theoretical predictions of most probable dE/dx value as a function of kinetic energy is based on Landau-Vavilov theory[11]. Figure 3.14 shows the most probable dE/dx as a function of kinetic energy and residual range. We use the minimum ionising region of Kinetic energy, 250-450 MeV, which corresponds to a residual range (distance from the end of the track) of 120-200cm, in this region dE/dx variation is within 1%. Following selection criteria are used for stopping muon selection:

- **Fiducial volume cuts:** For stopping muon selection we require one end of the track to be outside the TPC and the other end to be inside the TPC. I define a fiducial volume V2, which is the rectangular prism inside fiducial volume V1 (described in section 3.2) containing points satisfying $|x| < 330$ cm, 50 cm $< y <$ 545 cm, and 50 cm $< z <$ 645 cm. I require the tracks to start outside the fiducial volume V1 and end inside the fiducial volume V2.

- **Angular cuts:**The angular requirements for removing the poorly reconstructed tracks are the same as for through-going cosmic ray muons as discussed in section 3.2.1.

- **Removing Broken tracks:** Due to reconstruction inefficiencies, some particle trajectory are reconstructed as two or more tracks, which mimic a stopping muon although the particle may not have stopped inside the TPC or the end of the track segment may not be the true endpoint in the case of particle stopping inside the TPC. We need to remove such tracks to get a pure sample of stopping muons. If the start/endpoints of the two tracks are within 30 cm of each other and the angle between them is less than 14°, both the tracks are removed. Also, due to a small gap ($\sim 2\ cm$) between the APAs, there is a tendency for a track to break into multiple segments as they pass through an APA boundary. Additionally, I remove any track which starts or stops within 5cm of the APA boundary.

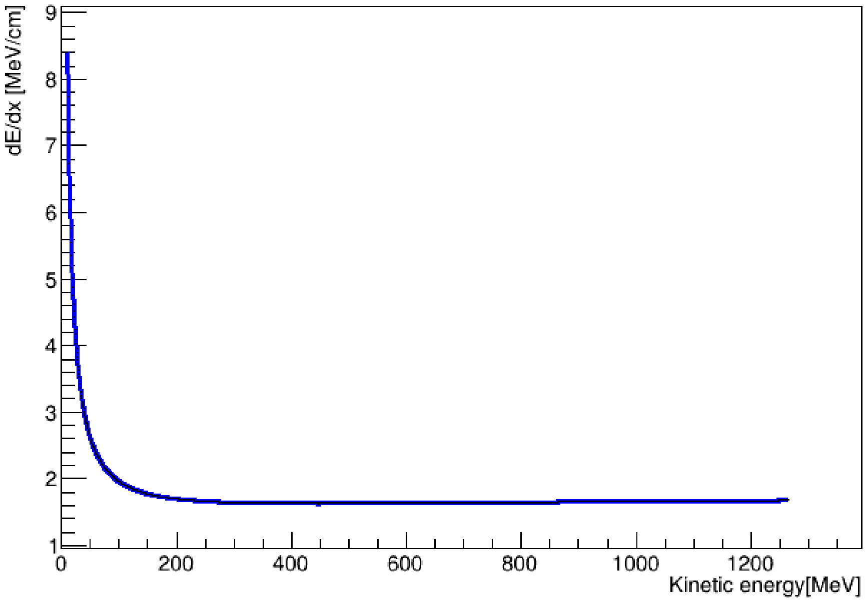

(a) Most probable dE/dx vs Kinetic Energy

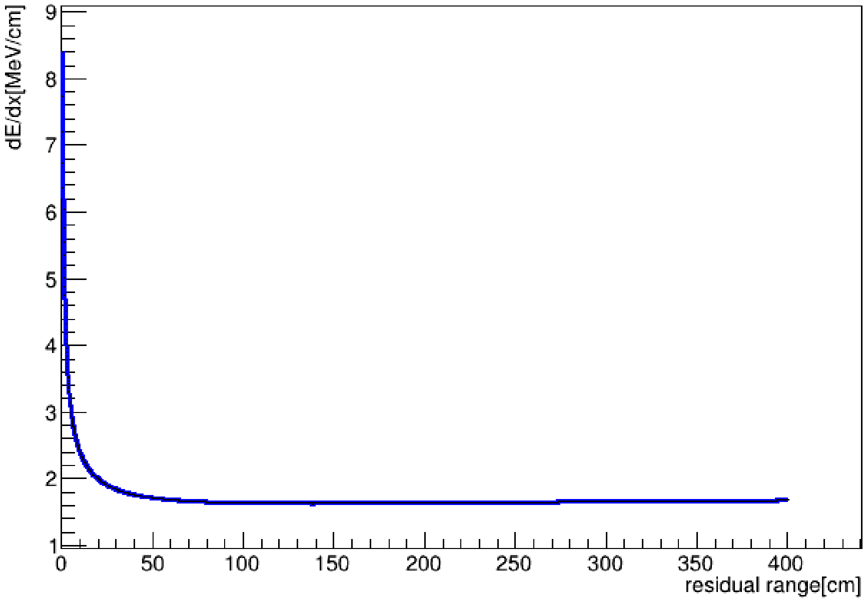

(b) Most probable dE/dx vs residual range

Figure 3.14: Most probable dE/dx vs Kinetic energy (a) and the most probable dE/dx vs residual range (which is the range of a particle at corresponding kinetic energy)(b) for muons in argon. The theoretical predictions are based on Landau-Vavilov theory. The residual range is obtained from kinetic energy based on[81].

- **Removing tracks with early and late hits**: The time window used for an event in protoDUNE-SP is 3000 *ms*. The activities before and after the time window are not recorded in an event. We remove tracks that may be cut off by the 3000 *ms* TPC readout window boundaries and which may mimic a stopping muon. If any hit associated with a track has a peak time less than 125 *ms* ticks or greater than 2950 *ms*, the track is removed.

- **Removing tracks with Michel hits attached:** μ^+ decays into e^+, ν_e, and $\bar{\nu_\mu}$ $\sim$ 100% of time, while μ^- are often captured by positive ions in liquid argon. In the case of muon decay, there is a short electron track, also known as Michel electron, near the end of the parent muon track. It was observed that the reconstruction algorithm often misses some of the muon hits during muon track reconstruction or in some cases includes the hits from the nearby Michel electron in the parent muon track. In such a case the energy loss per unit length (dE/dx) no longer follows the theoretical prediction from Landau-Vavilov. We thus remove the muon tracks which decay into Michel electron. For this, we need to identify the cases where muon decays into an electron. For this, we identify the wire number and hit peak time of the last hit on the track and count the number of hits within ± 5 wires and ± 50 ticks from the last hit of the track and not belonging to the track or any other track longer than 100 *cm*. A count greater than 0, suggests Michel electron-like activity around the end of the muon track, we remove such tracks. If all the Michel hits are attached to the parent muon track the number of hits counted will be 0, in such a case we look at the ratio of the median charge deposited for the last 5 *cm* to the first 5 *cm* of the track, figure 3.15. For a stopping muon, the charge deposited near the end of the track should be significantly higher than at the beginning of the track or charge deposited by a Michel electron. I discard tracks with a ratio of less than 1.4.

The tracks passing the above selection criteria are selected for energy scale calibration. As there is no dearth of cosmic muons in ProtoDUNE-SP, as it is located at the surface of the earth, our primary goal was to obtain a highly pure sample of stopping muons. Purity

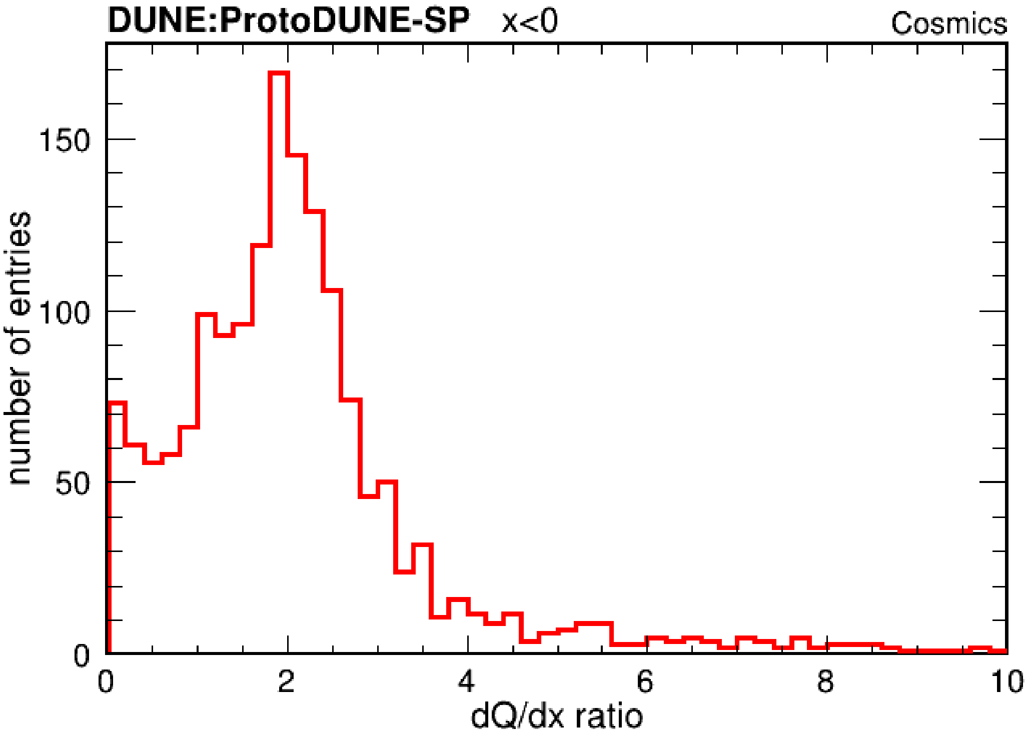

Figure 3.15: Ratio of the median dQ/dx for the last 5 cm and first 5 cm of a stopping muon track. Based on the distribution tracks with ratio>1.4 are selected as stopping muon track.

is defined as,

$$\text{purity} = \frac{\text{Number of true stopping muons in the selected sample}}{\text{Number of stopping muons passing the selection criteria}} \tag{3.12}$$

The purity is estimated based on the Monte-Carlo study. The true stopping points and the true particle id are known for Monte-Carlo. If the true endpoint lies inside the active volume of the TPC and the particle is a muon we consider the particle to be a true stopping muon. A purity of 99.74% is achieved in the Monte-Carlo study.

We apply the correction factors to the dQ/dx values following equation 3.11 to obtain calibrated dQ/dx values. The theoretical most probable dE/dx value as a function of residual range for stopping muon tracks in LAr is accurately predicted by Landau-Vavilov theory. The experimental dE/dx values are obtained from calibrated dQ/dx values using Modified Box Model[79] with calibration constant as a free parameter. The Modified Box Model equation can be written as,

$$\left(\frac{dE}{dx}\right)_{\text{calibrated}} = \left(\exp\left(\frac{(\frac{dQ}{dx})_{\text{calibrated}}}{C_{\text{cal}}}\frac{\beta' W_{\text{ion}}}{\rho \mathscr{E}}\right) - \alpha\right)\left(\frac{\rho \mathscr{E}}{\beta'}\right), \tag{3.13}$$

where

C_{cal} = Calibration constant used to convert ADC values to number of electrons,

$W_{\text{ion}} = 23.6 \times 10^{-6}$ MeV/electron (the work function of argon),

$\mathscr{E}$ = E field based on the measured space charge map,

$\rho = 1.38$ g/cm^3 (liquid argon density at a pressure of 124.106 kPa),

$\alpha = 0.93$, and

$\beta' = 0.212$ (kV/cm)(g/cm^2)/MeV.

α and β' are the Modified Box model parameters which were measured by the ArgoNeuT experiment at an electric field strength of 0.481 kV/cm[?].

The calibration constant C_{cal} is a free parameter in the Modified Box model. In ProtoDUNE-SP C_{cal} is normalized so that the unit ("ADC×tick") corresponds to 200 electrons. In the case where the detector response is perfectly modeled, the calibration constant C_{cal} should be exactly $1/200 = 5\times10^{-3}$ ADC×tick/e. To derive the calibration constant we fit the dE/dx (equation 3.13) from the calibrated dQ/dx along the muon track in the minimum ionizing region (which corresponds to 120 to 200 cm from the stopping point of the track) to the theoretical prediction from Landau-Vavilov using C_{cal} as a free parameter under χ^2 minimization. The methodology for the energy calibration is described as follows:

- For each track passing the above selection criteria, the first 200 cm from the end of the track is considered and divided into 5 cm bins based on the distance from the stopping point(residual range).

- For each residual range bin, dE/dx distribution is plotted and fitted to a Landau-Gaussian distribution[11;82] to determine the most probable value of dE/dx for a particular residual range bin. Figure 3.16 demonstrates dE/dx distribution for one of the residual range bin (residual range between 140 to 145 cm) and the corresponding Landau-Gauss fit to obtain the most probable dE/dx value.

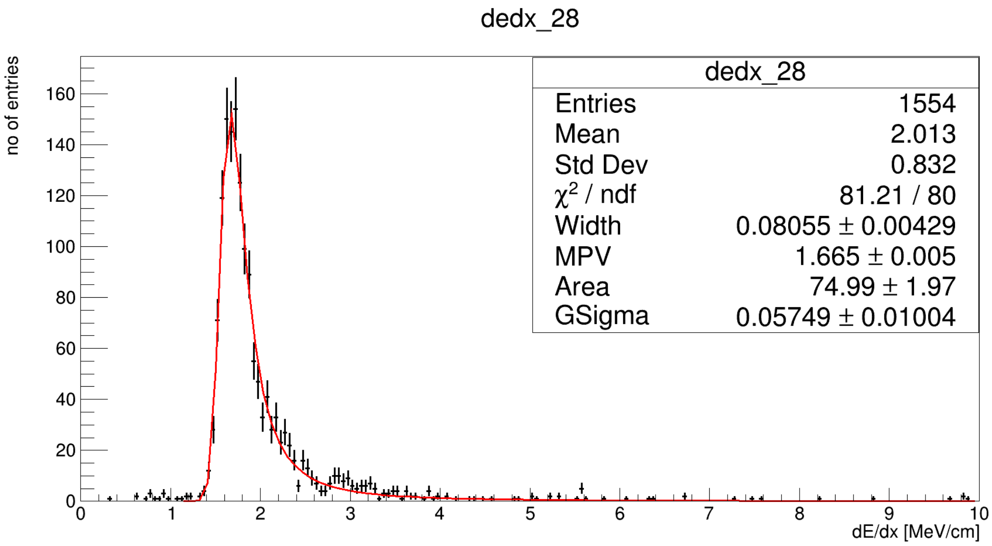

Figure 3.16: dE/dx distribution fitted with a Landau convoluted Gaussian function for residual range values between 140 cm to 145 cm.

- Considering the bins with residual range between 120 cm to 200 cm(or Kinetic energy between 250 MeV to 450 MeV) we estimate the χ^2 value for a wide range of calibration constants. The χ^2 is calculated using the relation,

$$\chi^2 = \Sigma(\frac{(MPV(dE/dx)_{prediction} - MPV(dE/dx)_{Measured})^2}{\sigma^2}) \tag{3.14}$$

  Here the sum is over the bins with kinetic energy between 250 MeV to 450 MeV. The uncertainty is the error on the fit calculated using, $\sigma^2 = \delta^2_{fit}$.The C_{cal} value corresponding to the minimum χ^2 is the final calibration constant.

Figure 3.17 shows the χ^2 values for different calibration constants for ProtoDUNE-SPdata run 5770 and ProtoDUNE-SP Monte-Carlo simulation. Figure 3.18 shows the χ^2-χ^2_{min} for different calibration constant. The statistical uncertainty is estimated by evaluating C_{cal} values for χ^2-χ^2_{min}=1. The table below shows the calibration constants for data run 5770 and Monte-Carlo simulation:

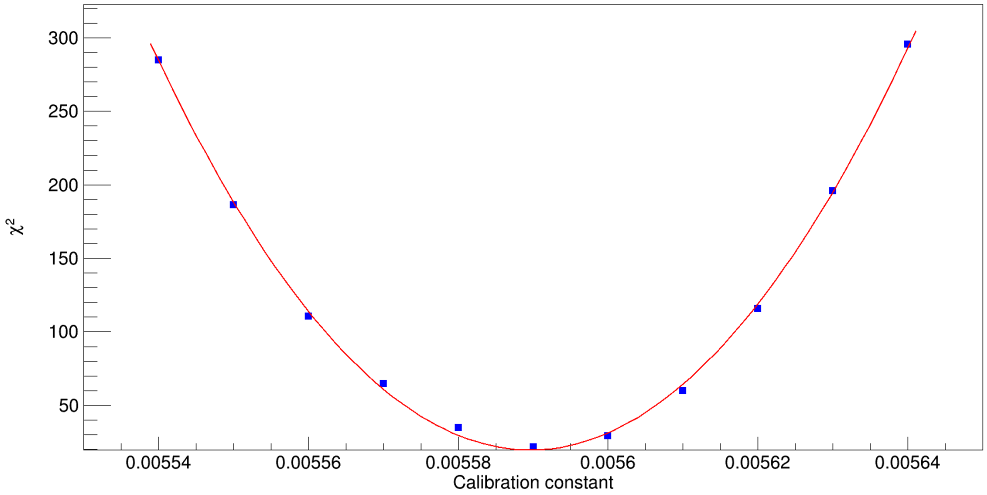

(a) Data run 5770

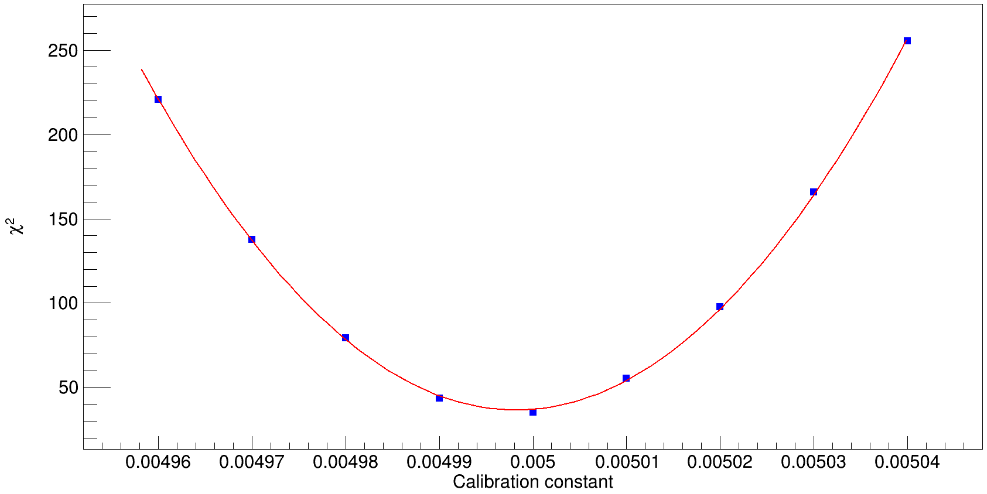

(b) Monte-Carlo

Figure 3.17: χ^2 vs calibration constant for ProtoDUNE-SP data run 5770 (a) and the Monte-Carlo simulation (b).

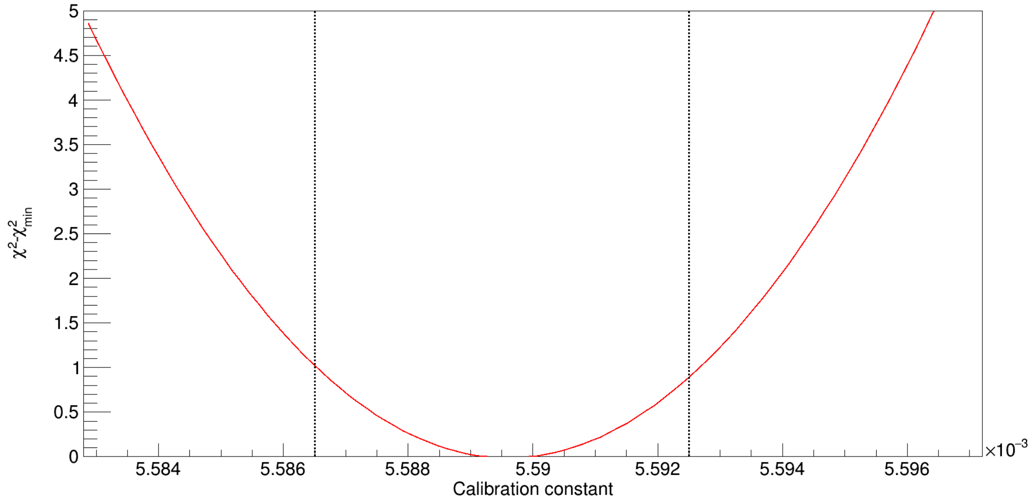

(a) Data run 5770

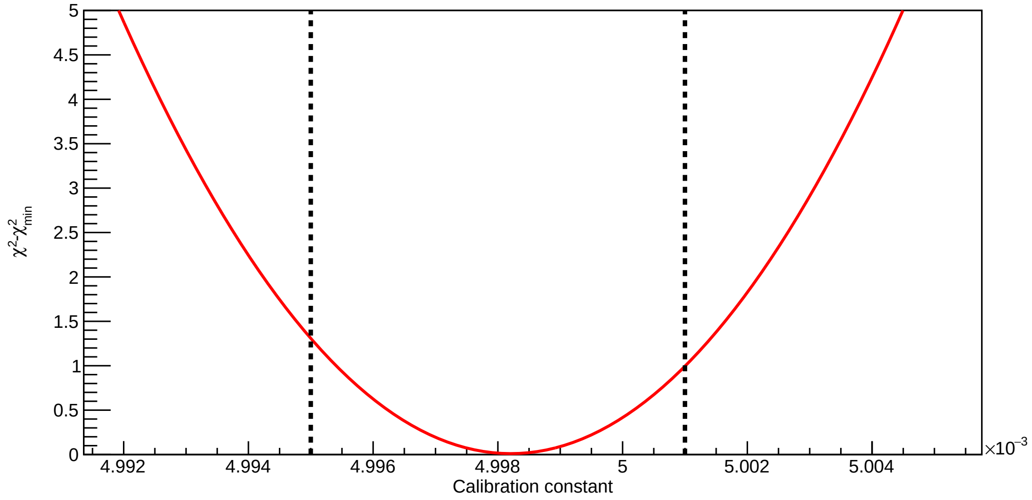

(b) Monte-Carlo

Figure 3.18: χ^2-χ^2_{min} vs calibration constant for ProtoDUNE-SP data run 5770 (a) and the Monte-Carlo simulation (b). The pair of dotted lines indicate the 68.3% confidence interval for measure C_{cal}.

Table 3.1: Values of calibration constants for the collection plane in MC and data.

	Data	MC
Fitted value of C_{cal}	$(5.590 \pm 0.003)\ \times 10^{-3}$ ADC×tick/e	$(4.998 \pm 0.003)\ \times 10^{-3}$ ADC×tick/e

Figure 3.19 shows the comparison of measured dE/dx to the prediction from Landau-Vavilov theory. The measured values are corresponding to the calibration constant with minimum χ^2.

Figure 3.20a and 3.20b shows the calibrated dE/dx vs residual range for ProtoDUNE-SP data run 5770 and Monte-Carlo simulation respectively. The black curve in the figures represent the theoretical predictions from Ladau-Vavilov. Figure 3.20c shows the dE/dx for stopping muons.

3.4 Results and conclusion

In cosmic muon-based calibration, I derived the X and YZ calibration constants to remove the non-uniformity in charge deposition in various parts of the detector and the calibration constant to determine the absolute energy scale. One of the major goals of ProtoDUNE-SP was to study the detector response for different test beam particles, the cosmic muon-based calibration is applied to all other particle species with excellent results thus enabling the study of detector response for various test beam particles. The results from the cosmic muon-based calibration scheme are used in various ProtoDUNE-SP physics analyses including Michel energy spectrum, π^0 energy reconstruction studies, electron shower energy reconstruction. Figure 3.21 show the results of muon based calibration applied to protons. The plots are taken from ProtoDUNE-SP performance paper[26]. The study demonstrates the calibration scheme can be applied to any LArTPC with enough cosmic ray muons incident and valid for any particle species. The charge calibration procedure requires a good detector coverage in a short period which may not be possible for DUNE, while we may use laser beam to perform

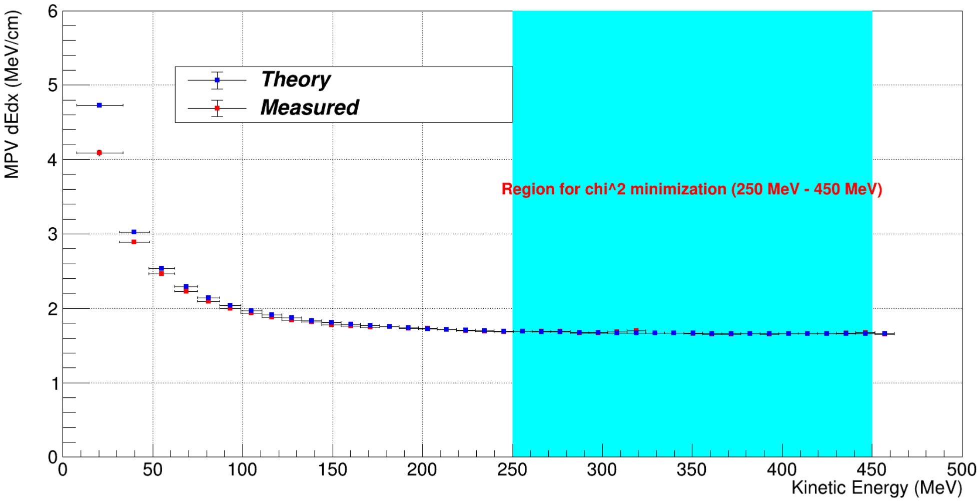

(a) Data run 5770

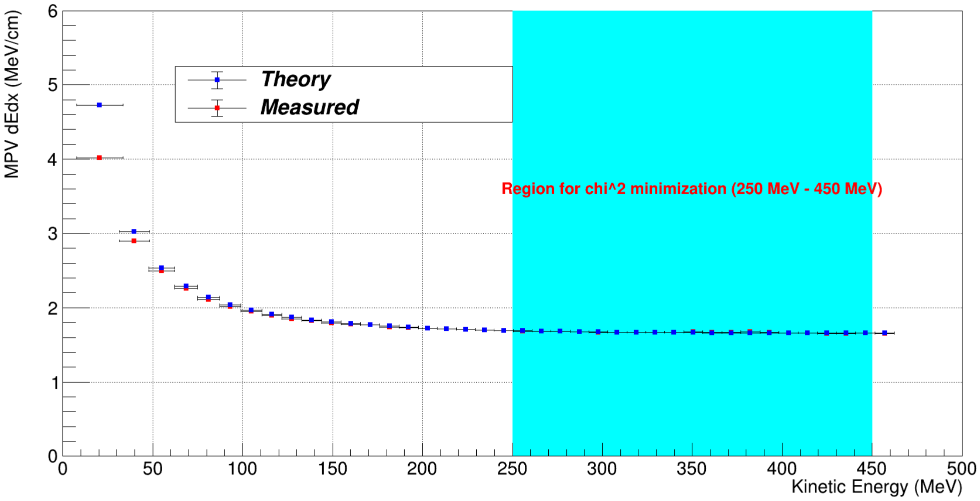

(b) Monte-Carlo

Figure 3.19: Most probable dE/dx compared to Landau-Vavilov theory for data run 5770 (a) and Monte-Carlo simulation (b).

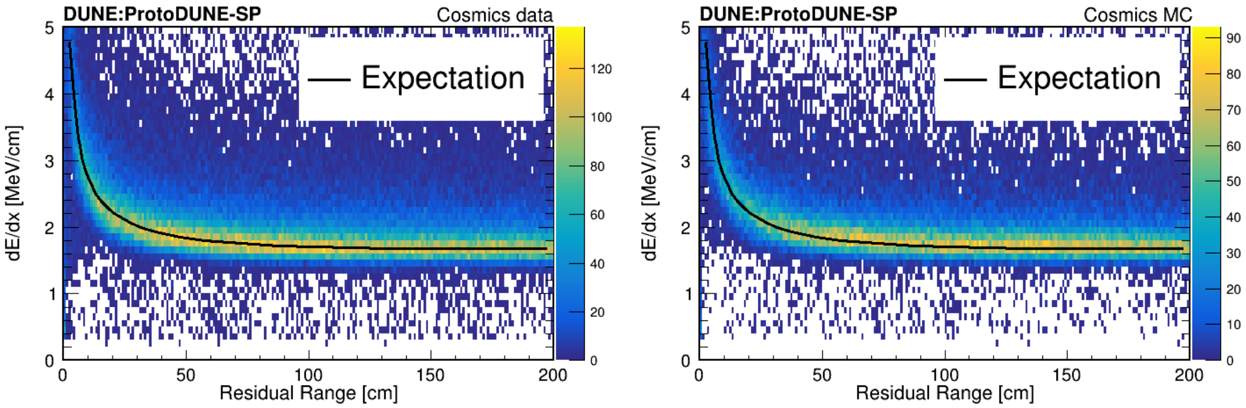

(a) Data (b) MC

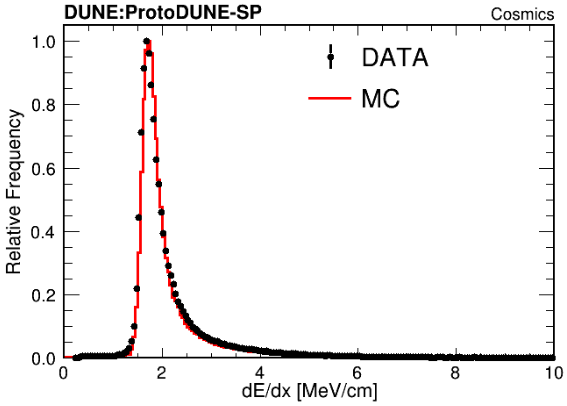

(c) dE/dx comparison

Figure 3.20: Stopping muon dE/dx distributions for the ProtoDUNE-SP cosmic-ray data and MC. The black curves in a and b are the predicted most probable values (using the Landau-Vavilov function) of dE/dx versus residual range and c is the dE/dx distribution for the stopping muon sample. The histograms in c are normalized such that the maximum frequency is one. The plots are taken from ProtoDUNE-SP performance paper[26].

a similar analysis in DUNE. However, for the energy scale calibration, we require only a few 100 stopping muon tracks which enable the scheme to be directly exported to DUNE.

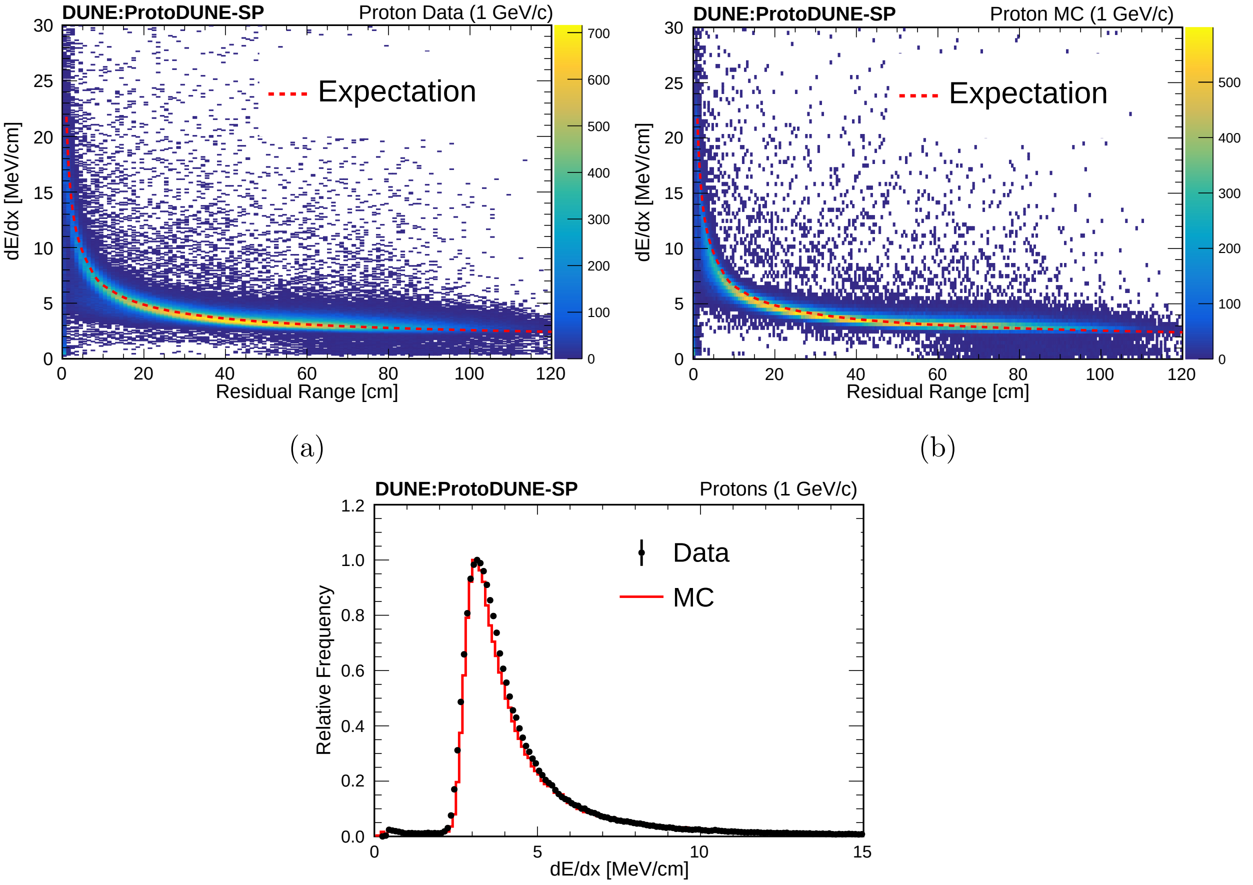

(a)

(b)

(c)

Figure 3.21: Stopping proton dE/dx versus residual range distributions for the ProtoDUNE-SP beam data a and MC b, the expected most probable values are shown in red. The dE/dx distributions after the SCE corrections of data and MC are shown in c. The histograms in c are normalized such that the maximum frequency is one. The figures are taken from the ProtoDUNE-SP performance paper [26]

Chapter 4

Electron drift velocity measurement in ProtoDUNE-SP

Section 3.1.1 discusses in details the impact of space charge effect (SCE) on a particle trajectory in the ProtoDUNE-SP detector. In addition, SCE distorts the energy reconstruction. As ProtoDUNE-SP is built at the surface of the earth, a large number of cosmic muons pass through the detector each second[72]. Although SCE distorts the position and energy reconstruction of a particle passing through the medium on the other hand this provides an opportunity to study the effect space charge makes on a surface LArTPC. ProtoDUNE-SP has two sets of anode plane assemblies (APAs) which makes it a particularly useful detector to have a direct measurement of the effect of space charge. Several current LArTPCs are operating, and others are being build or planned at the surface of the earth including MicroBooNE[83], ICARUS[39], SBN[84] near detector to name a few. DUNE near detector will also be built at the surface of the earth. The techniques developed in protoDUNE-SP will be immensely useful to have a better understanding of the effect of space charge on the surface LArTPCs. In this chapter, I will discuss a novel technique that I developed to measure the electron drift velocity in the presence of the space charge effect.

4.1 Theoretical estimate of space charge effect for ionization detectors

The theoretical treatment of SCE is based on the study of space charge in ionization detectors[85]. The first study of the effect of the varying distribution of electric field was considered by Child[86] and Langmuir[87]. They studied the effect of spatially varying distribution of free electrons on the operation of a vacuum diode. In a simplified approach, the electric field variation only along the drift direction is considered, which will be along the direction of the applied electric field in the case of positive ions. Let the positive-ion space-charge density be ρ(x), the magnitude of the stable state electric field is E(x), and K is the ion pairs created per cm^3 of the detector per sec. The positive ion drift velocity is given by, v(x)=$\mu E(x)$, where μ is the positive ion mobility. The ion drift velocity is around 5 orders of magnitude lower than the electron drift velocity[75–77]. Although an equal number of electrons and ions are produced by incident cosmic muons, the electrons quickly get collected to the anode leaving behind a net positive charge density. The continuity equation is modified to,

$$\nabla \cdot \mathbf{J} + \frac{\partial \rho}{\partial t} = K \tag{4.1}$$

where $\mathbf{J}$=$\rho\mathbf{v}$ is the positive ion current density. For the steady-state condition, considering the variation of the electric field to be only along x direction, the equation 4.1 reduces to,

$$\frac{\partial \rho v(x)}{\partial x} = K \tag{4.2}$$

From the Maxwell equation (in MKS units) we have,

$$\nabla \cdot \mathbf{E} = \frac{dE}{dx} = \frac{\rho}{\epsilon} \tag{4.3}$$

The detailed solution of the equations above is discussed in space charge in ionization detectors[85], the final expression for E(x) we obtain is,

$$E(x) \approx E_A[1 + \frac{1}{2}.(\frac{\alpha E_0(D-x)}{E_A D})^2] \tag{4.4}$$

where E_A is the electric field at the anode,

E_0 is the nominal electric field applied between the cathode and the anode which is $\approx$ 500 V/cm in case of ProtoDUNE-SP,

D is the distance between the cathode and the anode which 3.6 m for ProtoDUNE-SP,

x is the distance from the cathode,

α is a dimensionless parameter given by,

$$\alpha = \frac{D}{E_0}\sqrt{\frac{K}{\epsilon\mu}} \tag{4.5}$$

where ϵ is the dielectric constant of liquid argon and μ is the positive ion mobility. At a nominal field of $E_0 = 0.5\ kV/cm$ the value of α for a LArTPC built at the surface of the earth is $\approx$ 0.18D[85;88]. Using equation 4.4 the electric field as a function of distance from the cathode is shown in figure 4.1. The electric field at the anode is $\sim$ 16% lower and the electric at the cathode is $\sim$ 10% higher than the nominal value of 500 V/cm. The electric field measured can be used to estimate the drift velocity of electrons in liquid argon as discussed in the LArSoft package[74]. However, there are some uncertainties in the factors which affect the electric field calculation including K, μ, E_0. The treatment here ignores the transverse component of the electric field, the assumption although reasonable is completely valid only for the case of an infinite size detector. In addition, the flow of liquid argon in the detector also affects the drift velocity of ionization electrons. Considering, all these factors the direct data-driven measurement of the electron drift velocity and the electric was carried out, which will be discussed in the next section.

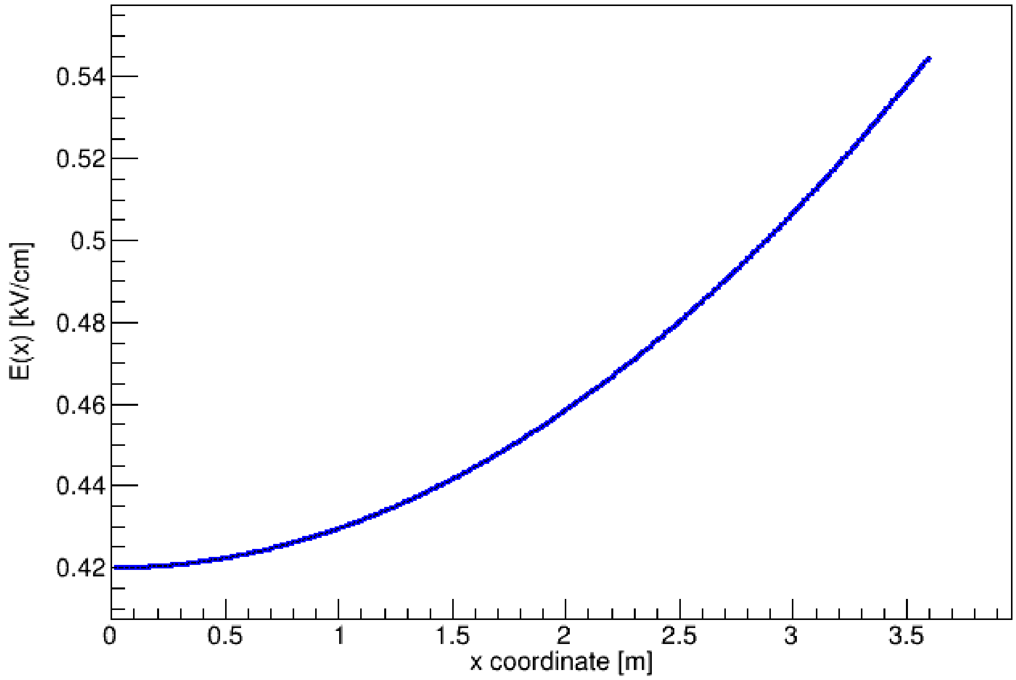

Figure 4.1: Theoretical prediction[85] of E(x) in the presence of SCE in ProtoDUNE-SP detector. Here, x=0 corresponds to the CPA location and x=3.6 m corresponds to APA location.

4.2 Data-driven drift velocity measurement

For the drift velocity measurement, I use a sample of anode-cathode-anode crossing tracks. These tracks are special in the sense that their start and endpoints are undistorted by SCE. The selection procedure for such tracks and the method for drift velocity measurement is described as follows:

4.2.1 Event selection

ProtoDUNE-SP detector has two drift volumes, one on either side of the cathode. If a particle passes through the two drift volumes the ionization electrons drift to the anode on the same side of cathode in which they are liberated. The y and z position of the hits in the track is reconstructed based on the anode wire where the signal is received, the x position of the hits is reconstructed based on the time of the peak of the hit, t_{hit}. Pandora reconstruction algorithm[89] is used in the LArSoft framework[90] for reconstruction of the incident particle trajectory. The x position is reconstructed using the relation,

$$x = x_{\text{anode}} - v_{\text{drift}} \times t_{\text{drift}},\ \ for\ x > 0\ region \tag{4.6}$$

$$x = -(x_{\text{anode}} - v_{\text{drift}} \times t_{\text{drift}}),\ \ for\ x < 0\ region \tag{4.7}$$

where x_{anode} is the x coordinate of the anode on $x > 0$ region, $\approx 360\ cm$, for ProtoDUNE-SP,
v_{drift} is the nominal drift velocity,
t_{drift} is time taken by a hit to reach the anode = t_{hit}-t_0, t_0 being the time at which the particle enters the TPC.

In a LArTPC the t_0 for a track can be determined based on the scintillation light signal received on the photon detector system as a particle passes through the medium, however, there could be some ambiguity in the t_0 measured from the scintillation light as there are many cosmic muons incident in an event. There are other techniques developed for measuring the t_0 for tracks crossing the cathode[26], but the efficiency of t_0 estimation is low for tracks incident in a certain region of the TPC. In the case of successful t_0 reconstruction the track segments in the two sides of the cathode are stitched together. In the lack of knowledge of t_0, the track segment on the two sides of the cathode does not line up even in the absence of SCE. Figure 4.2 is a cartoon showing the reconstruction of a track with unknown t_0 and passing through the two drift volumes. I first select the tracks with known t_0, for the tracks with unknown t_0 I developed a technique to stitch the tracks with passes through the two anodes and the cathode. Below, I discuss in details the technique to stitch and select anode-cathode-anode tracks:

1. In each event, I select tracks that are confined to only one drift volume, either $x < 0$ or $x > 0$ drift volume. This is done using the TPC number of each hit in the track. For hits in the $x > 0$ volume, possible TPC numbers are 2, 6, or 10 while for hits in $x < 0$ volume TPC numbers can be 1, 5, or 9.

2. Corresponding to a track segment in (1) I search for a matching track segment in the

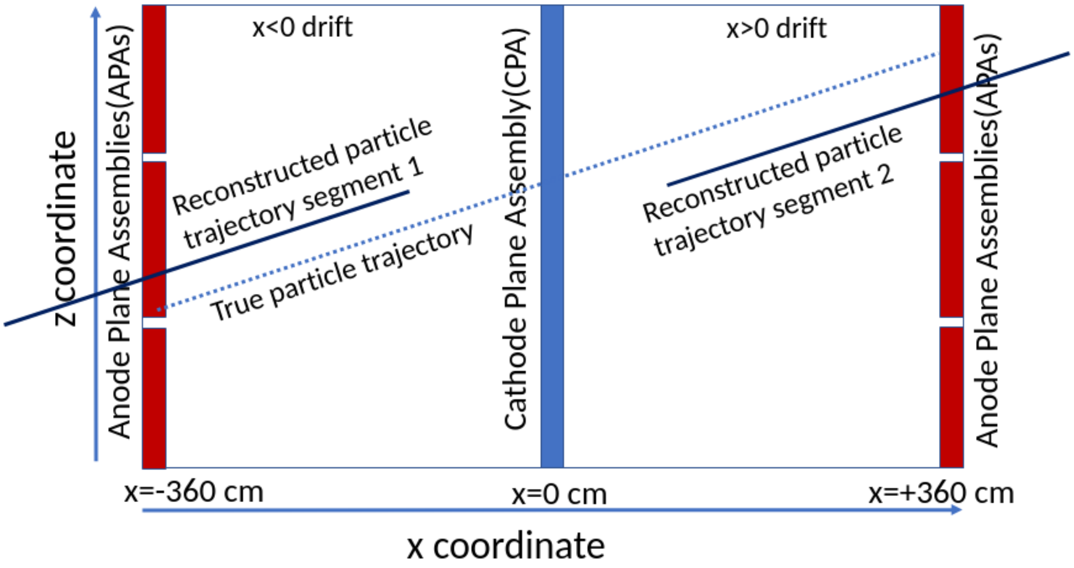

Figure 4.2: Figure shows the xz projection of the TPC (top view), the dotted line represents the true trajectory of a particle passing through the medium and the two tracks segments parallel to the true trajectory represent the reconstructed track if t_0 is unknown.

other drift volume as described in the next steps.

3. A particle passes through the TPC at a speed close to the speed of light and produces ionization electrons simultaneously along its path. However, electron drift velocity is much smaller compared to the speed of light which causes the electrons liberated nearest to the anode to take the least time to reach the anode. For particles passing through the two APAs, we receive first signals at the two anodes nearly simultaneously. Figure 4.3 shows the difference in $t_{\rm hit}$ at the anode for the pair of tracks on the two drift volumes in an event. If we can find a segment in the other drift volume whose minimum $t_{\rm hit}$ is within 5 ticks of the track in (1) we carry on to other selection requirements, otherwise we start from step (1).

4. The anode-cathode-anode crossing tracks have to travel the entire drift distance of the TPC. In figure 4.4 $t_{\rm min}$ and $t_{\rm max}$ represents the time taken to reach the APA for the hit closest to anode and the hit closest to cathode respectively and ΔT = $t_{\rm max}$-$t_{\rm min}$. If we add the ΔT values on the two sides of the cathode for a track(ΔT_1+ΔT_2), we will get maximum possible value for anode-cathode-anode crossing tracks as they have to

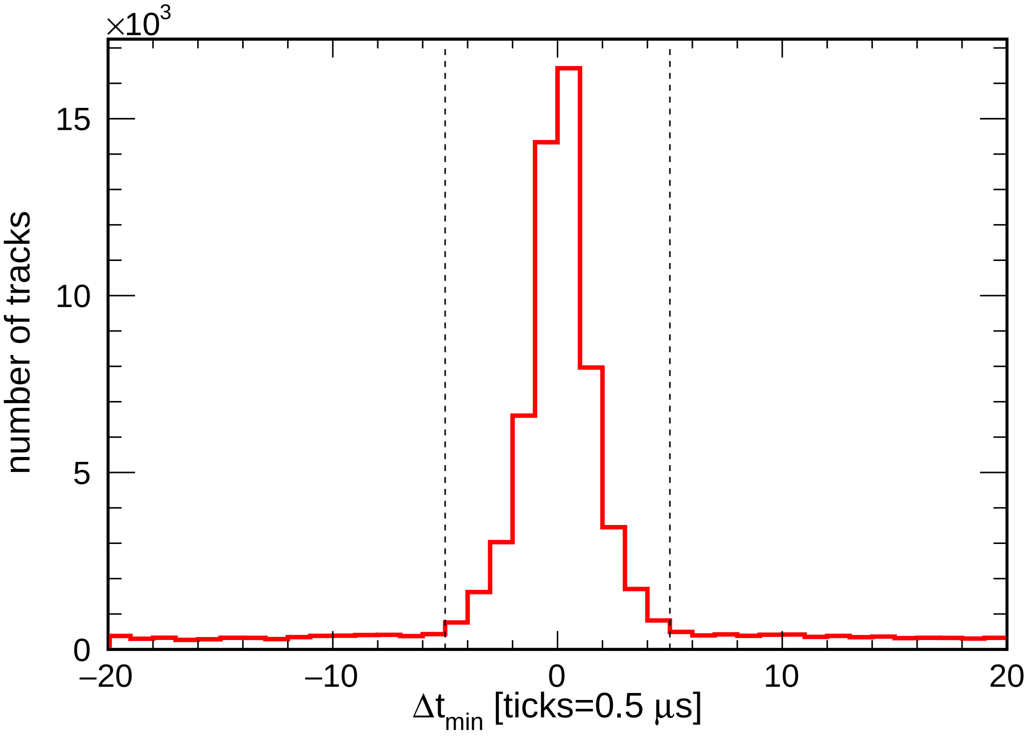

Figure 4.3: Figure shows the distribution of the difference in minimum t_{hit} for track segments in an event in two drift volumes (t_{min} for $x > 0$ minus the t_{min} for $x < 0$). If the track segments belong to the same particle Δt_{min} should be close to 0. I select track segments with absolute value of Δt_{min} less than 5 ticks. The plot is made using cosmic ray muons in the ProtoDUNE-SP beam runs.

cover the entire drift volume. Figure 4.5 shows the value of $\Delta T_1+\Delta T_2$ for all tracks passing through the two drift volumes. Based on the distribution we select tracks with $\Delta T_1+\Delta T_2$ value between 9180 ticks to 9220 ticks (4590μs to 4610 μs).

5. For a track crossing the anode, t_0 is the same as t_{min} in a drift volume, which enables us to reconstruct the x coordinate of the hits in the trajectory. However in the presence of SCE, the reconstructed x position based on equation 4.6 or 4.7 is distorted. In the absence of SCE, the ends of the track closer to the cathode should meet each other after position reconstruction, ignoring the 3 mm thickness of the CPA panel. In the presence of SCE, the two segments can only get close to each other and will often not line up. Figure 4.6a shows the 3D distance between points closest to cathode on the two drift volumes and figure 4.6b shows the 3D distance after implementing selection criteria in

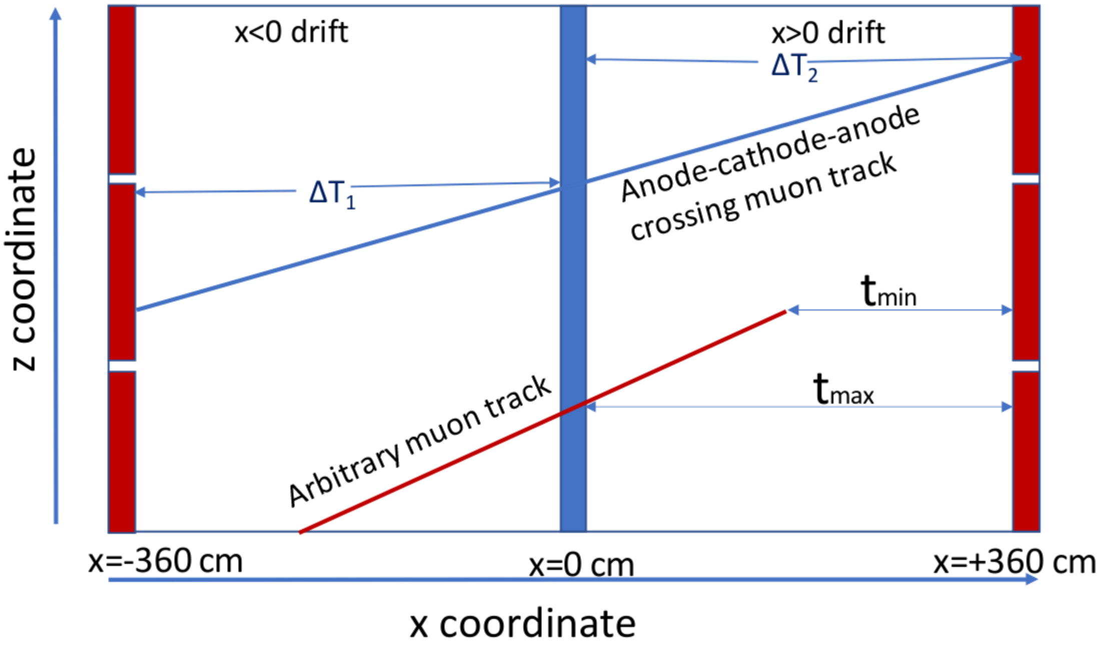

Figure 4.4: Figure shows the xz projection of the ProtoDUNE-SP TPC. We can see the sum of the difference between the maximum (t_{max}) and minimum peak times (t_{min}) is maximum possible for anode-cathode-anode tracks. We use this characteristics of anode-cathode-anode tracks for their selection.

item (1)-(4). I select tracks with a 3D distance less than 20 cm as anode-cathode-anode crossing track.

The tracks passing the selection requirements (1)-(5) are used for drift velocity calculation, discussed in subsequent sections.

4.2.2 Reconstructing true X position

In a LArTPC we have a direct measurement of the wire coordinates and the peak time for each hit on a track (t_{hit}). We can determine the y and z position of a hit based on the APA wire where the hit arrives, however, there is no direct measurement of the x position of a hit in a LArTPC. While we directly measure the peak times for each hit, x position reconstruction requires a known drift velocity at each point inside the TPC. The goal of this study is to determine the drift velocity as a function of x. For our selection of tracks, we know the coordinates of the start and the endpoint on a track precisely. The true trajectory

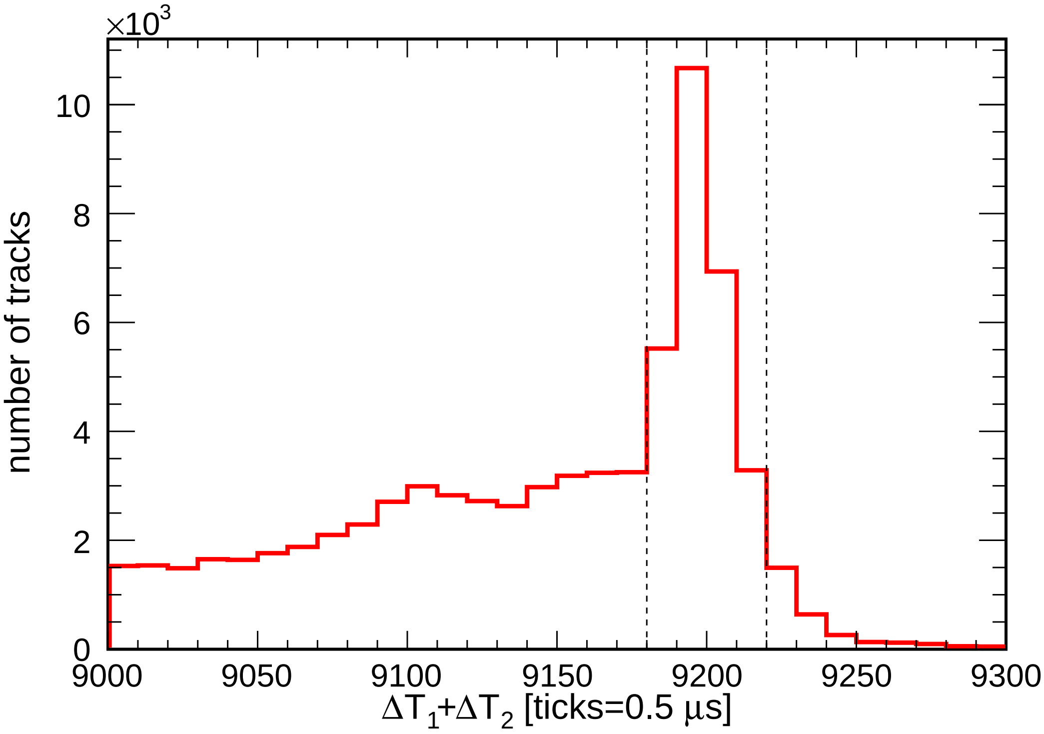

Figure 4.5: Figure shows sum of the difference between the maximum (t_{max}) and minimum peak times (t_{min}) for the track segments in the two drift volumes. The peak region between the dotted lines corresponds to the anode-cathode-anode tracks. The plot is made using cosmic ray muons from the ProtoDUNE-SP beam runs which consist of over 700,000 events.

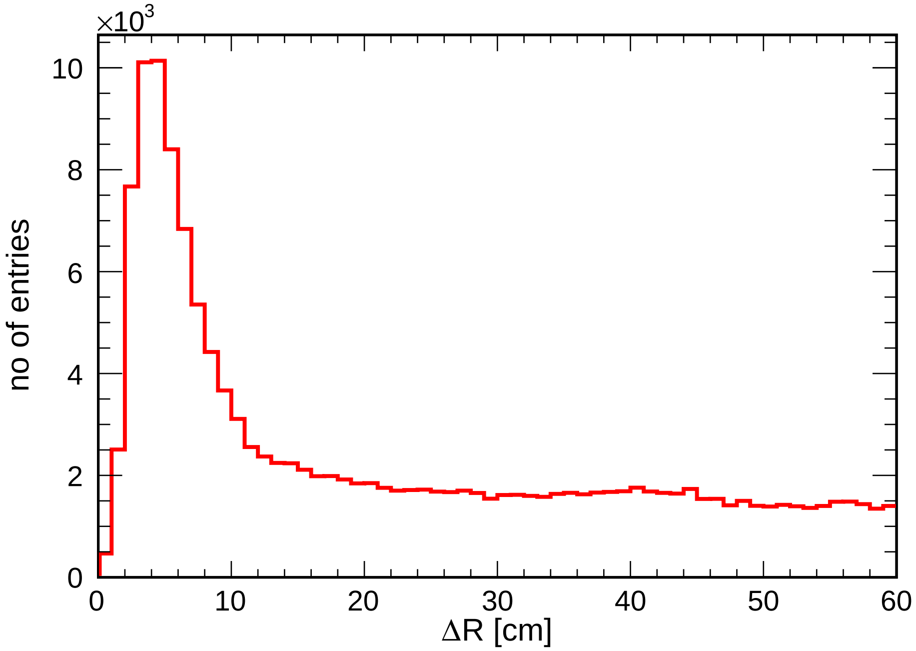

(a) Before any selection requirement.

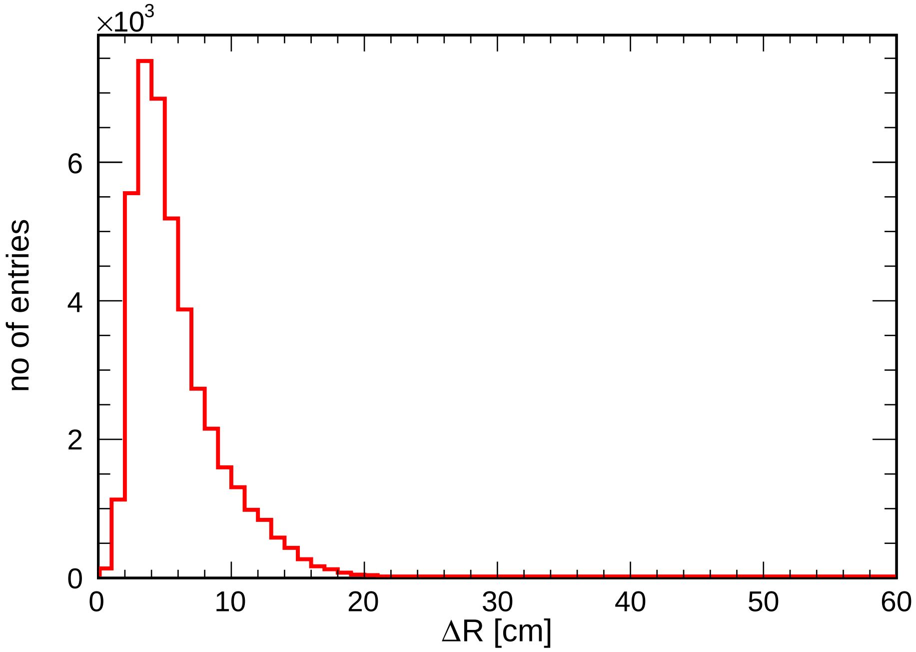

(b) After selection requirement (1)-(4).

Figure 4.6: Figure (a) shows the distance between the reconstructed track ends closer to cathode before any selection requirement and figure (b) shows the same distribution for tracks passing the selection requirement (1)-(4).

of the cosmic muon is a nearly straight line, considering the effect of multiple Coulomb scattering averages out over time. For a straight track, knowing the y or z coordinate of a hit, we can determine the corresponding x coordinate of the hit using the equation of a straight line. Figure 4.7 demonstrates the reconstruction of x coordinate using z coordinate, which is given by the coordinate of collection wire where the hit is detected. Points A(x0, y0, z0) and B(x1, y1, z1) are the start and endpoints on a track respectively and are precisely known. Let P(x, y, z) be any arbitrary point on the track, knowing z we can determine x using the relation,

$$x = x1 + \frac{(x1 - x0) \cdot (z - z1)}{z1 - z0} \tag{4.8}$$

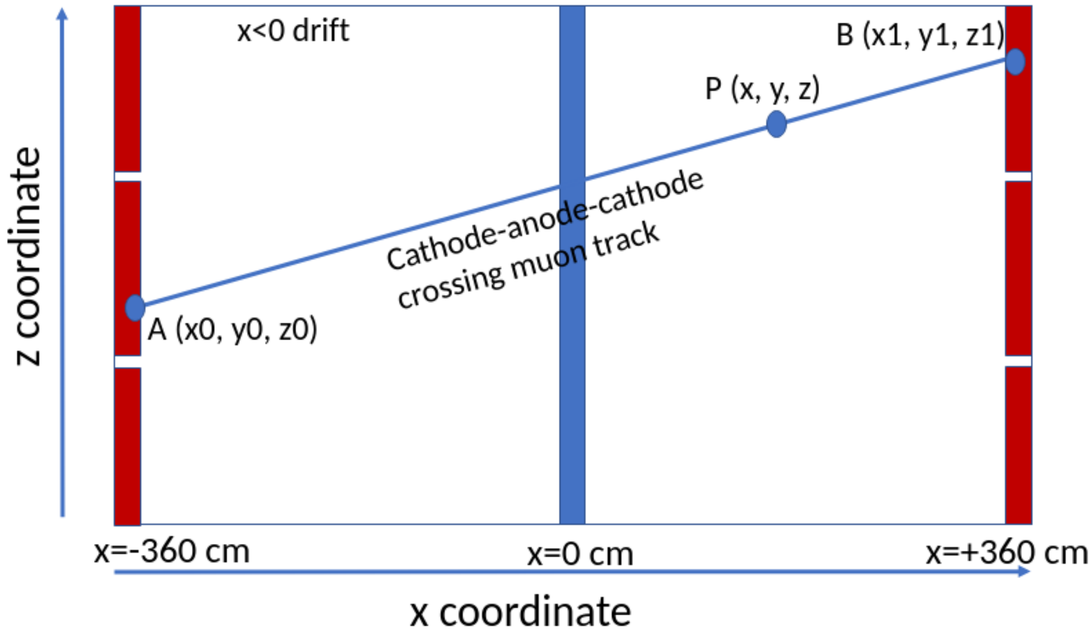

Figure 4.7: Figure shows the xz projection of an anode-cathode-anode track, knowing the z position of a hit (which is known from collection wire in which the hit is detected) we can determine the x position using the equation of a straight line.

The reconstructed tracks are distorted by SCE causing the straight-line approximation to be reconsidered. However, we can remove the effect of SCE distortion on tracks by finding out the magnitude of SCE distortion in different parts of the TPC. I estimated the SCE distortion inside the TPC using anode-cathode-anode tracks. The procedure uses a pair of tracks crossing each other in the TPC, the technique was initially developed in the

MicroBooNE experiment to determine SCE distortion map[91;92]. In addition, ProtoDUNE-SP has two anode planes which enable us to determine both the start and endpoints on the trajectory precisely unlike in most LArTPC's which have a single anode plane. In the next section, I am discussing the method for measuring the SCE distortion using anode-cathode-anode tracks.

4.2.3 SCE distortion map using anode-cathode-anode tracks

Figure 4.8 shows a pair of tracks that intersect each other. From a collection of anode-cathode-anode tracks during the protoDUNE-SP beam run, I select all pairs of tracks that cross each other or pass very close to each other in 3D space. We know the undistorted start and endpoints for the selected tracks as they pass through both the anodes. The true trajectory is determined using the start and endpoints of the track. The reconstructed trajectory is determined using the measured y, z position and hit peak time (for x reconstruction). True intersection point, P'(X, Y, Z) in figure 4.8, is found using the equation of a straight line in 3D space. The reconstructed intersection point is estimated by measuring the distance between reconstructed hits in the two tracks. The pair of reconstructed hits (one from each track) with the shortest distance between them given the point of intersection for the reconstructed tracks, P(x, y, z) in figure 4.8. For each pair of intersecting or near intersecting tracks, it is evident that the SCE has caused the point P' to be reconstructed at point P. The distortion due to SCE can be measured by subtracting reconstructed intersection coordinate from true intersection coordinate given by,

$$\delta_{\mathrm{x}} = X - x \tag{4.9}$$

$$\delta_{\mathrm{y}} = Y - y \tag{4.10}$$

$$\delta_{\mathrm{z}} = Z - z \tag{4.11}$$

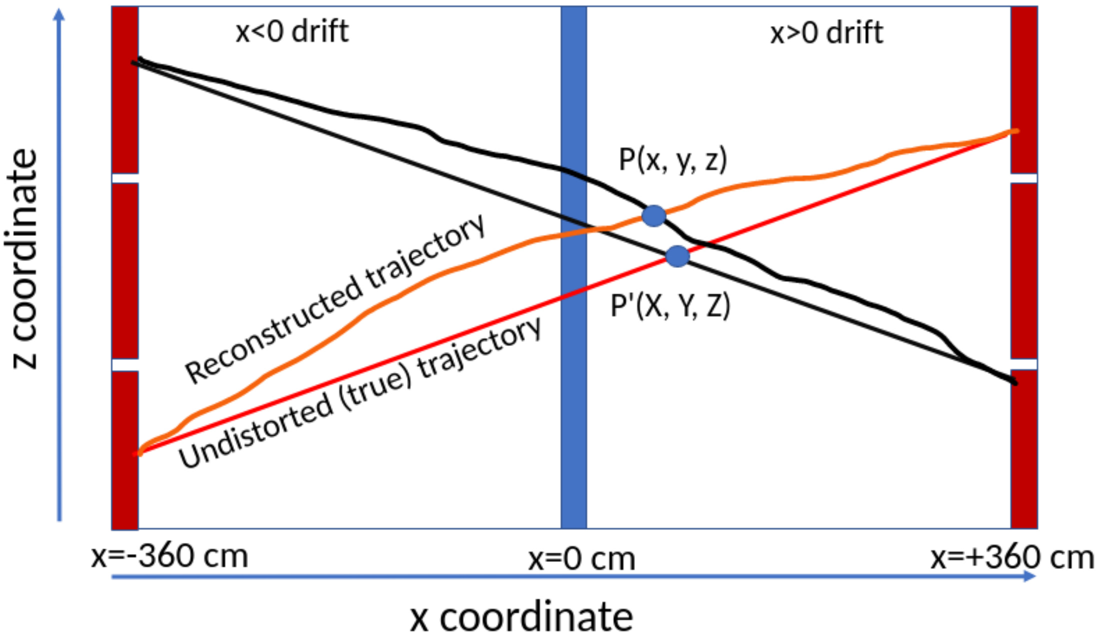

Figure 4.8: Figure shows the 2D projection of a pair of anode-cathode-anode tracks intersecting each other in 3D space. The point P' corresponds to the true point of intersection and point P corresponds to the reconstructed point of intersection.

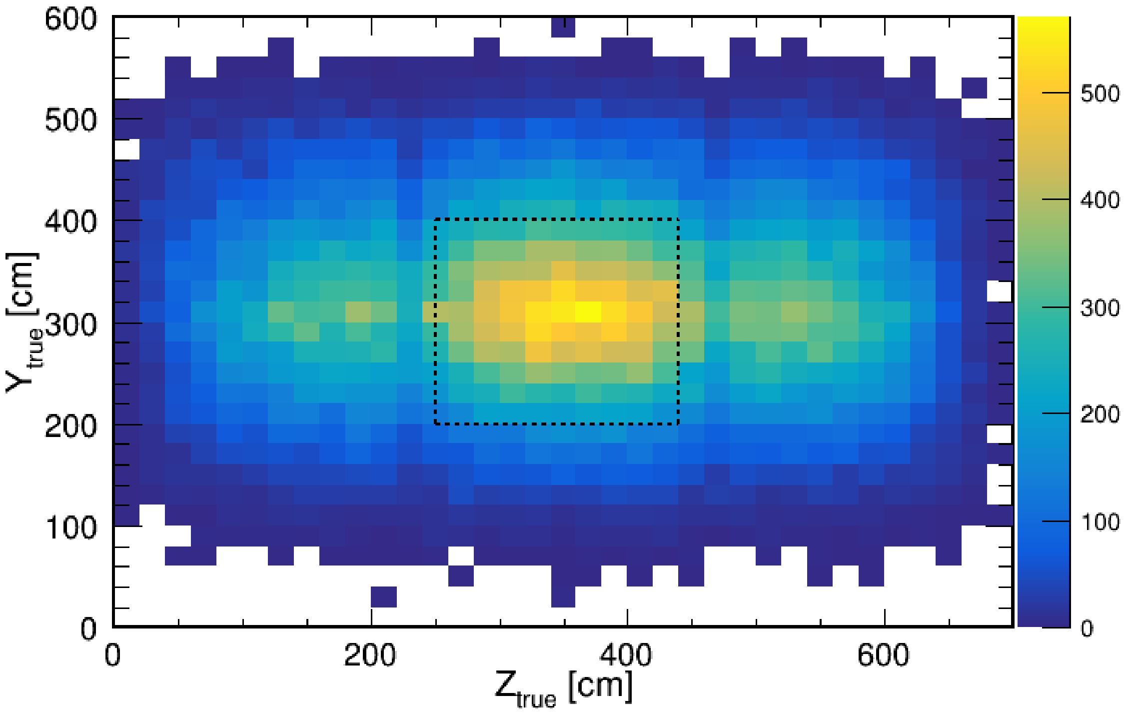

Figure 4.9: In figure the color scale shows the number of cathode-anode-cathode tracks passing through each 20 cm × 20 cm bin along yz plane at the CPA. For the drift velocity calculation only the region bounded by the dotted lines is chosen owing to better statistics.

Figure 4.9 shows the coverage map of anode-cathode-anode tracks as they pass through the CPA. The whole CPA has been divided into 20 cm× 20 cm bins along y and z direction. The color scale shows the number of tracks passing through each bin. As we go inside the TPC the number of incident tracks increases. For the estimation of SCE distortion, I divide the whole TPC into 20cm bins along y and z and 40 cm bins along x. With finer bin size we can determine the distortion more accurately, however, due to statistical limitations wider bins are chosen. Along the x coordinate the distortion is approximately linear so I am choosing a slightly wider bin size along x to increase statistics in each bin. I used $\approx$ 700,000 events to make the SCE map, with around 60,000 anode-cathode-anode tracks selected. Each pair of intersecting tracks gives a value of SCE distortion at the point of intersection. From a collection of all intersecting tracks, we have SCE distortion values covering the entire TPC except the regions near the TPC boundary. For each bin median x, y, z distortions δ_x^{median}, δ_y^{median}, δ_z^{median} are determined. Figure 4.10 shows the Z distortion distribution for some selected bins. The median value of the distribution is taken as the Z distortion corresponding to the bin, the median is chosen as some bins have low entries where the mean value can be affected by a few outliers. Figure 4.11 demonstrates the variation of z distortion as a function of x for fixed y (420 cm) and z (550 cm) coordinates. As expected the distortion in z decreases as we get closer to the anode on both sides of the cathode.

Using the distortion map we can determine the undistorted trajectory (true trajectory) of a particle by removing the distortion using the SCE distortion map. The true X, Y, Z coordinates for a reconstructed hit with reconstructed coordinates x, y, and z is estimated using,

$$X = x + \delta_{\mathrm{x}}(x, y, z) \tag{4.12}$$

$$Y = y + \delta_{\mathrm{y}}(x, y, z) \tag{4.13}$$

$$Z = z + \delta_{\mathrm{z}}(x, y, z) \tag{4.14}$$

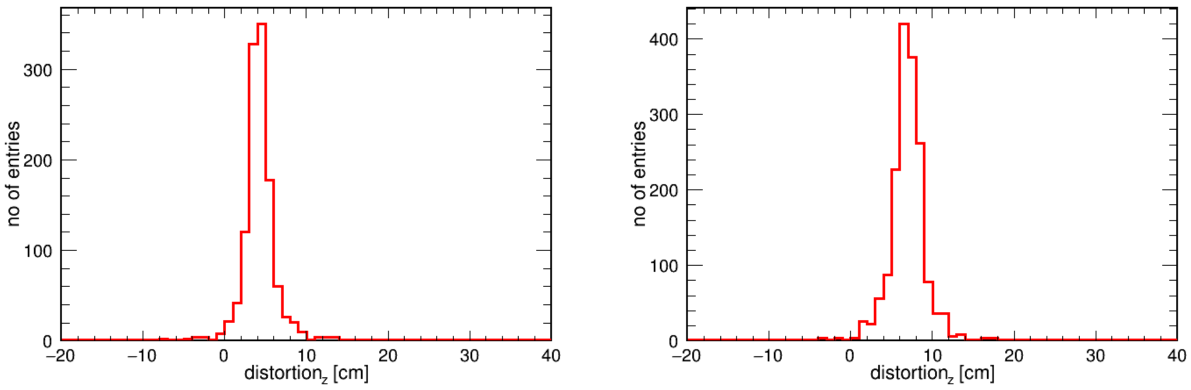

(a) $x > 0$ (b) $x < 0$

Figure 4.10: Figure (4.10a) shows the distribution of measured z distortion for bin with $0 < x < 40$, $400 < y < 420$ and $540 < z < 560$, the Gaussian fitted mean value of the distribution is 4.16 cm and standard deviation of 1.3 cm, Figure (4.10b) represents the Z distortion for bin with $-40 < x < 0$, $400 < y < 420$ and $540 < z < 560$, the Gaussian fitted mean value of the distribution is 6.96 cm and standard deviation of 1.57 cm.

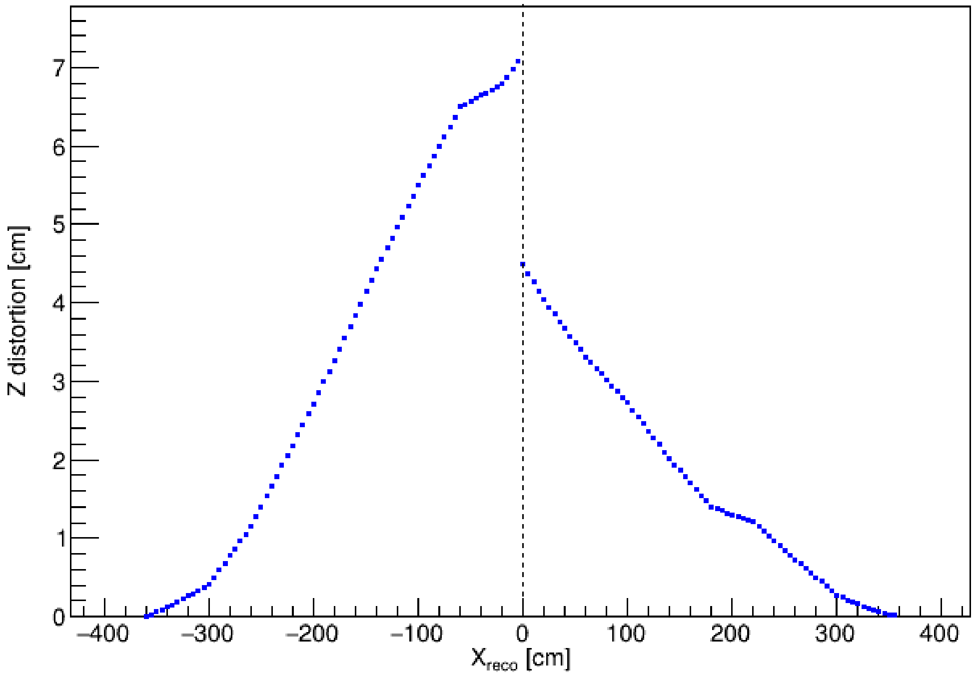

Figure 4.11: Figure shows the z distortion as function of x coordinate with fixed y =420 cm and z = 550 cm. The figure shows the magnitude of SCE distortion is different on the two drift volumes.

Using the SCE correction the undistorted or true trajectory of a particle can be determined. Once we have the true trajectory of the particle, using equation 4.8 the true x position of the particle is determined using the corrected z position.

4.2.4 Drift velocity measurement methodology

In the previous section I discussed a technique for the measurement of the true x position of the hits in an anode-cathode-anode crossing track. At the same time we do have a direct measurement of the time of arrival of the signals at the anode (t_{hit}). The drift time for each hit can be calculated using equation 4.15,

$$t_{\text{drift}} = t_{\text{hit}} - t_0 \tag{4.15}$$

where $t_0 = t_{\text{min}}$ for anode-cathode-anode crossing tracks.

For each track, we now have a collection of true x position and measured drift times, t_{drift}. We divide the whole drift distance of 720 cm (-360cm to +360cm in x), into 36 bins of width 20 cm each. For each bin, the segment of a track lying within a bin is selected, and x vs t_{drift} distribution is fitted to a polynomial of the first order as shown in figure 4.12. The drift velocity is by definition the change in drift distance as a function of drift time, which can be obtained from the slope of the fit for x vs t_{drift} histogram. Figure 4.12 shows x vs t_{drift} plots for some randomly chosen track segments. Each track segment confined in a bin gives a value of local drift velocity for that bin. For each bin in x we have a distribution of drift velocities based on the values from different track segments, figure 4.14 shows the drift velocity distribution for one such bin. We calculate the median drift velocity for each bin which is shown in figure 4.13.

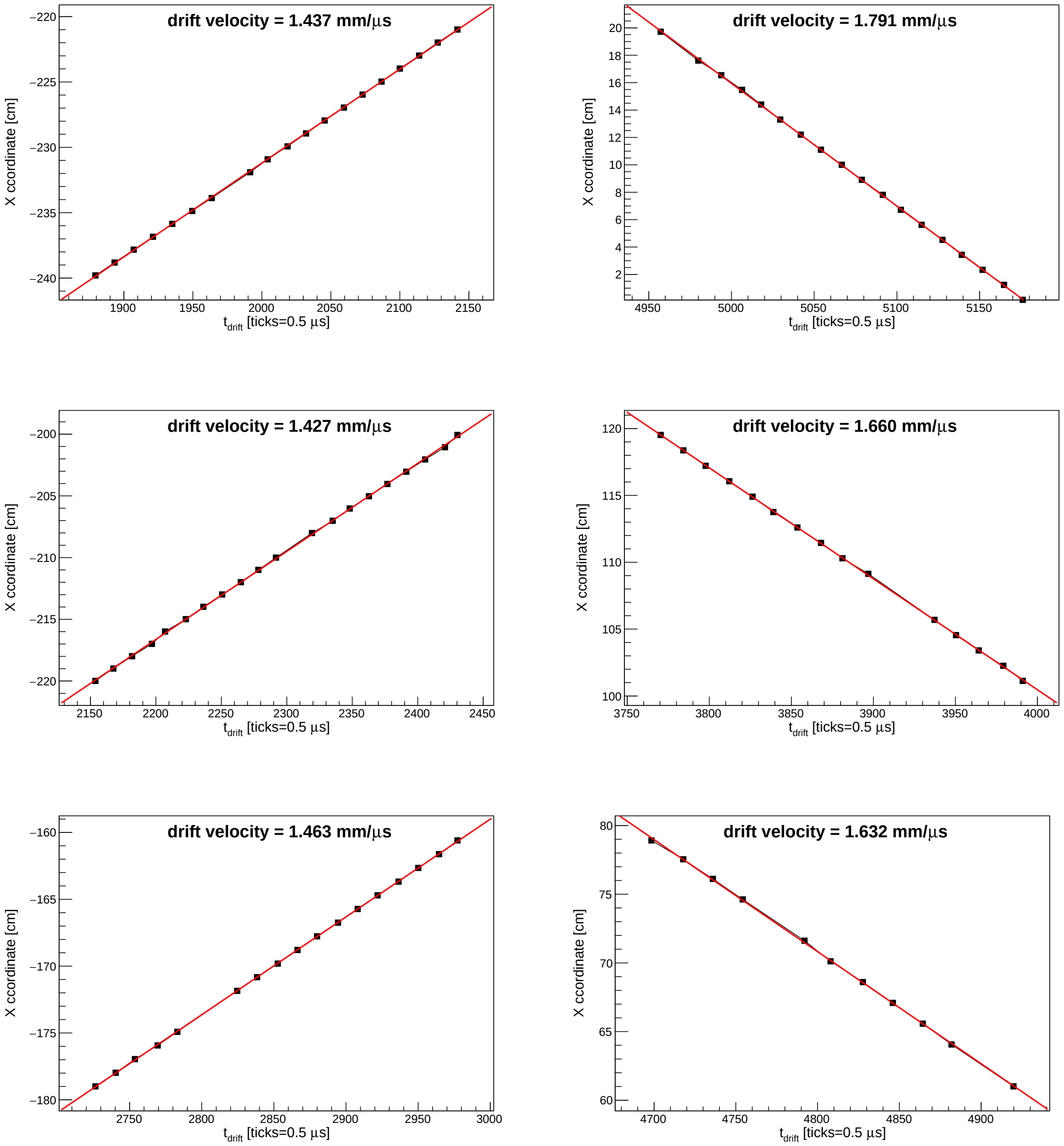

Figure 4.12: Figure shows x vs drift time distribution for some randomly chosen track segments, the plots are fitted to a polynomial of first order to obtain the local drift velocity.

4.2.5 Statistical uncertainty in measured velocity

Figure 4.14 shows the velocity distribution for the bin with x between 340 cm to 360 cm. There are some entries with very high or very low drift velocities, which are mainly caused

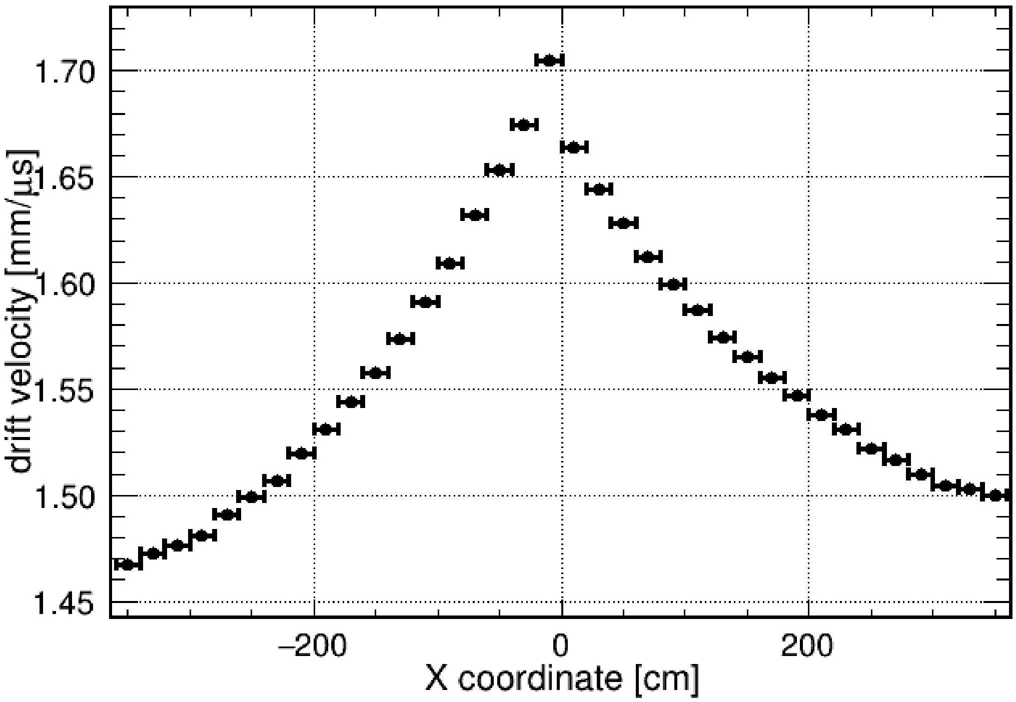

Figure 4.13: Figure shows the measured drift velocity as function of x coordinate. The data consists of all the ProtoDUNE-SP beam runs comprising of over 700,000 event. The drift velocity is averaged over the central region of TPC with 200 $cm < y <$ 400 cm and 250 $cm < z <$ 440 cm.

by factors including poor reconstruction, multiple Coulomb scattering. The outliers can affect the mean of the distribution so a median value gives more reasonable results. The standard uncertainty (1σ or 68% confidence interval) on a median would be $0.5\pm\ \frac{1}{2\sqrt{N+2}}$ quantiles[93;94], where N is the number of entries in the distribution. The error bars in the median drift velocity and electric field plots are estimated using $0.5\pm\ \frac{1}{2\sqrt{N+2}}$ quantiles. Once

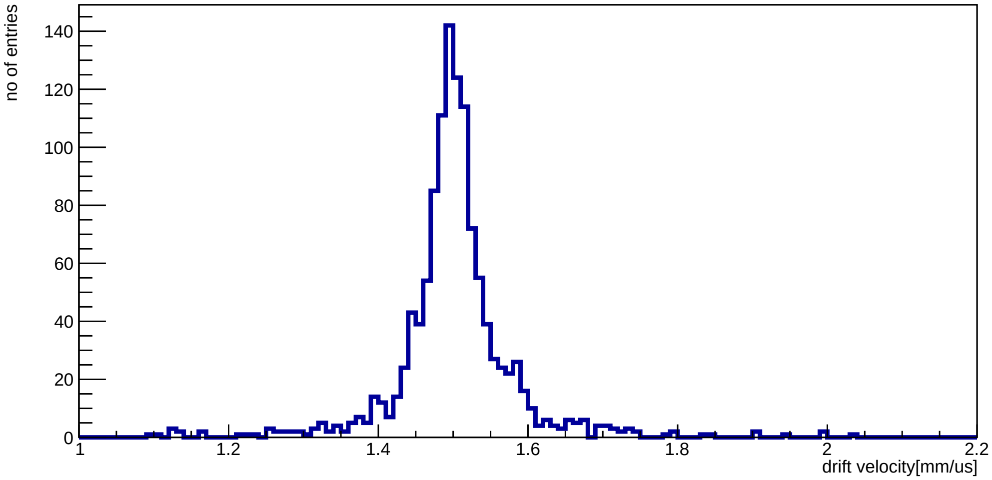

Figure 4.14: Figure shows shows the distribution of drift velocity for a bin with $340\ cm < x < 360\ cm$. The median value of the distribution is calculated along with the error in median. The results for all such distribution is shown in figure 4.13.

we measure the drift velocity we can measure the electric field as described in the next section.

4.3 Drift electric field using measured drift velocity

In ProtoDUNE-SP, the cathode-anode nominal potential difference is ≈ 180 kV which is equal to 0.5 kV/cm for a drift distance of 3.6 m. However, there is some uncertainty and fluctuation in the applied electric field, the average electric field applied during the ProtoDUNE-SP beam run was found to be ∼0.4867 kV/cm. For a given electric field the electron drift velocity depends on the temperature of the medium. The average temperature during the ProtoDUNE-SP beam run was 87.68 K. There have been past studies to relate electron drift velocity to drift electric field in liquid argon by Walkowiak[73] and ICARUS experiment[39]. The relation is in a parametric form and depends on temperature as well. Here, I am using a package used in LArSoft to convert drift velocity into drift electric field and vice versa[74]. Figure 4.15 shows the relation between electric field and drift velocity at a temperature of 87.68 K, a LArSoft package[74] was used to draw the plot.

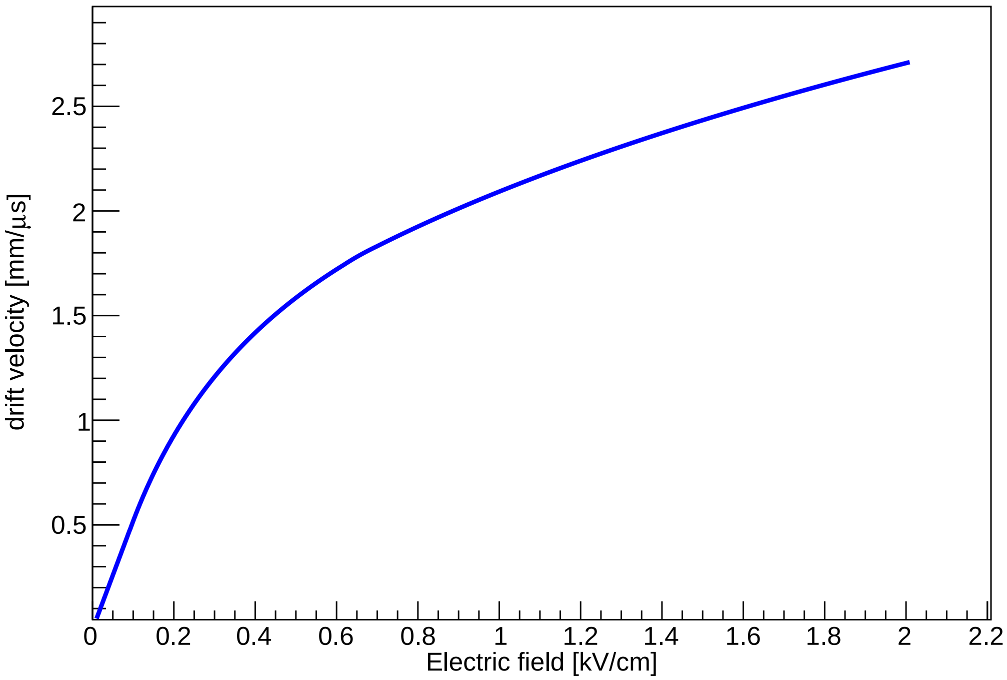

Figure 4.15: Figure shows drift velocity as a function of electric field for a fixed temperature of 87.68 K. The plot is drawn based on a LArSoft package[74].

Using the relation between drift velocity and electric field, we can convert the measured drift velocity into the electric field. Figure 4.16 shows the electric field as a function of drift coordinate, obtained from drift velocity.

4.4 Results and conclusion

In ProtoDUNE-SP, the space charge effect distorts the electric field and the drift velocity. Distortion in drift velocity and electric field distorts the particle trajectory as well as the

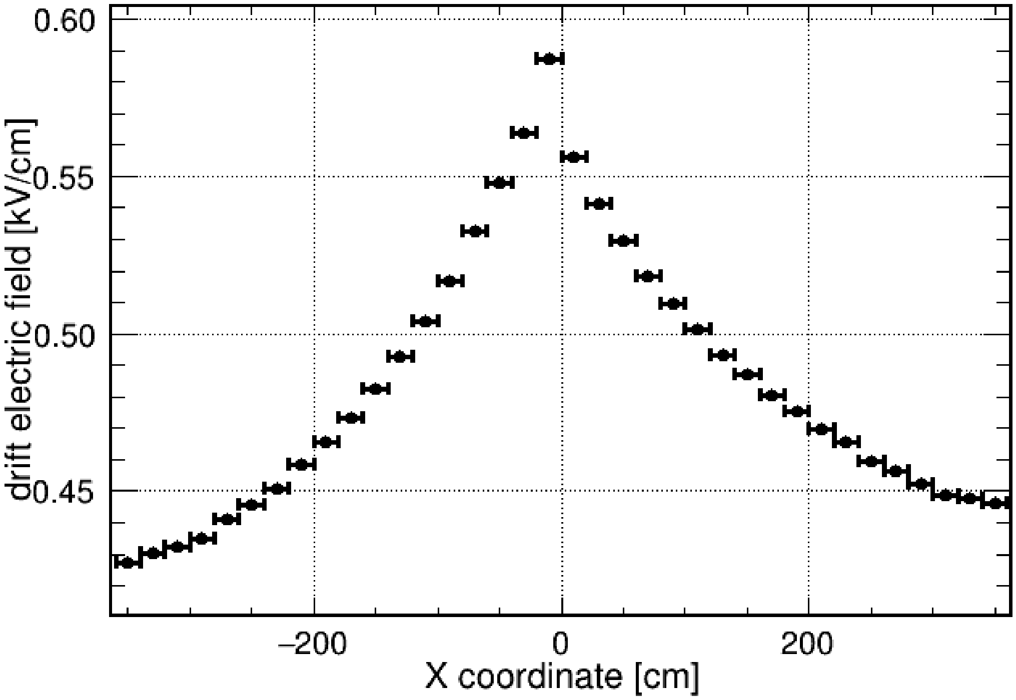

Figure 4.16: Figure shows the electric field as a function of x coordinate for ProtoDUNE-SP beam runs.

charge deposited. It is very important to estimate the correct drift velocity and electric field for reliable position and energy reconstruction of a particle passing through the medium. I developed a technique to measure the drift velocity and electric field using anode-cathode-anode tracks. The effect of SCE is found to be different in the two drift volumes. On the $x > 0$ region, the electric field at the cathode is 15% higher and at the anode, it is 8.5% lower than the nominal value. For $x < 0$ region, the electric field at the cathode is 20% higher and at the anode, it is 11.5% lower than the nominal value. As SCE is the major source of uncertainty in position and energy reconstruction in ProtoDUNE-SP, the SCE maps developed here have been used or are planned to be used for estimating systematic uncertainties in the different analyses including electron life time measurement, hadron-argon cross-section analysis. DUNE is being built 1.5 km underground and will have negligible SCE compared to ProtoDUNE-SP. However, the method developed here for estimating the effect of SCE can be used to validate the measurement of the applied electric field or to detect any local variation in the electric field in DUNE even with a few tracks.

Chapter 5

π^+-argon total reaction cross section measurement

As discussed in section 1.5, pions are the final state products of most neutrino interactions relevant to the DUNE longbaseline experiment. Understanding pion interaction with argon is very important for the simulation and validation of various neutrino interaction models. I am using a cross section reweighting method to estimate the cross section. In this chapter, I will discuss the measurement of π^+-argon reaction cross section in the ProtoDUNE-SP experiment.

5.1 ProtoDUNE-SP beam events:

We collected beam data in ProtoDUNE-SP between Sept 2018 to Nov 2018 the details of which are discussed in section 2.1.7. Table 5.1 shows the number of beam triggers expected and recorded for ProtoDUNE-SP beam runs for different particle species (p, e^+, K, π^+) and momentum distribution, μ^+ is a major background in the pion beam. Using the information from the beamline instrumentation, beam momentum and particle type can be identified (section 2.1.7). In the current cross section analysis, I am using 1 GeV/c momentum π^+ beam, with the aim of taking forward the technique for higher energy π^+ beam in the future.

Momentum (GeV/c)	Total Triggers Recorded ($\times 10^3$)	Total Triggers Expected ($\times 10^3$)	Expected π^+ triggers ($\times 10^3$)	Expected p triggers ($\times 10^3$)	Expected e^+ triggers ($\times 10^3$)	Expected K triggers ($\times 10^3$)
0.3	269	242	0	0	242	0
0.5	340	299	1.5	1.5	296	0
1	1089	1064	382	420	262	0
2	728	639	333	128	173	5
3	568	519	284	107	113	15
6	702	689	394	70	197	28
7	477	472	299	51	98	24
All momenta	4173	3924	1693.5	777.5	1381	72

Table 5.1: Expected and recorded beam triggers for various beam particles in ProtoDUNE-SP. The table is taken from[95].

5.2 Selecting 1 GeV/c momentum π^+ events

For selecting a pure sample of the incident beam pions a combined information of the beamline instrumentation and the TPC reconstruction is used, which will be described in detail in the current section.

5.2.1 Beam event reconstruction:

Pandora software package[58] is used to reconstruct beam and cosmic events in ProtoDUNE-SP. Initially, all the clusters of hits are reconstructed under the cosmic ray hypothesis. In the next step, cosmic-ray events are identified and removed. A track is classified as a clear cosmic-ray candidate if it enters the TPC from the top and leaves from the bottom, the t_0

is inconsistent with a particle coming from the beam and any hit reconstructed assuming t_0=0 appears to be outside the TPC[26]. Once the hits from a clear cosmic ray candidate are removed, a 3D slicing algorithm is used that divides the detector into spatial regions containing all of the hits from a single parent particle interaction. These slices could contain the hits from beam particles as well as cosmic rays which have not been removed in earlier filtering. The slices are reconstructed in parallel with the cosmic-ray and test-beam specific reconstruction.

The test-beam reconstruction is more complicated and can reconstruct the hierarchy of particles seen in the hadronic interaction producing multiple track-like and shower-like trajectories, in addition to searching for the primary vertex of the test beam particle. Once the slices are reconstructed using both the cosmic-ray and test-beam hypothesis a boosted decision tree (BDT) is used to determine the slice with the test-beam origin. The BDT primarily uses topological information to determine the consistency of the slice with the test-beam particle hypothesis. Figure 5.1 shows a fully reconstructed particle hierarchy for simulated beam interaction, with an incoming π^+ beam.

5.2.2 1 GeV/c π^+ beam event selection:

The beamline instrumentation provides the time of flight (TOF) and Cerenkov counter information. As tabulated in table 2.2 the TOF value for π^+/μ^+ should be between 0 to 110 ns and there should be no signal in the low-pressure Cerenkov counter (XCET-L). However, it is not possible to distinguish between π^+ and μ^+ based on the TOF or Cerenkov counter information as their masses are similar, π^+ has a mass of 139.6 MeV/c^2 and μ^+ has a mass of 105.6 MeV/c^2. Using the information from the TPC we can remove the muons from a pion sample which will be discussed in detail later in the chapter.

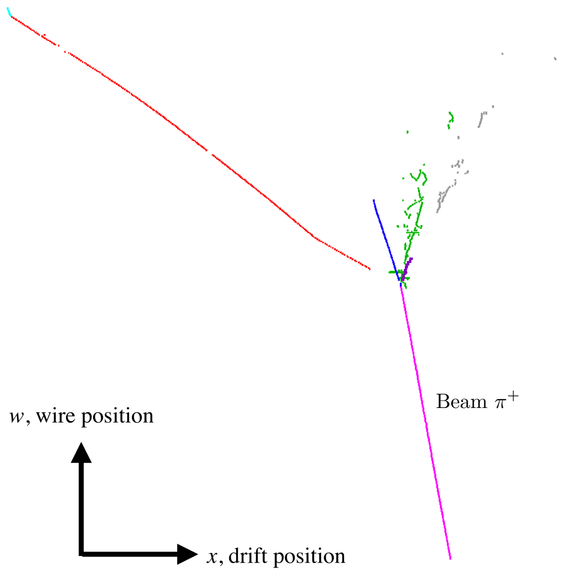

Figure 5.1: The figure shows a reconstructed test beam particle interaction in Monte-Carlo simulated sample. The track in magenta represents incoming beam π^+ track and differnt colors represents different secondary particles created at the interaction vertex. The figure is taken from[26].

5.2.3 Beam quality cuts:

The events with unstable high voltage (HV) or one or more inactive TPC readout boards (FEMBs) are removed. The trajectory of a beam particle before entering the TPC can be reconstructed using the spatial position of a particle as it passes through different profile monitors in the beamline instrumentation. Using the trajectory of the particle before entering the TPC, the 3D position and angle of a particle at the TPC front face are determined. Using the reconstructed particle trajectory inside the TPC the 3D position of the first hit inside the TPC and the angle of beam particle inside the TPC are determined. To remove tracks that are incorrectly identified as a beam particle certain quality cuts are applied. These cuts help remove the background such as cosmic rays and secondary particles produced by beam particles interacting before entering the TPC. The beam quality cuts used are[26]:

- Angle cut: The cosine of the angle between the beamline reconstructed track and the TPC reconstructed track must be greater than 0.93.

- Position cut:
  $0\ cm\ \leq\ (TPC\ start\ X\ -\ beamline\ end\ X)\ \leq\ 10\ cm,$
  $-5\ cm\ \leq\ (TPC\ start\ Y\ -\ beamline\ end\ Y)\ \leq\ 10\ cm,$
  $30\ cm\ \leq\ (TPC\ start\ Z\ -\ beamline\ end\ Z)\ \leq\ 35\ cm$

The space charge effect (SCE) distorts the TPC reconstructed tracks which cause the TPC start position to shift away from the beamline reconstructed track end position. The cuts above are based on the start position of the TPC reconstructed trajectory before SCE corrections. Similarly, for the Monte-Carlo (MC) sample the following beam quality cuts are used.

- Angle cut: The cosine of the angle between the beamline reconstructed track and the TPC reconstructed track must be greater than 0.93.

- Position cut:
  $-3\ cm\ \leq\ (TPC\ start\ X\ -\ beamline\ end\ X)\ \leq\ 7\ cm,$
  $-8\ cm\ \leq\ (TPC\ start\ Y\ -\ beamline\ end\ Y)\ \leq\ 7\ cm,$
  $27.5\ cm\ \leq\ (TPC\ start\ Z\ -\ beamline\ end\ Z)\ \leq\ 32.5\ cm$

5.2.4 Purity of selected sample:

The beamline instrumentation is unable to distinguish between π^+ and μ^+ based on the time of flight information. The major background to our sample of π^+ is the μ^+ which originates from π^+ decay in the beamline. As a pion enters the TPC it undergoes hadronic interactions with the argon nucleus producing different daughter products including secondary pions and protons. Pandora reconstruction algorithm reconstructs the beam particle as a primary particle inside the TPC and daughter products are referred to as secondary particles. Occasionally due to imperfect reconstruction, the hits from the secondary particles are including in the primary beam pion which causes misidentification of the interaction vertex, such events are classified as background events. MC samples are used to determine the purity of the sample. For the MC sample, using the reconstructed track information we can trace back to the true identity of the track using BackTracker Service[96] in LArSoft. If a primary track's true particle identification is π^+ and it is the same track as the beam particle (which can be determined by comparing the true track ID of the primary track and the beam track), this is regarded as a true beam π^+ or beam matched π^+. The table shows the fraction of signal and background in the pion triggered sample. As we cannot separate π^+ and μ^+ using the information from the beamline, the incident beam will consist of both particles. Table 5.2 summarizes the fraction of signal and background for the 1 GeV/c momentum MC simulation. In addition to π^+ and μ^+ the ProtoDUNE-SP 1 GeV/c MC sample also contains other beam particles such as p and e^+. However, we can identify and remove them using beamline instrumentation. In the MC study, using the true particle ID of the beam particles only π^+ and μ^+ are selected for further study.

	number of events	fraction of events
Incident beam π^+ and beam μ^+	46613	1.0
Beam matched primary π^+ (signal)	30901	0.6629
Daughter π^+ (background)	1781	0.0382
Daughter p (background)	3010	0.0646
Daughter μ^+ (background)	10282	0.2206
Other secondary background (d, e^+, μ^-, π^- etc.,)	639	0.0137

Table 5.2: Table shows the total number of π^+ triggered events (which are inseparable from beam μ^+ using the beamline information) and the fraction of signal and background amongst the reconstructed tracks.

The purity of the sample is defined as,

$$\text{purity} = \frac{\text{Number of beam matched primary } \pi^+ \text{ in the sample}}{\text{Total number of beam events } (\pi^+ + \mu^+) \text{ in the sample}} \tag{5.1}$$

The purity of the π^+ triggered sample is 66.29% before background removal.

Removing background:

- Hadronic interaction of π^+ with argon often produces protons as a daughter product. If the reconstruction algorithm fails to identify the interaction vertex and includes proton hits as a part of the π^+ track, the event is regarded as a proton background event. For the 1 GeV/c momentum beam sample, the protons and the pions are separable based on their dE/dx values. Figure 5.2 shows the median dE/dx values for different particles in the 1 GeV/c π^+ triggered sample. MC entries are normalized to match data entries. The distribution is made for tracks with end Z coordinate less than 220 cm. Other background includes e^+, π^-, secondary π^+. The tracks with median dE/dx values higher than 3 MeV/cm are removed as background. The cut is primarily used to remove the proton background, however, it also eliminates the bulk of muons stopping before reaching Z=220 cm.

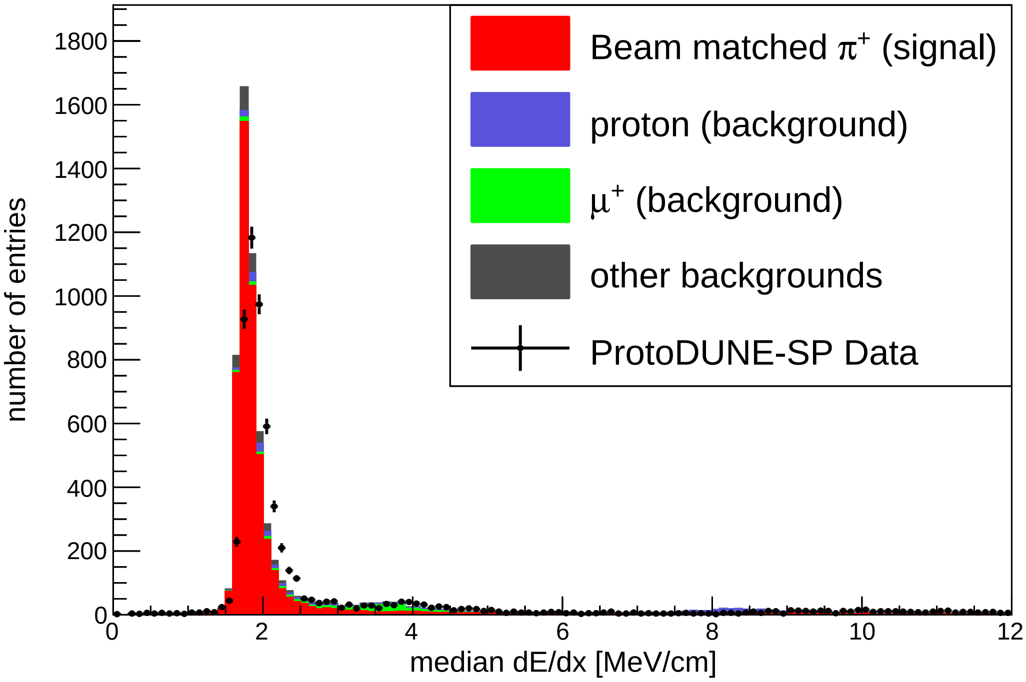

Figure 5.2: dE/dx distribution for 1 GeV/c π^+ triggered sample. Majority of the beam matched π^+ have median $dE/dx < 3\ MeV$ signal, the tracks with median $dE/dx > 3\ MeV$ are removed as background.

- The major source of μ^+ background is the π^+ decay in the beamline or inside the TPC. μ^+ do not exhibit hadronic interaction. However, they decay (≈100%) with the decay mode, $\mu^+ \rightarrow e^+ + \nu_e + \bar{\nu_\mu}$. The e^+ produced in the μ^+ decay is referred to as Michel electron. Michel electron can be identified using topological information. In ProtoDUNE-SP, using Convolutional Neural Network a technique is developed by Aidan Reynolds[97] which gives a Michel score to each hit, if the Michel score is closer to 1 then the hit is likely to be coming from Michel electron. I follow the following steps to identify if a particle decayed into Michel electron:

- Select candidate π^+ track (primary track) using beamline information and quality cuts (using truth information for MC sample).
- Find the Michel score of the hits around the end of the track and not belonging to the primary track. Figure 5.3 shows the total Michel score divided by the number of hits. From the figure, we can see for primary π^+ the average Michel score of hits around the end of the track is close to 0.
- Remove any track with Michels score per hit greater than 0.2.

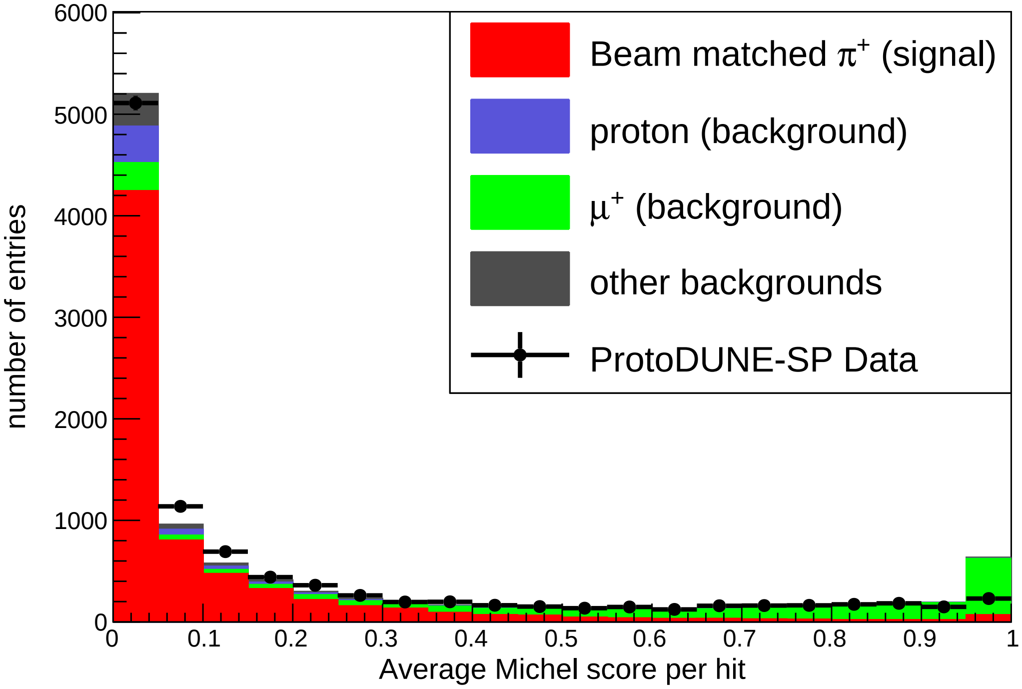

Figure 5.3: Average Michel score per hit for hits around the end of a particle trajectory. Entries with $Michel\ score > 0.2$ are removed as μ^+ background.

- Additionally, tracks with end Z position greater than 220 cm are removed. This is to remove tracks which pass through multiple APAs, there is an APA boundary at Z=230 cm. Between APAs there is a gap of 2 cm. An electron diverter was placed to move the charge away from the gap as a result many tracks were found to be broken in that region. Figure 5.4 shows the end Z position of beam tracks. Between 220 cm and 240 cm in Z there is a strange feature in data distribution, which is a result of tracks broken as they pass through the APA boundary.

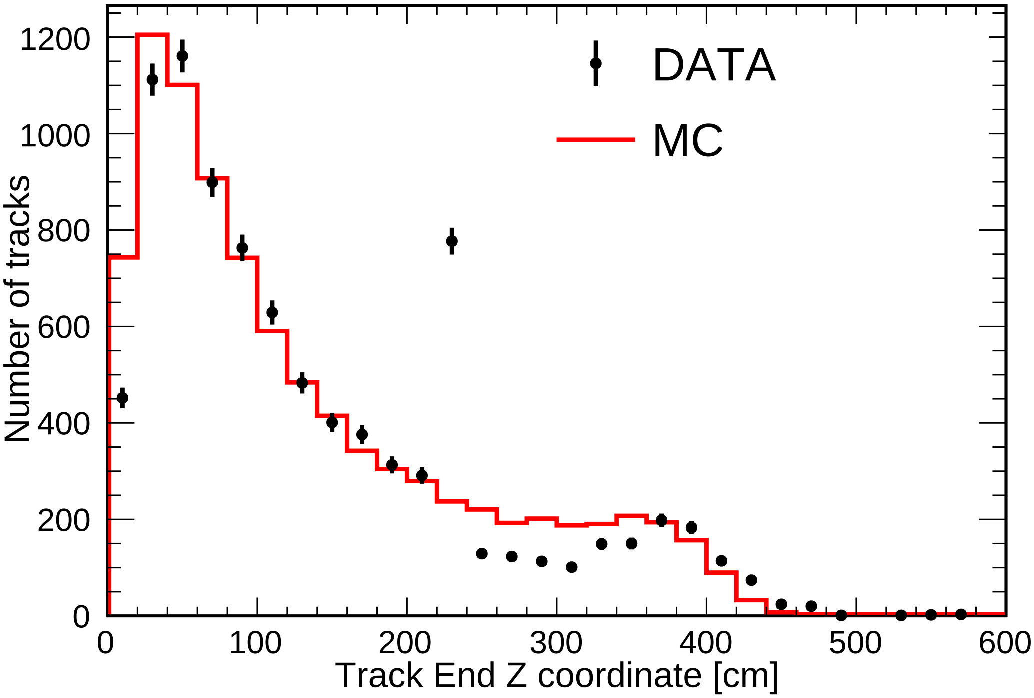

Figure 5.4: Beam track end Z position for data and MC. For data, a number of tracks end in the Z=220 cm to 240 cm bin, which is due to the presence of diverter at around Z=230 cm. The electron diverter is placed to move ionization electrons away from the APA gap, which results in the distortion of the reconstructed trajectory causing reconstruction algorithm to have lower stitching efficiency as tracks pass across the APA boundary. MC entries is normalized to data entries.

Purity and efficiency after removing background cut: Table 5.3 shows the fraction of signal and background events after the above cuts:

	number of events	fraction of selected events
Number of beam particles passing background removal cuts	24247	1.0
Beam matched primary π^+ (signal)	21935	0.8958
Daughter π^+ (background)	1080	0.0441
Daughter p (background)	813	0.0332
Daughter μ^+ (background)	291	0.0119
Other secondary background (d, e^+, μ^-, π^- etc.,)	366	0.0149

Table 5.3: Table shows the fraction of signal (beam matched π^+ and background events remaining after apply background removal cuts (MC).

The purity of the sample is defined as,

$$\text{purity} = \frac{\text{Number of beam matched primary } \pi^+ \text{ in the sample}}{\text{Total number of beam selected events in the sample}} \tag{5.2}$$

The purity of the π^+ sample is 89.58%.

The efficiency of selection is defined as:

$$\text{efficiency} = \frac{\text{Total number of beam selected events in the sample}}{\text{Total number of beam events } (\pi^+ + \mu^+) \text{ present before background removal}} \tag{5.3}$$

The efficiency of selection $= \frac{24247}{46613} = 52.02\%$

5.3 π^+-argon cross section measurement using reweighting tools:

When a particle travels through a medium it may either interact with the medium or pass through the medium without interaction. Cross section is a measure of the likelihood of the interaction of two particles under given conditions[98]. The conditions could be incident particle flux, target material, energy of the incident beam etc. Figure 5.5 shows a number of particle (N_{inc}) incident on a thin target of thickness L, density ρ and atomic mass A. N_{int} is the number of particle interacting with the target material and N_{inc}-N_{int} is the number of particle passing through the target without interacting. The cross section is defined by,

$$\begin{aligned} \sigma &= \frac{N_{int}}{N_{inc}} \cdot \frac{1}{n} \\ &= \frac{N_{int}}{N_{inc}} \cdot \frac{A}{N_A \rho L} \end{aligned} \tag{5.4}$$

where n is the number of particle per unit surface area and N_A is the Avogadro's number. ProtoDUNE-SP is ≈6.95 m along the beam direction. However, it can be divided into thin slices and each slice can be treated as a thin target. As the particle passes through the

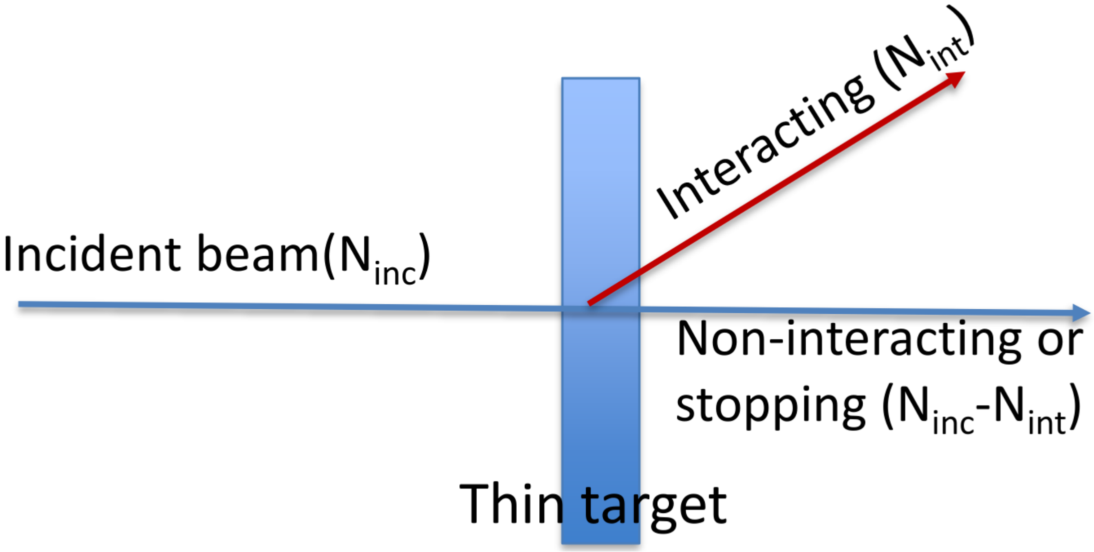

Figure 5.5: Cross section measurement using a thin target.

medium the kinetic energy of the particle at each slice can be measured and the cross section can then be estimated as a function of kinetic energy. The thin-slice method was developed for a LArTPC in the LArIAT experiment[24]. One of the limitations of the thin-slice technique is the requirement of excellent vertex and energy reconstruction. In ProtoDUNE-SP we developed an alternative method for cross section measurement which is less dependent on interaction vertex reconstruction capability, the Geant4 reweighting technique, which I will discuss in detail in the subsequent sections.

5.3.1 Geant4 cross section reweighting technique:

As discussed in section 1.6.2 Geant4 predicts pion-argon cross section based on experimental results of pion cross section on heavier and lighter nuclei. Figure 5.6 shows the π^+-argon Geant4 cross section prediction. The MC simulation uses the cross section prediction by Geant4 to simulate interaction of particles in liquid argon. As a particle interact there could be simply change in direction or new particles could be formed depending on the type of interaction. In hadron elastic interaction no new particle is produce, however the particle changes direction after interaction. However, in the interactions classified as a reaction interaction such as pion absorbtion, charge exchange etc., daughter particles are produced and the primary track ends at the interaction vertex. The particle trajectory is thus dependent on the cross section values or likelihood of interaction. The observables such as track length, d_{XYZ}, deflection parameter (b) which are defined later in the section, are impacted by cross section. In Geant4 reweighting technique we tune the Geant4 predicted cross section in MC simulation such that we get the best agreement between data and MC observables. Some of the observables that can be used for Geant4 cross section reweighting are described below:

- **Track length:** This represents the sum of the distance between consecutive hits on a track, figure 5.7a.
- **d_{XYZ}:** This represents the 3D distance between the start and end of the track, figure 5.7b.

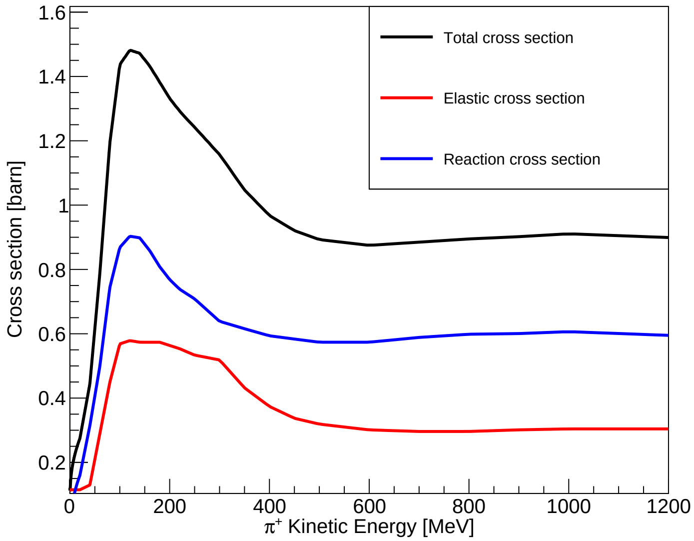

Figure 5.6: Geant4 v10.5 π^+-argon cross section prediction 0-1200 MeV kinetic energy.

- **Deflection parameter (b):** The perpendicular distance between the reconstructed track endpoint and the straight-line projection of the same track considering the first few hits on the track (BC), figure 5.7c.

Figure 5.7 shows the comparison of observables namely track length, d_{XYZ} and deflection parameter for data and MC sample. In Geant4 cross section reweighting we tune the cross section for best data-MC agreement. The method requires producing multiple MC samples with varied cross section values. It will be time and resource-consuming to produce new MC samples for each cross section variation. Considering which a Geant4 reweighting framework (Geant4Reweight[99]) was developed by J. Calcutt for ProtoDUNE-SP which enables us to use the same MC sample for different cross section values. The next section discusses the Geant4Reweight framework in detail.

5.3.2 Geant4Reweight framework:

Geant4Reweight framework is written in C++. It allows users to give weight to tracks produced by Geant4 simulation according to hadron interaction cross section variation. The discussion in this section is completely based on work done by J. Calcutt[99], and the equa-

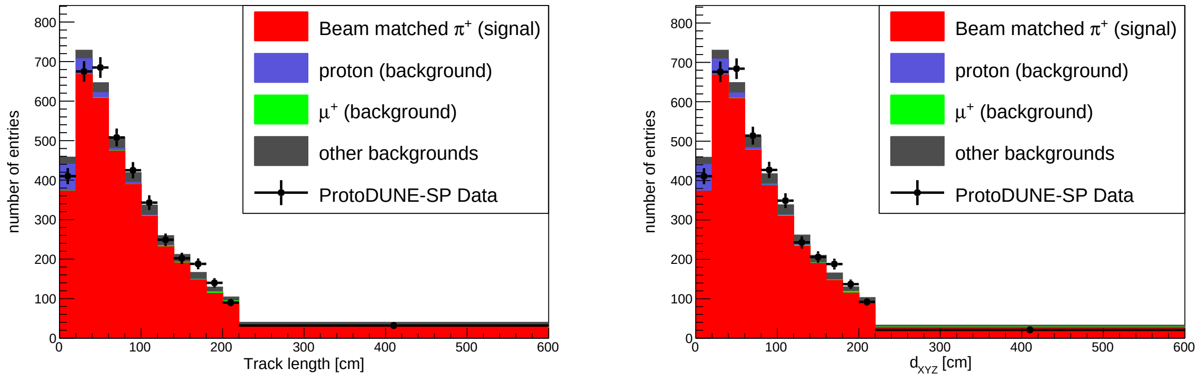

(a) Track length

(b) d_{XYZ}

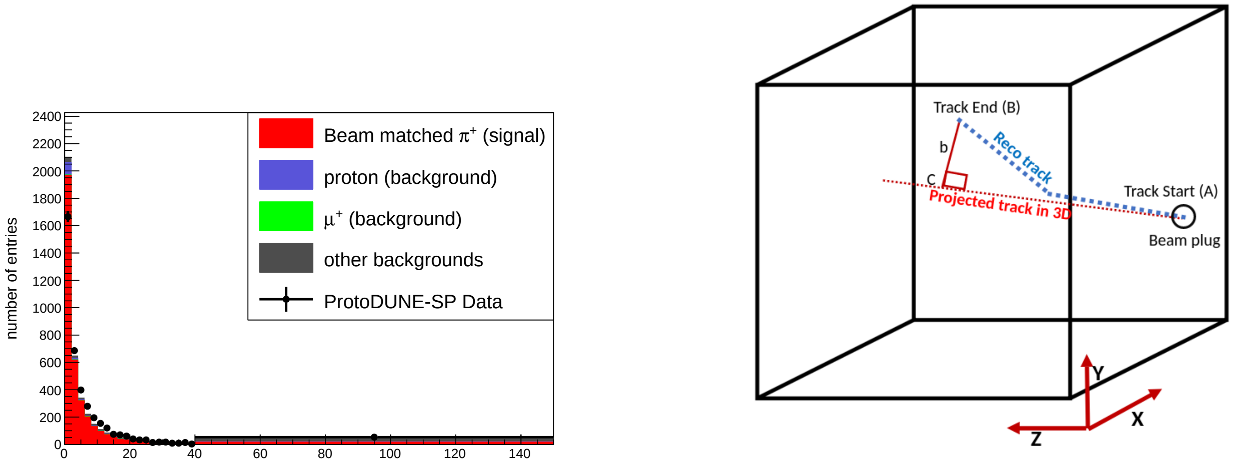

(c) Deflection parameter (b)

(d) Drawing defining data/MC observables

Figure 5.7: Data MC comparison for (5.7a)Track length, (5.7b)d_{XYZ}, (5.7c)Deflection parameter (b), MC entries are normalized to match data entries, the final bin is made wider to increase the bin statistics, (5.7d)Drawing defining observables which are dependent on cross section. The dotted blue points represents hits on a track. Sum of the distance between consecutive hits is defined as the track length. The distance between start and endpoint of the track is defined as d_{XYZ} which is equal to AB in the drawing. Dotted red line represent the projected track considering first 5 hits on the track, the perpendicular distance from the endpoint on the track to the red line (BC) represent deflection parameter b.

tions are taken from a manuscript being prepared for publication.

Geant4 simulation: In Geant4 the active volume of the TPC is divided into small cubes called voxels. Geant4 tracks particles as they pass through the active volume with each step ending at the voxel boundary and calculates the energy deposited by each particle in each step. At each step, the particle is simply moving between voxels or undergoing an interaction. Technically speaking, there are three sets of processes that can be considered in each step namely at-rest, continuous, and discrete processes, the simulation decides which process to invoke. If a particle stops, amongst all the at-rest processes the process that proposes the shortest interaction time (analogous to interaction length) is invoked. In the event of a particle not being at rest, each of the discrete and continuous processes proposes an interaction length. The shortest interaction length is chosen as the step length. As a particle moves between steps each continuous process is invoked and at the end of the step if a discrete process proposes the shortest interaction length that process is invoked. The interaction lengths for elastic and reaction processes are provided by the input cross section values at each kinetic energy, figure 5.6. For Coulomb scattering as well cross section tables provide the interaction length, while for pion decay lifetime tables provide the interaction length.

Reweighting technique: We are interested in reweighting the hadronic elastic and reaction cross section, these come under discrete processes. Consider a pion traveling through some material. For a given process, the probability for the particle to travel some distance δx without interacting is given by (probability of survival):

$$P_S = e^{-\delta x/\lambda} \tag{5.5}$$

where λ is the mean free path for the process and is inversely proportional to the cross section. The survival probability for that process not to occur after a series of steps is given by.

$$P_S = e^{-\sum\limits_{i}^{steps} \delta x_i/\lambda_i} \tag{5.6}$$

where λ_i is the mean free path for i^{th} step, δx_i is the step length taken for the step. Normally,

$$1/\lambda = \sigma\rho N_A/M$$

where σ is the cross section for the process, M, ρ are the molar mass and density of the medium respectively, N_A is the Avogadro's number. The probability of survival can be written as,

$$P_S = e^{-\sum_{i}^{steps} \sigma_i \delta x_i} \tag{5.7}$$

Where the constant extra factors are absorbed into σ to simplify the equation. The probability of survival can be rewritten as:

$$P_S = \prod_{i}^{steps} e^{-\delta x_i \sigma_i} \tag{5.8}$$

If a particle interacts, the interaction will occur only in the last step. The interaction probability will be similar to 5.8 for all the steps except the last step in which the interaction occurs. Interaction probability is thus given by,

$$P_I = \left(\prod_{i}^{steps-1} e^{-\delta x_i \sigma_i} \right) \left(P_{I,f} \right) \tag{5.9}$$

where $P_{I,f} = \left(1 - P_{S,f} \right)$, is the interaction probability and 'f' represents final step as the interaction can only occur in the final step.

$$P_I = \left(\prod_{i}^{steps-1} e^{-\delta x_i \sigma_i} \right) \left(1 - e^{-\delta x_f \sigma_f} \right) \tag{5.10}$$

The probability of survival and interaction can be extended to multiple process. In equation 5.8 and 5.10 we need to replace the respective process cross section by total cross section:

$$\sigma = \sigma_R + \sigma_E + \sigma_X \tag{5.11}$$

where σ_R and σ_E are the total reaction and elastic cross section respectively. All other processes such as pion decay, Coulomb scattering are included in σ_X. The probability for a specific process p to occur is obtained by multiplying the total cross section by the fraction of total cross section made up by σ_P:

$$P_{I,p} = \left(\prod_{i}^{steps-1} e^{-\delta x_i \sigma_i} \right) \left(1 - e^{-\delta x_f \sigma_f} \right) \left(\frac{\sigma_{p,f}}{\sigma_f} \right) \tag{5.12}$$

Weighting each track: In Geant4Reweight we vary the elastic and reaction cross section and determine whether an event is more or less likely to occur. Suppose, we change elastic cross section by a factor f_E and reaction cross section by a factor f_R, the new cross section values are:

$$\sigma'_E = f_E \cdot \sigma_E \tag{5.13}$$

$$\sigma'_R = f_R \cdot \sigma_R \tag{5.14}$$

A Geant4 particle track travels through multiple steps. The total weight for a track is the product of weights for each step. At each step there are 4 possibilities that can occur namely, no interaction, reaction interaction, elastic interaction, and other interaction. For no interaction the weight is given by the change in survival probability:

$$\begin{aligned} W_{S,i} &= e^{-\delta x_i (\sigma'_{R,i} + \sigma'_{E,i} + \sigma_{X,i})} / e^{-\delta x_i (\sigma_{R,i} + \sigma_{E,i} + \sigma_{X,i})} \\ &= e^{-\delta x_i (\sigma'_{R,i} + \sigma'_{E,i})} / e^{-\delta x_i (\sigma_{R,i} + \sigma_{E,i})} \end{aligned} \tag{5.15}$$

For other 3 possibilities the weight is given by change in interaction probability:

$$\begin{aligned} W_{R/E,i} &= \left(\frac{\sigma'_{R/E,i}}{\sigma'_i} \right) \left(\frac{\sigma_i}{\sigma_{R/E,i}} \right) \left(\frac{1 - e^{-\delta x_i \sigma'_i}}{1 - e^{-\delta x_i \sigma_i}} \right) \\ &= f_{R/E} \left(\frac{\sigma_i}{\sigma'_i} \right) \left(\frac{1 - e^{-\delta x_i \sigma'_i}}{1 - e^{-\delta x_i \sigma_i}} \right) \end{aligned} \tag{5.16}$$

$$\begin{aligned} W_{X,i} &= \left(\frac{\sigma_{X,i}}{\sigma'_i} \right) \left(\frac{\sigma_i}{\sigma_{X,i}} \right) \left(\frac{1 - e^{-\delta x_i \sigma'_i}}{1 - e^{-\delta x_i \sigma_i}} \right) \\ &= \left(\frac{\sigma_i}{\sigma'_i} \right) \left(\frac{1 - e^{-\delta x_i \sigma'_i}}{1 - e^{-\delta x_i \sigma_i}} \right) \end{aligned} \tag{5.17}$$

Here, $\sigma_i = \sigma_{R,i} + \sigma_{E,i} + \sigma_{X,i}$ and $\sigma'_i = \sigma'_{R,i} + \sigma'_{E,i} + \sigma_{X,i}$.

5.3.3 Factors affecting data/MC observables:

In the reweighting method for cross section measurement we vary the elastic and reaction cross section to obtain a weight for a track as described in section 5.3.2. Using the measured weights for each track MC observables described in figure 5.7 are remade for each set of cross section scaling factors and compared to data observables to get the best data-MC agreement. However, besides the cross section there could be other sources of discrepancy between data and MC observables that will be discussed in this section.

Beam momentum: The momentum for beam particles is obtained using a momentum spectrometer as discussed in section 2.1.7. The 3 XBPF detectors (figure 2.11) surrounding the magnet provide the momentum for each beam particle passing through the beamline as illustrated in figure 5.8[100]. The lateral position of a particle at each XBPF detector is represented by χ_1, χ_2 and χ_3. L_1, L_2 and L_3 represent the known distance between the monitors and B represent the measured magnetic field. Equation 5.18 and 5.19[26] are used to measure a particles bending angle θ and momentum p.

$$\cos\theta = \frac{M[\Delta L \tan\theta_0 + \Delta\chi \cos\theta_0] + L_1 \Delta L}{\sqrt{[M^2 + L_1^2][(\Delta L \tan\theta_0 + \Delta\chi \cos\theta_0)^2 + \Delta L^2]}} \tag{5.18}$$

$$p = \frac{299.7924}{\theta} \times \int_0^{L_{\text{mag}}} (Bdl) \tag{5.19}$$

Here, $M \equiv \alpha + \chi_1$, $\alpha = \frac{\chi_3 L_2 - \chi_2 L_3}{L_3 - L_2} \cos\theta_0$, $\Delta L \equiv L_3 - L_2$, and $\Delta\chi \equiv \chi_2 - \chi_3$. θ_0 is the nominal bending angle of the beam and is equal to 120.003 mrad[61]. The performance of the momentum spectrometer was validated using high statistics simulation[61], which included all the material in the beamline, the gas in the Cerenkov detectors at the right pressures per momentum, as well as the expected spatial resolution of the profile monitors. For each particle equation, 5.19 was used to calculate the beam momentum. The momentum resolu-

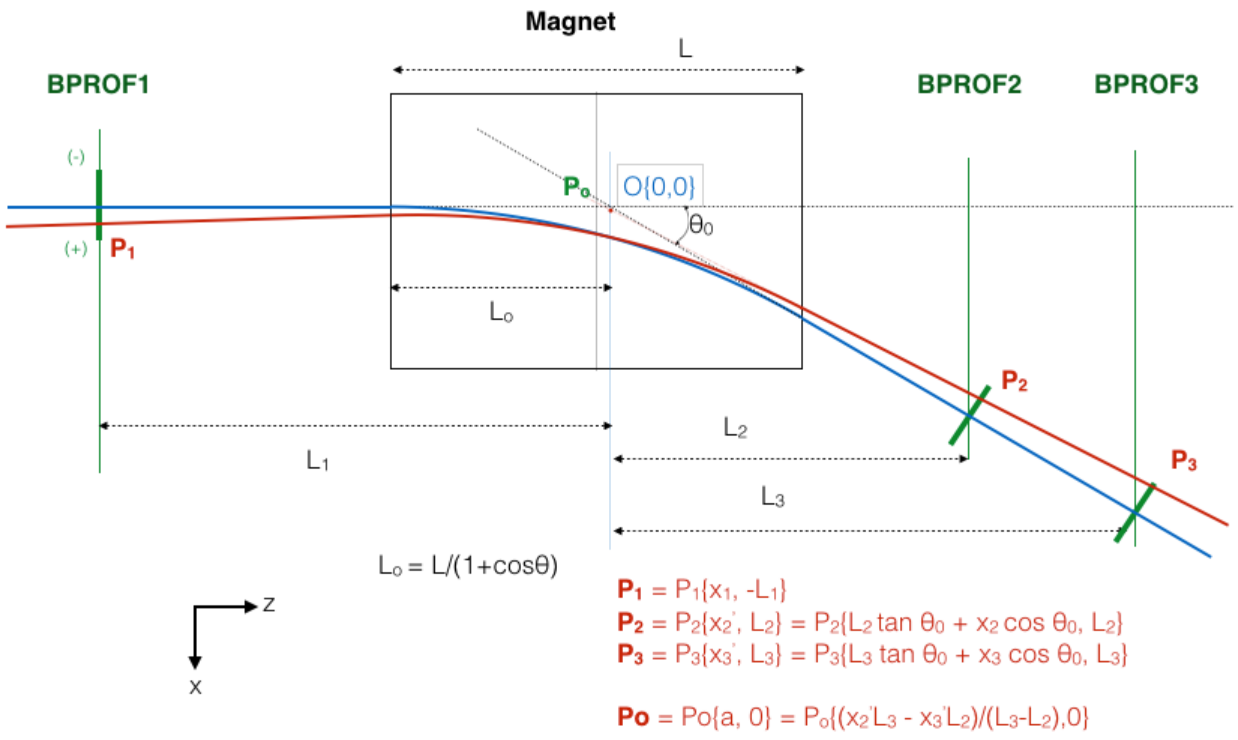

Figure 5.8: A schematic diagram showing the method used for reconstructing momentum and bending angle for a given beam particle (red). Taken from[100].

tion is given by Δp/p. For instance for a beam of the central value of momentum 12 GeV/c and assuming position resolutions of 0.2 mm, 0.5 mm, and 0.8 mm, momentum resolution of 1.1%, 2.5%, and 3.9% respectively assuming no material in the beamline. Including the material in the beamline was found to deteriorate the reconstructed momentum resolution. Figure 5.9 shows the momentum resolution for the beam with a central value of momentum 2 GeV/c and including all the materials in the beamline.

Figure 5.10 shows the momentum resolution as a function of beam momentum for different spatial resolution of beam line monitors. The expected resolution of the fiber profile detectors is 0.3 mm, for which the momentum can be determined to ≈ 2% in the range from 1-12 GeV/c.

As described above the measured momentum have uncertainties related to the spatial res-

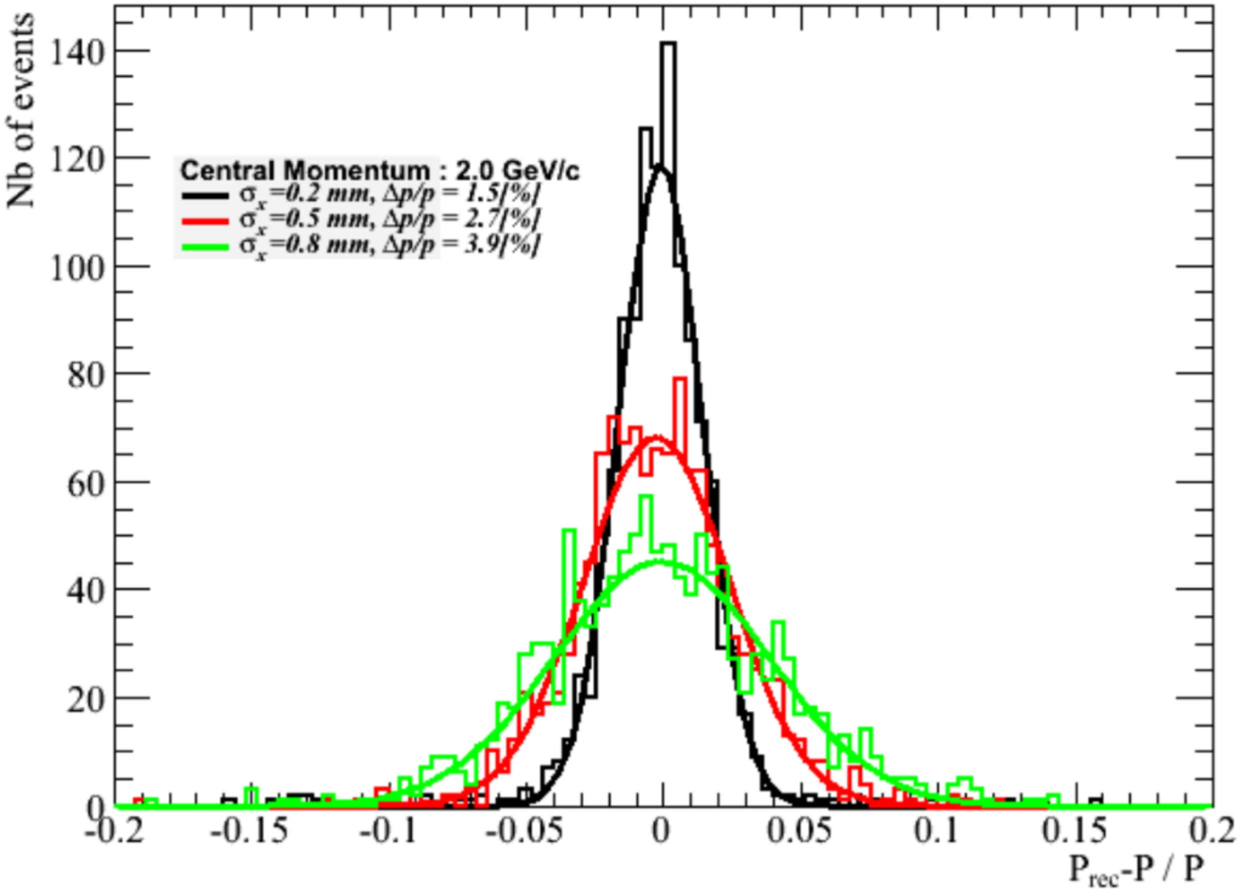

Figure 5.9: Reconstructed momentum for a beam of 2 GeV/c beam, taking into account the material on the beam line. Taken from[100]

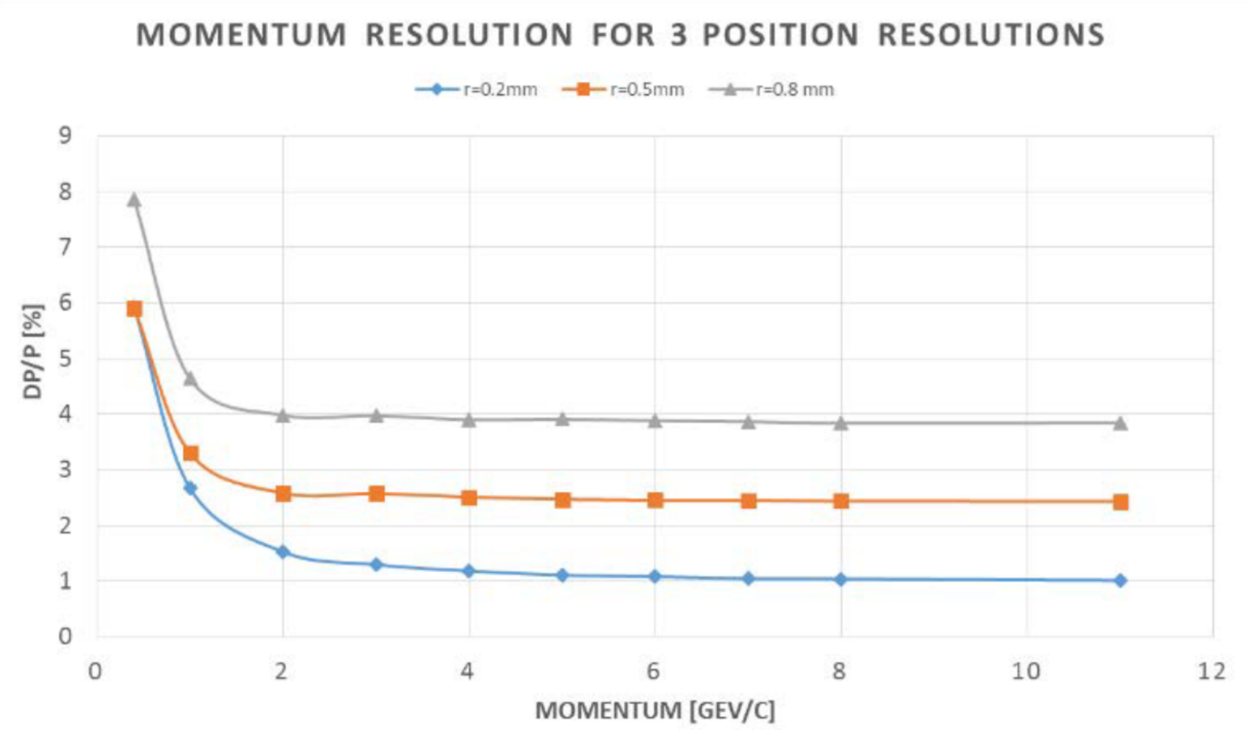

Figure 5.10: Momentum resolution of the spectrometer for three different position resolutions, namely 0.2, 0.5 and 0.8 mm Taken from[100].

olution of the fiber profile detectors, figure 5.11 shows the momentum distribution for ProtoDUNE-SP 1GeV/c data and MC samples. For the ProtoDUNE-SP data central value of momentum is 1.014 GeV/c and the width of the distribution (1 σ) is 0.072 GeV/c. And for the MC sample, the central value of momentum is 1.008 GeV/c and the width of the distribution (1 σ) is 0.0625 GeV/c. Also, the beam particle loses energy as it passes through the material in the beamline and a thin layer of argon between the cryostat and the TPC active volume. There are uncertainties in the energy lost by a particle before entering the TPC active volume which may lead to data and MC momentum not agreeing and thus causing disagreement in the distribution of the observables described in section 5.3.1. For pions, it is difficult to disentangle the effect of cross section, beam momentum, or other factors such as the fraction of background on the distribution of the data-MC observables. Muons do not exhibit hadronic interaction and thus the observables such as track length, d_{XYZ} for muons depend mainly on the beam momentum. Therefore, we are using muons to reweight the MC momentum distribution for best agreement between data and MC observables for muons and use the same momentum reweighting results for pions. The muon momentum reweighting method is described in the next section.

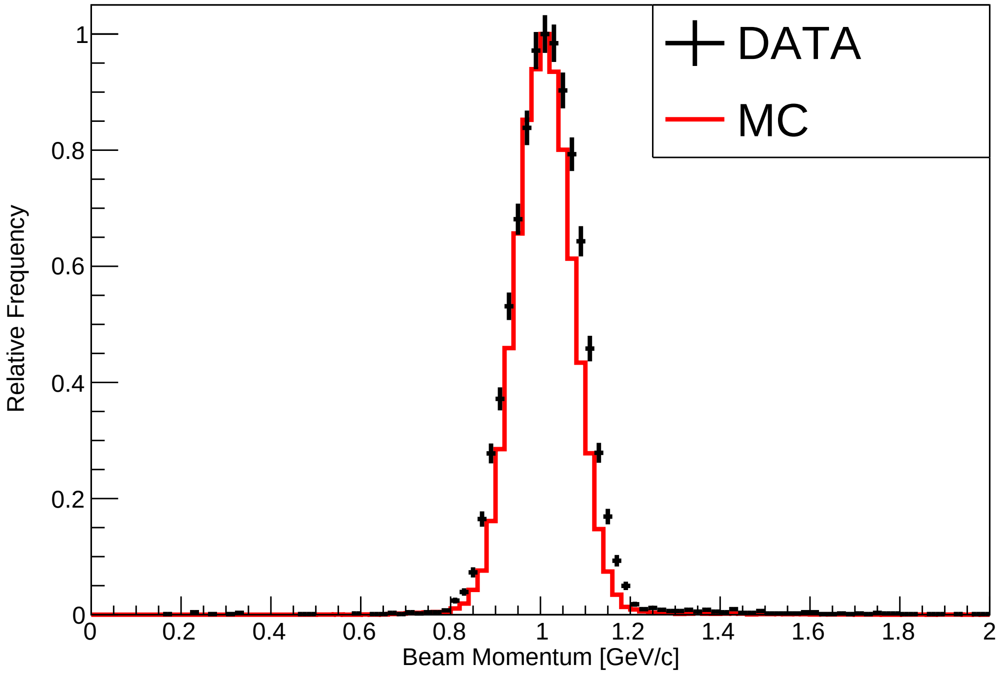

Figure 5.11: Data and MC momentum distribution for 1 GeV/c momentum particles.

Muon fraction in the pion triggered beam: In addition to cross section and beam momentum, another major source of disagreement between data and MC observables is the fraction of muons in the pion triggered beam. Muons are produced in pion decay. From MC study, before background removal the pion triggered sample contains ≈ 22% muon background (table 5.2) after background removal the muon fraction reduces to ≈ 1.2% (table 5.3). However, during background removal tracks with end Z position greater than 220 cm are removed which reduces the muon background as most muons are long tracks, if we do not remove tracks with end Z position greater than 220 cm the remaining muon fraction in the beam after quality cuts are ≈ 7.5%. For normalizing MC distribution to match data entries we need to use all the tracks irrespective of end Z position, so it is important to understand the fraction of the remaining muon background as we cannot completely remove them.

5.3.4 Momentum reweighting using muons:

A sample of μ^+ is used for momentum reweighting. μ^+ is selected based on the Michel score of the hits close to the end of the track. If *average Michel score per hit* > 0.2 and the track end Z position is greater than 240 cm the tracks are selected as muon tracks. Using the MC sample the purity of selection is estimated.

$$\text{purity} = \frac{\text{Number of true muons in the selection}}{\text{Number of toal selected candidate muons}} = \frac{4051}{4688} = 86.4\% \tag{5.20}$$

Described below is the method used for momentum reweighting:

- Each candidate muon track is given a weight based on the momentum.
- For the default 1GeV/c MC momentum distribution the momentum central value is p_0=1008 MeV/c and width is σ_0=62.5 MeV/c. A grid search is carried out to find a momentum central value and width that makes the weighted MC d_{XYZ} distribution for muons best agree with the corresponding distribution for data. The d_{XYZ} distribution is chosen as we need to know only the start and endpoints of a track for d_{XYZ} distribution, unlike track length which requires a knowledge of every point on the track. Often the tracks are distorted at APA boundaries which makes track length less reliable. In addition, the d_{XYZ} parameter is less affected by missing hits caused by bad TPC channels, except when the track stops near one of the bad channels. An array of momentum with central value (p_i) between 850 MeV/c and 1150 MeV/c and width (σ_j) between 30 MeV/c to 130 MeV/c is used in the grid search.
- For a momentum distribution with central value p_i and width σ_j, the Gaussian momentum distribution is given by

$$g_{ij} = e^{\frac{-(p-p_i)^2}{2\sigma_j^2}} \tag{5.21}$$

where p is the momentum variable. Similarly, the Gaussian distribution for MC default momentum distribution is given by,

$$g_0 = e^{\frac{-(p-p_0)^2}{2\sigma_0^2}} \tag{5.22}$$

- The weight for a particle of momentum p is given by,

$$W_{ij}(p) = g_{ij}/g_0 \tag{5.23}$$

- Each element of the momentum array $(p_i,\ \sigma_j)$ produces a weighted MC distribution of d_{XYZ} which is compared to data d_{XYZ} distribution and χ^2 value is estimated. The value corresponding to the least χ^2 is the final momentum value which will be used for pion momentum reweighting.

χ^2 **estimation:** The χ^2 estimation is based on the publication[101]. In this analysis, the sum of the weights is used to estimate the number of incident particles. A compound Poisson distribution (CPD) is used to describe the distribution of the sum x of a Poisson distributed number of weights, given the weights are independent and identically distributed random variables[101]. Consider an experimental histogram with m_j entries in j^{th} bin and the theoretically predicated entries be $x_j(\theta)$ depending on one or several parameters θ. The theoretical prediction is obtained from MC simulation which reproduces the experimental conditions and the smearing by resolution effects. The complete simulation cannot be produced for each selected parameter. Suppose the simulated data is produced with some parameter θ_0 according to probability distribution function (p·d·f) f(θ_0), for each parameter θ the p.d.f. for θ_0 can be reweighted, removing the necessity to produce a new MC sample for each parameter θ, the weights are given by w=f(θ)/f(θ_0).

Then $x_j = \sum_{i=1}^{n_j} w_{ij}$ where n_j is the generated events in bin j. The χ^2 expression comparing Poisson numbers m_j times the normalization constant c to compound Poisson number x_j for parameter θ is given by,

$$\chi^2 = \sum_{j=1}^{B} \frac{(cm_j - x_j(\theta))^2}{\delta_j^2}, \tag{5.24}$$

$$= \sum_{j=1}^{B} \frac{(cm_j - \sum_{i=1}^{n_j} w_{ij})^2}{\delta_j^2} \tag{5.25}$$

where B is the number of bins, δ_j^2 is the expected value of the numerator under the hypothesis that the two summands in the bracket have the same expected value μ. For scaled Poisson distribution (SPD) approximation based on the publication[101], the log likelihood is given by,

$$\ln\ (L(\mu)) \ = \ m\ \ln(\frac{\mu}{c}) - \frac{\mu}{c} + \tilde{n}\ \ln\tilde{\lambda} - \tilde{\lambda} + const \tag{5.26}$$

where the index j is suppressed. $\tilde{n} = x/s$, $\tilde{\lambda} = \mu/s$, $\mu = \mathrm{cs}\frac{\tilde{n}+m}{c+s}$, and the corresponding $\delta^2 = cs(\tilde{n} + m)$. Equation 5.26 can be written in simplified form as,

$$\ln\ (L(\mu)) = m\ \ln(cm) - \tilde{n}\ \ln(\tilde{n}s) + (m + \tilde{n})\ \ln(\frac{cs(m+\tilde{n})}{c+s}) \tag{5.27}$$

The χ^2 is estimated using,

$$\chi^2 = -2\ \sum_{i=1}^{B} \ln\ (L(\mu)) \tag{5.28}$$

Equation 5.28 is used for χ^2 estimation for all the weighted MC distributions in the subsequent sections.

Momentum reweighting results: In figure 5.12 the color scale shows the χ^2-χ^2_{min} values as a function of momentum central values (p_i) and momentum width (σ_j). For the minimum χ^2 distribution the central value of momentum is obtained to be 1027 MeV/c and the momentum width is 67 MeV/c. These results will be used for the momentum reweighting of candidate π^+ distribution. Figure 5.12 shows the χ^2-χ^2_{min} for each value of momentum. Figure 5.13 shows the comparison of d_{XYZ} distribution of candidate μ^+ for ProtoDUNE-SP data, default MC, and the reweighted MC distribution with minimum χ^2.

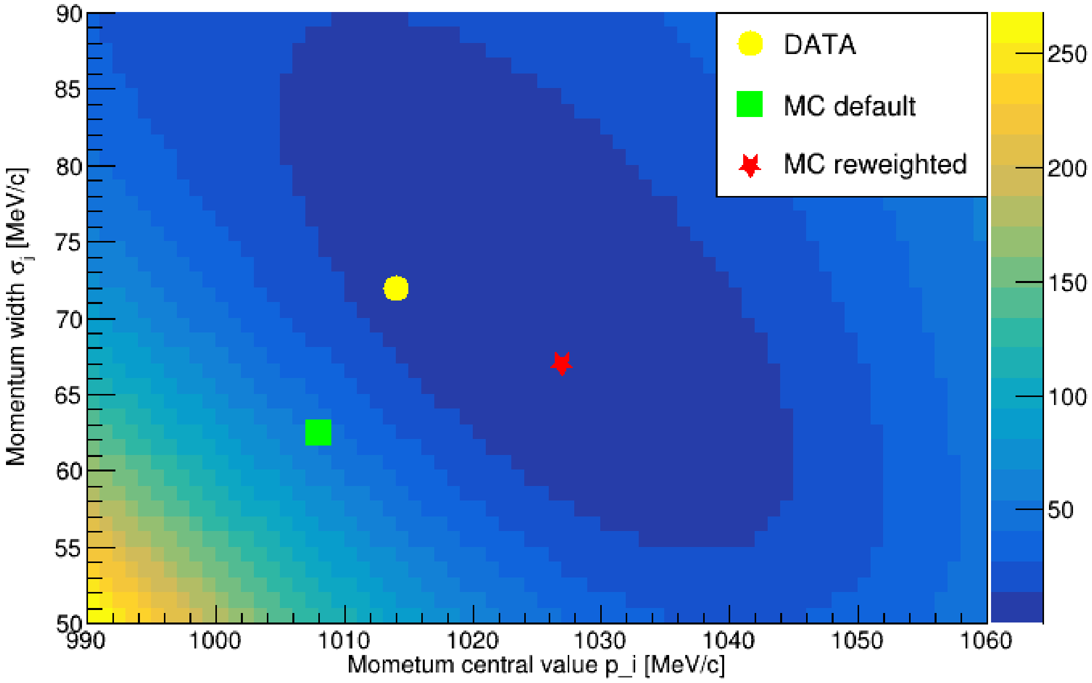

Figure 5.12: The color scale shows the χ^2-χ^2_{min} distribution for candidate muons. The points in the plot shows the value of default MC momentum, data momentum and the results of momentum reweighting. The results obtained using muons will be used for pion momentum reweighting.

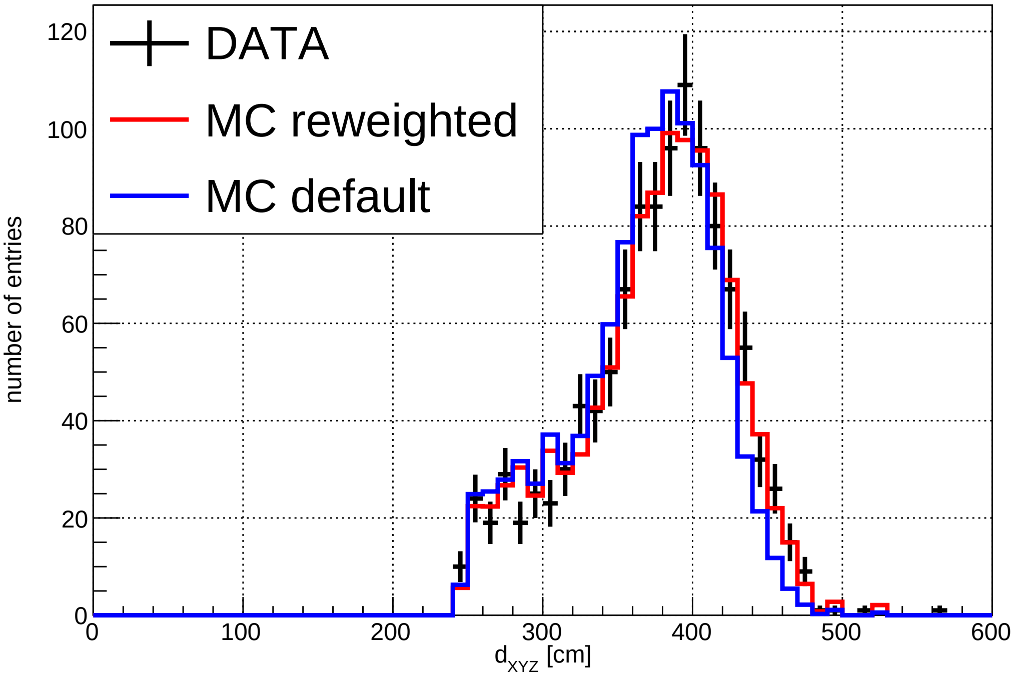

Figure 5.13: Comparison of d_{XYZ} distribution for candidate μ^+ for data, default MC, and minimum χ^2 reweighted MC.

5.3.5 Muon fraction reweighting:

The major background in the π^+ triggered sample is the μ^+ which originates from π^+ decay in the beamline and inside the TPC. Previously, I discussed the techniques used for removing μ^+ using CNN Michel scores. However, we cannot completely remove the μ^+. Using reweighting technique we estimate the fraction by which μ^+ must be changed in MC such that they agree with data. The muon fraction reweighting is described as follows:

- A sample of candidate π^+ is selected and the proton and muon background removal cuts described earlier are applied.

- d_{XYZ} distribution for the sample is plotted with $d_{XYZ} > 220\ cm$ binned in a single bin, which is done as more tracks are breaking at the APA boundary for data compared to MC which results in data-MC discrepancy for the d_{XYZ} distribution.

- For MC sample a weight is given to each μ^+ background (which is identified using truth information) in the sample, which is used to fill the d_{XYZ} histogram. The procedure is repeated for an array of weights, each weight producing a new MC d_{XYZ} distribution.

- The histogram corresponding to minimum χ^2 when compared to data is identified and the corresponding weight gives the muon weight for best data-MC agreement.

Figure 5.14 shows the χ^2-χ^2_{min} values for data-MC comparison of d_{XYZ} for different muon weights. Figure 5.15 shows the results of muon number reweighting. For best data-MC agreement the weights of muon should be 1.06, which means we must increase the fraction of muon in MC by 6% to match the fraction of muon in data. The results show the muon fraction in MC is in good agreement with the muon fraction in data. The results are directly used in cross section reweighting.

5.4 Inclusive π^+ cross section measurement:

Event Selection: A sample of π^+ is selected as described in section 5.2.2 and d_{XYZ} distribution for data is plotted. For MC sample the results of momentum reweighting and μ^+

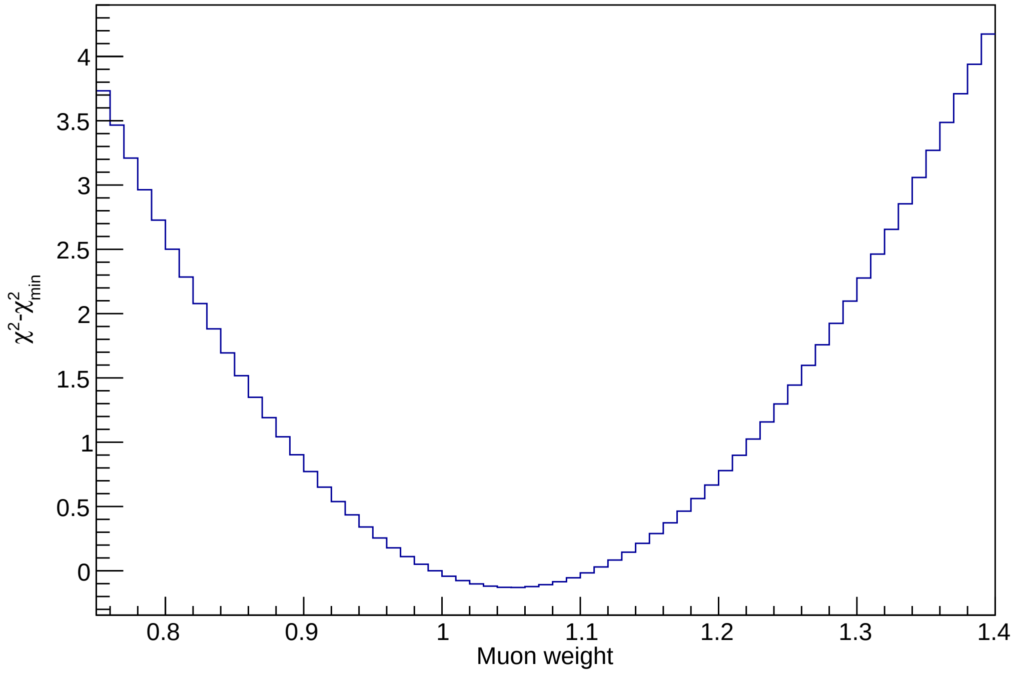

Figure 5.14: χ^2-χ^2_{min} vs weights for true μ^+. Each μ^+ background is identified using MC truth information and a weight is given.

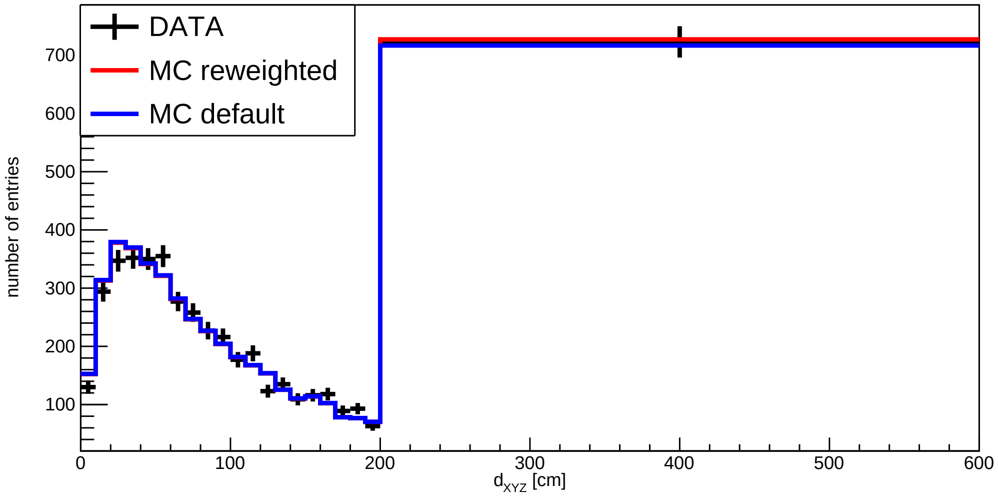

Figure 5.15: Comparison of d_{XYZ} distribution for candidate π^+ for data, default MC, and minimum χ^2 muon number reweighted MC.

fraction reweighting described in previous section are applied. The reaction cross section weight (W_R) is calculated for each incident true π^+ (which is determined using MC truth information), using Geant4Reweight tool as described in section 5.3.2. The reaction cross section is scaled between 0 to 2 times (in increments of 0.01) the default Geant4 cross section keeping the elastic cross section unchanged from Geant4 predictions. For each reaction cross section scaling factor (f_R) we obtain a weight for each track. The following steps describes the total weight given to each track:

- Let us first describe the momentum weights for each track,

  $$W_{mom}(p) = g_1/g_0 \tag{5.29}$$

  where $W_{mom}(p)$ is the momentum weight for a particle with momentum p. $g_1 = e^{\frac{-(p-p_1)^2}{2\sigma_1^2}}$, p_1=1027.0 MeV/c and σ_1=67.0 MeV/c, the momentum central value and width respectively which best agrees with data. $g_0 = e^{\frac{-(p-p_0)^2}{2\sigma_0^2}}$, p_0=1008.0 MeV/c and σ_0=62.5 MeV/c, the momentum central value and width respectively for default MC sample.

- Muon fraction weight is given by W_{muon}=1.06 for each background muon.

The total weight for each particle is given by:

Case 1: If the particle is a beam matched π^+ (signal):

$$Total\ weight\ (W_T) \ = \ W_R \cdot W_{mom} \tag{5.30}$$

Case 2: If the particle is a muon background:

$$Total\ weight\ (W_T) = \ W_{mom} \cdot W_{muon} \tag{5.31}$$

Case 3: If the particle is a non muon background:

$$Total\ weight\ (W_T) = \ W_{mom} \tag{5.32}$$

We determine the W_T for each scaling factor f_R and each track. Using the weights the d_{XYZ} histogram for each scaling factor is made for MC and compared with data. χ^2 for each scaling factor is estimated using equation 5.28, the scaling factor resulting in minimum χ^2 gives the final results for the cross section. Figure 5.16 shows the χ^2-χ^2_{min} values for different scaling factors. For best data-MC agreement we should scale the reaction cross section 0.97 times the Geant4 predicted cross section. Figure 5.18 shows the d_{XYZ} distribution for candidate π^+ for data, default MC and reaction cross section reweighted minimum χ^2 distribution. The default MC distribution and the best-reweighted cross section are in close agreement which indicates the π^+ reaction cross section is well predicted by Geant4.

From figure 5.17 the value of reaction cross section scaling factor corresponding to χ^2=χ^2_{min}+1 are 0.94 and 1.0. The reaction cross scaling factor in the 1-σ interval is 0.97 ± 0.03. As there are enough entries in each bin for d_{XYZ} distribution, a properly scaled compound poisson distribution (CPD) should be nearly gaussian. Hence the statistical uncertainty based on the χ^2 distribution (σ_{Stfit}=0.03) gives a good estimate of the uncertainty in the measured value. In the next section, I will discuss the bootstrap method for determining the statistical uncertainty.

5.4.1 Statistical uncertainty using Bootstrap method

The Bootstrap method[102;103] is a powerful technique that can be used when we don't know enough about the underlying processes or error in measurement to do a reliable Monte Carlo simulation. This method is only valid for independent and identically distributed data sets. Bootstrapping is a test that uses random sampling with replacement. In this method, the actual data set (S_0) with N data points is used to generate any number of data sets. The new data sets (S_1, S_2, S_3.......) will consist of N randomly drawn data points from the original dataset (S_0). Many entries will be repeated in the new data sets. The same analysis to obtain a measured parameter is repeated for the new samples. From the distribution of the measured parameters, the uncertainty of the measurement is estimated.

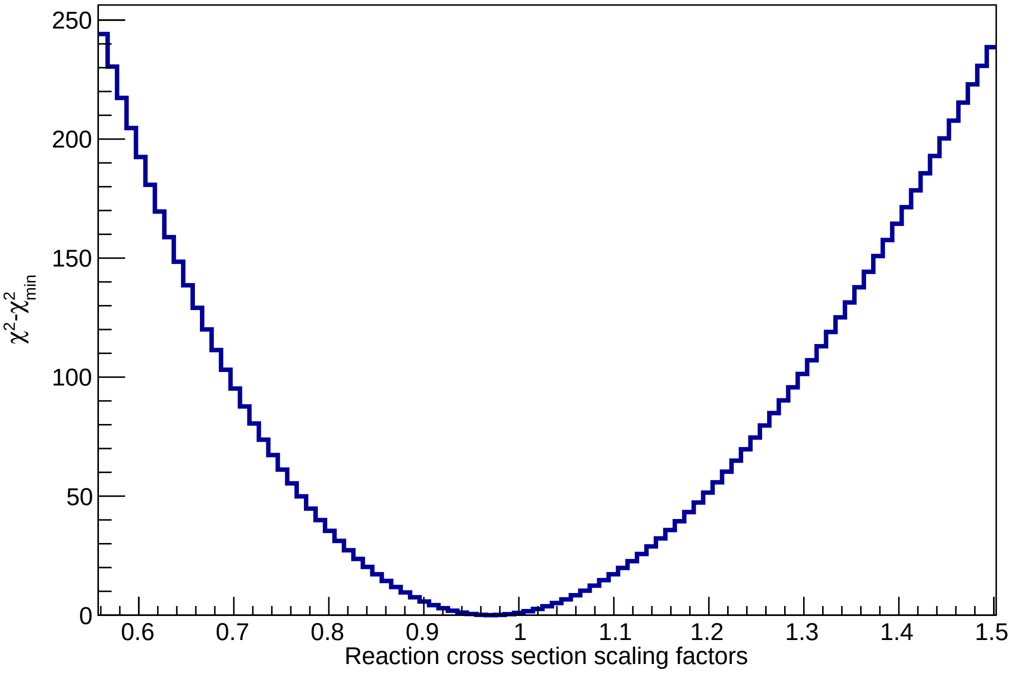

Figure 5.16: χ^2-χ^2_{min} vs reaction cross section scaling factors, the value of scaling factor corresponding to χ^2_{min} is 0.97.

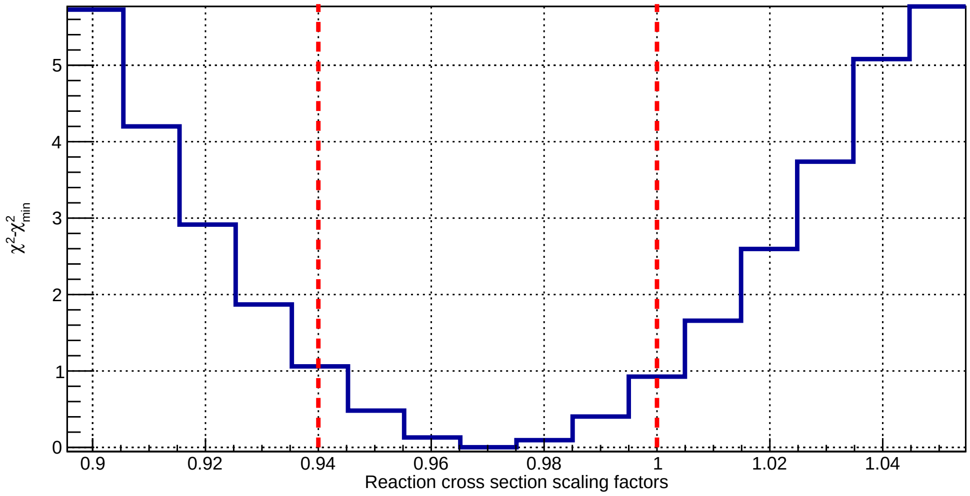

Figure 5.17: Figure 5.16 magnified around χ^2=χ^2_{min} region. The dotted red lines represents 68.3% confidence interval for the value of reaction cross section scaling factor.

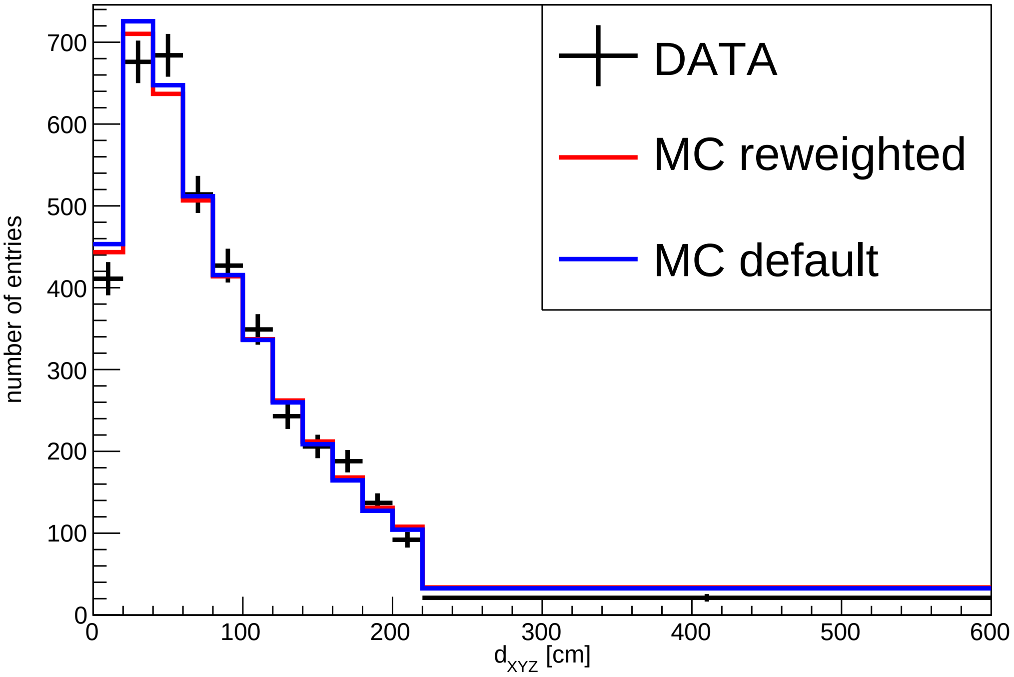

Figure 5.18: Comparison of d_{XYZ} distribution for candidate π^+ for data, default MC, and reaction cross section reweighted minimum χ^2 distribution. The default MC distribution and the reweighted MC distribution with minimum χ^2 are in good agreement.

Statistical uncertainty due to MC (σ_{StMC}): In the reaction cross section estimation, the original MC data set is used to produce the cross section result as described in section 5.4. There were 217163 events used in the original sample. I produced 100 new datasets randomly choosing 217163 events from the original MC dataset. The reaction cross section scaling factor is estimated for each of the 100 new samples. Figure 5.19 shows the reaction cross section scaling factors for 100 new samples generated from the original Monte Carlo sample. The standard deviation (σ_{StMC}) of the distribution is obtained to be 0.011.

Statistical uncertainty due to ProtoDUNE-SP Data (σ_{StData}): Similar to the calculation of σ_{StMC} I divided the ProtoDUNE-SP Data into 100 new samples with the same number of entries as the original dataset, choosing randomly from the original dataset. While estimating σ_{StData} the original MC distribution is used for all the new while changing the Data samples. Figure 5.20 shows the reaction cross section scaling factors for 100 new datasets derived from the original ProtoDUNE-SP Data. The standard deviation (σ_{StData}) is obtained to be 0.020. The number of entries in MC is approximately a factor of 2 higher than the number of entries in Data, which results in higher statistical uncertainty in results due to Data compared to MC.

Total statistical uncertainty using bootstrap method is given by:

$$\sigma^2_{Stbootstrap} = \sqrt{\sigma^2_{StMC} + \sigma^2_{StData}} \tag{5.33}$$

Which gives, $\sigma_{Stbootstrap}$=0.023. The statistical uncertainty using the bootstrap method is slightly lower than the uncertainty using the χ^2 distribution. However, as the statistics for data and MC samples are sufficiently large for CPD to be nearly gaussian I chose the statistical uncertainty estimated using χ^2 distribution as the statistical uncertainty in the reaction cross section scaling factor. In the next section, I will discuss the sources of systematic error and their estimation.

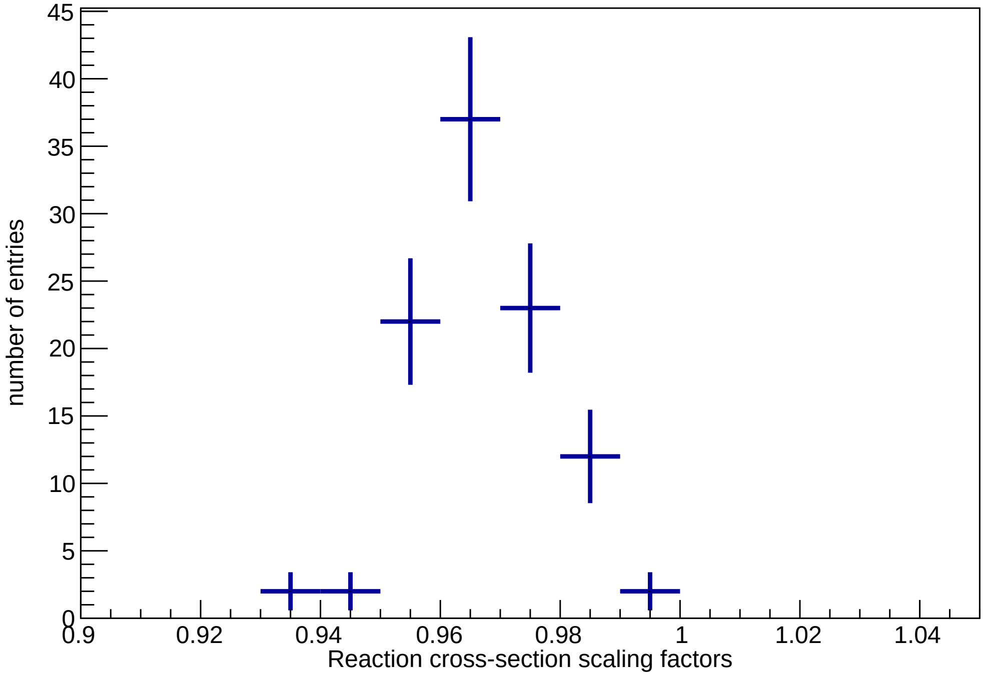

Figure 5.19: Reaction cross section values for different samples derived from the original MC sample. The distribution is used to estimate σ_{StMC}.

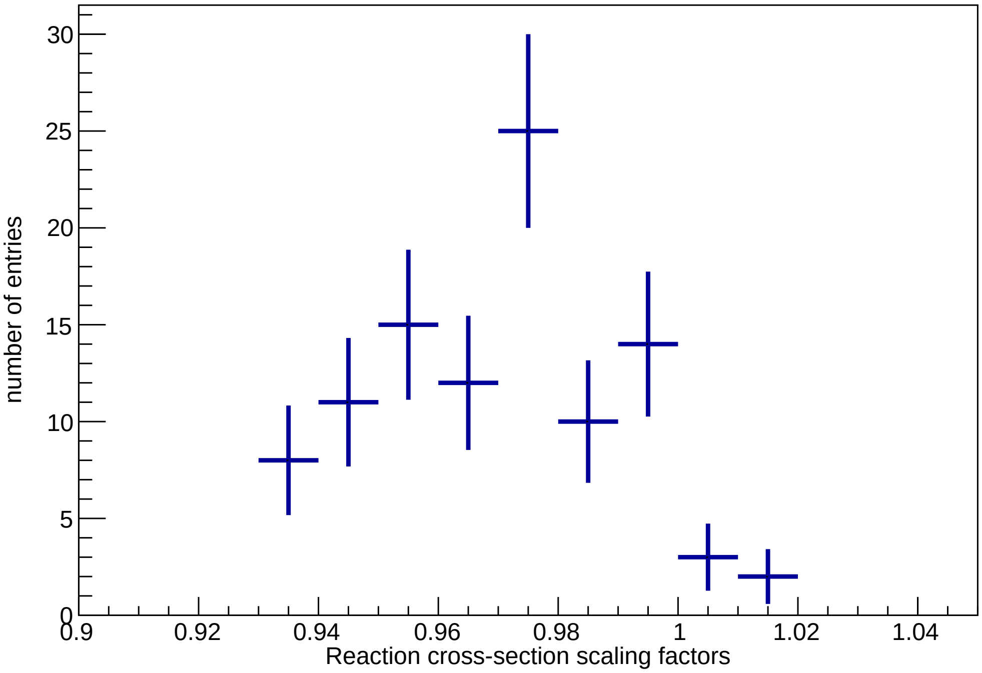

Figure 5.20: Reaction cross section values for different samples derived from the original data sample. The distribution is used to estimate σ_{StData}.

5.5 Systematic uncertainty in reaction cross section measurement:

The major source of systematic uncertainty in measured reaction cross section are uncertainty in μ^+ fraction in MC sample, space charge effect (SCE), and the effect of the elastic cross section on the observables.

5.5.1 μ^+ fraction uncertainty:

The μ^+ fraction in the beam has been estimated in section 5.3.5. From figure 5.14 the fraction of μ^+ for χ^2=χ^2_{min} +1 (68.3% confidence interval) approximately lies in the range 1.06±0.15. Using the muon weight = 1.21 (1.06+0.15) and repeating exactly the same procedure as described earlier for reaction cross section measurement I obtained a reaction cross section scaling factor of 0.98 and using muon weight = 0.91 (1.06-0.15) I obtained a reaction cross section scale factor of 0.96. So increasing or decreasing the muon fraction by 15% changes the reaction cross section scaling factor by ±0.01.

5.5.2 SCE systematic error:

SCE distorts the particle trajectory thus affecting the distribution of observables. An SCE map described in[26] is used to correct the SCE distortion. All the distributions shown so far has the SCE correction applied to particle trajectories based on the SCE map described in[26]. The SCE map was derived by interpolating the measured SCE distortions at the TPC faces to the bulk of the TPC. There are uncertainties in the SCE map due to various factors including uncertainty in positive ion density, the time dependence of SCE, fluctuation in High Voltage during data taking, and many more. I developed an alternative SCE map using anode-cathode-anode crossing tracks which is described in section 4.2.3. The coverage of the anode-cathode-anode tracks is poor near the TPC faces. I extrapolated the measurement of SCE distortion inside the TPC to the TPC faces by linearly extrapolating the SCE map from a region close to the TPC boundary. For the SCE systematic analysis for the cross section, we need to estimate the SCE correction localized to the region of the TPC where a beam particle can pass through. After extrapolation to the TPC upstream and downstream faces, the SCE map using anode-cathode-anode crossing tracks covers a region of $-360\ cm < X < 360\ cm$, $0\ cm < Z < 690\ cm$, and $200\ cm < Y < 500\ cm$.

For data, the track start and endpoints are corrected using an anode-cathode-anode track SCE map, while for MC simulation the input SCE map used for simulating the events is well hence no changes are made. Once we have data d_{XYZ} distribution we compare it with MC for an array of reaction cross section scaling factors as described in previous sections. Figure 5.21 shows the results of the SCE systematic study on the cross section. The reaction cross section scaling factor corresponding to minimum χ^2 is estimated to be f_R=0.97. The cross section results are identical using the two SCE maps. This shows the effect of SCE is well understood. The bin size for d_{XYZ} is 20 cm and the step size for scaling factor is 0.01 which could hide small differences in the results due to two SCE maps estimated independently using different techniques. Considering which the SCE systematic on the results is taken to be 0.01.

5.5.3 systematic due to Elastic cross section:

Similar to reaction cross section, Geant4 predicts the elastic cross section of π^+ on argon based on the results of π^+ elastic cross section cross section on heavier and lighter nuclei. However, there has not been a measurement of π^+ elastic scattering at low scattering angles ($< 5deg$). Figure 5.22 shows the differential elastic cross section of π^+ and π^- on various isotopes of Ca[104]. The results show the elastic cross section increases at a lower scattering angle. Also, the cross section at an angle lower than a certain threshold is not measured experimentally. In the lack of experimental measurement, the prediction of Geant4 elastic cross section at a low scattering angle may not be completely reliable. If we want to measure the elastic cross section using the Geant4 reweighting technique, we will have to use different scaling factors for different scattering angles which makes the analysis computationally

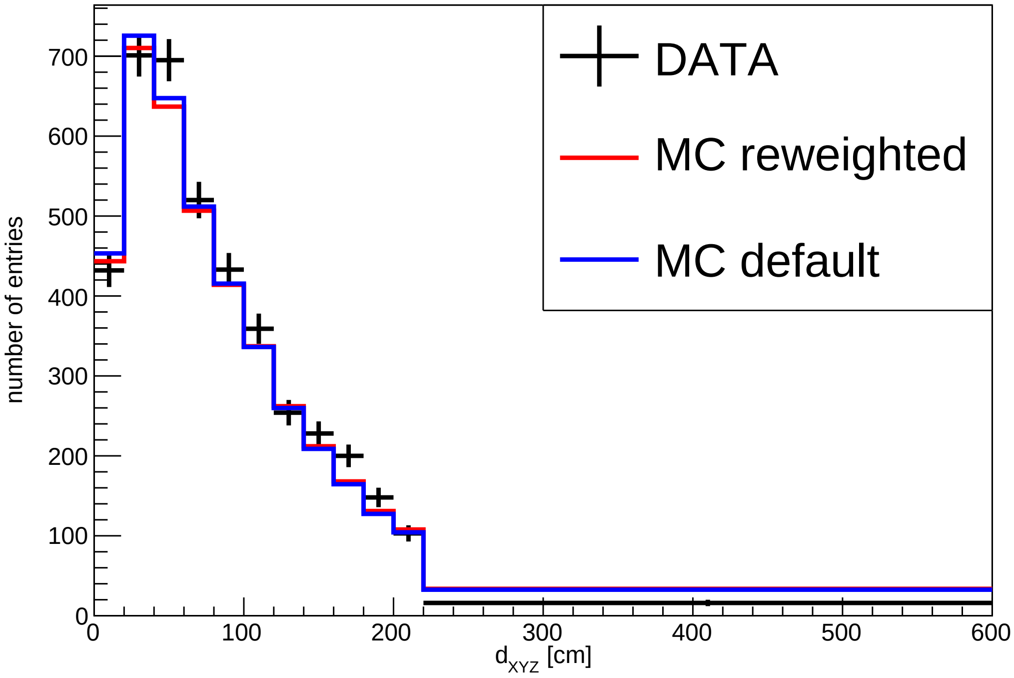

Figure 5.21: d_{XYZ} distribution, data uses SCE correction from anode-cathode-anode crossing maps, while MC uses the input SCE distortion map as in previous histograms.

challenging.

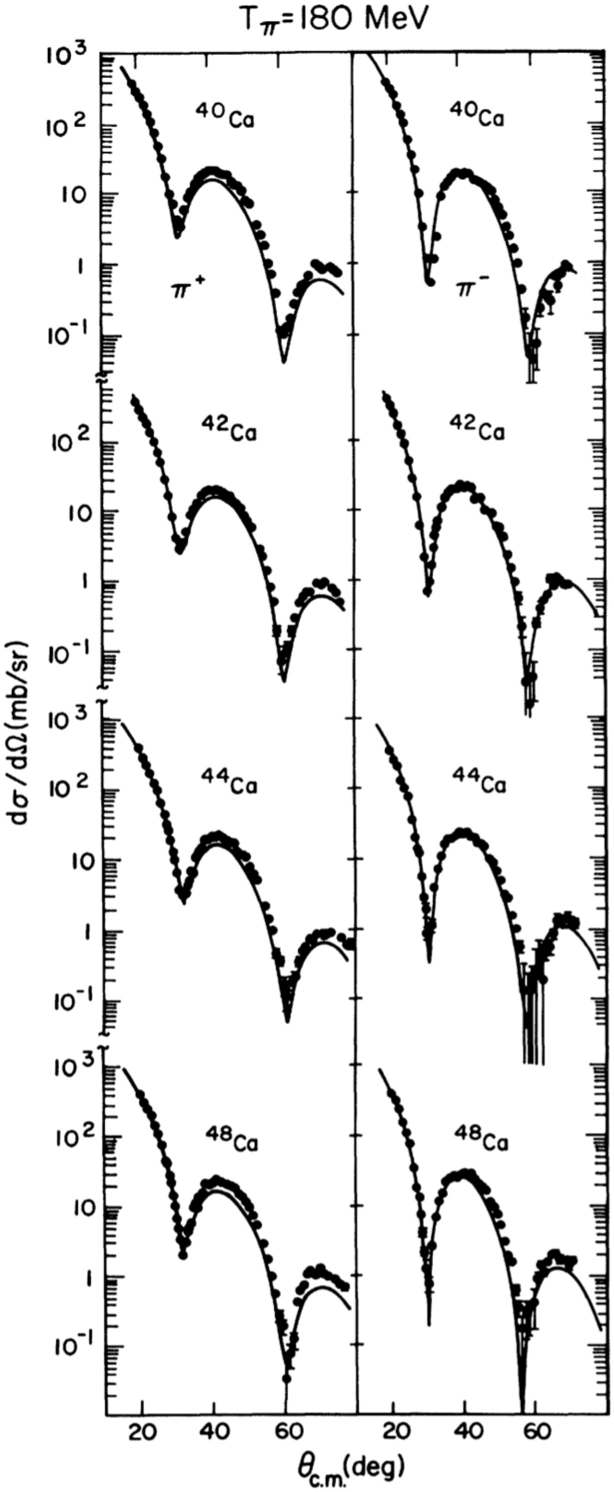

Figure 5.22: Angular distributions for pion-Ca elastic scattering at T=180MeV. Optical potential calculations are represented by solid curves. The figure is taken from[104].

Further, I used the Geant4Reweight framework to estimate the total and reaction cross section simultaneously. I followed a similar procedure as used for measuring the reaction cross section while varying both the reaction and elastic cross section scaling factors simultaneously. Figure 5.23 shows the χ^2-χ^2_{min} as a function of elastic and reaction scaling factors for d_{XYZ} distribution and deflection parameter (b) distribution respectively.

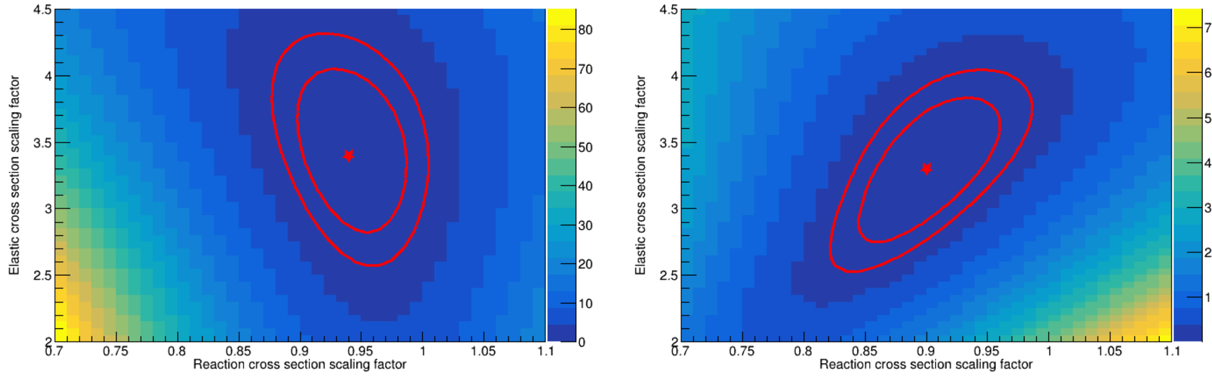

(a) d_{XYZ} parameter

(b) b parameter

Figure 5.23: The color scale shows the χ^2-χ^2_{min} for simultaneous variation of reaction and elastic cross section scaling factors, the left plot is for d_{XYZ} parameter and the right plot is for b parameter. The inner contour represents χ^2-χ^2_{min}=1 and the outer contour represent χ^2-χ^2_{min}=2.3 (68.3% confidence interval).

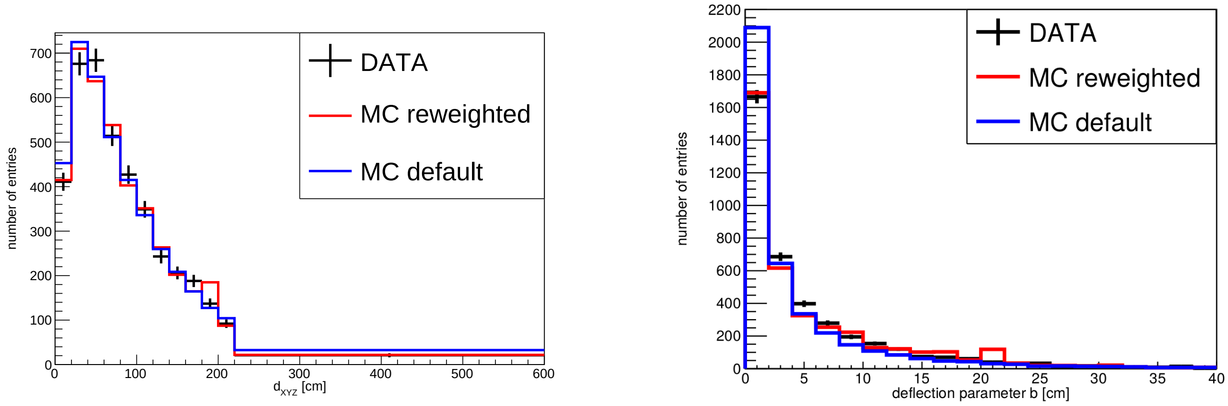

(a) d_{XYZ} parameter

(b) b parameter

Figure 5.24: The left plot is for d_{XYZ} parameter and the right plot is for b parameter the MC reweighted histogram is the best fit for simultaneous variation of reaction and elastic cross section scaling factors.

Figure 5.24 shows the plot of d_{XYZ} and deflection parameter respectively. For the best data/MC agreement, simultaneously varying the scaling factors gives the following results (table 5.4):

Observables used	Reaction cross section scaling factor	Elastic cross section scaling factor
d_{XYZ} parameter	0.94	3.4
deflection parameter (b)	0.90	3.3

Table 5.4: Reaction and elastic cross section scaling factors obtained by simultaneously varying the factors.

As previously discussed the elastic cross section is dominated by low scattering angle interactions which have not been experimentally measured. Using the Geant4Reweight tools, for a reliable measurement of elastic scattering scaling factors we need to use different scaling factors for different scattering angles which is something we plan to do in the future. Conservatively, we set an upper limit of elastic cross section scaling factor to be 3.4 (based on the results of simultaneous variation of scaling factors for d_{XYZ}) to determine the possible systematic error caused by uncertainty in predicted elastic cross section values.

When we set the elastic cross section scaling factor to be 3.4 the reaction cross section scaling factor is 0.94. From the previous discussion for an elastic cross section scaling factor of 1 (default Geant4 prediction), the reaction cross section scaling factor is 0.97. The systematic uncertainty due to elastic cross section is taken to be ±0.03.

5.6 RESULTS:

In this chapter I discussed the Geant4 reweighting technique to measure the π^+-argon total reaction cross section. The study suggests the Geant4 reaction cross section has to be scaled by a factor of 0.97 for MC observables distribution to match data. The result of the study is a reaction cross section scaling factor = 0.97. The uncertainties in measurement are:

Statistical uncertainty, σ_{Stfit}=0.03

Systematic uncertainties:

Due to SCE, σ_{SCE}=0.01

Uncertainty due to muon background fraction, σ_{muonf}=0.01

Uncertainty due to elastic cross section, $\sigma_{elastic}$=0.03

Total systematic uncertainty, $\sigma_{sys} = \sqrt{\sigma^2_{SCE} + \sigma^2_{muonf} + \sigma^2_{elastic}}$=0.033

Total uncertainty, $\sigma_{tot} = \sqrt{\sigma^2_{Stfit} + \sigma^2 sys} = 0.045$

The reaction cross section scaling factor is, 0.97 ± 0.045

The reaction cross section is found to be within 3% of the Geant4 prediction. The study validates the reaction cross section prediction by Geant4. The study is carried out for 1 GeV/c momentum beam π^+ and can be extended to the complete range of beam momentum (1-7 GeV/c) for ProtoDUNE-SP data.

Chapter 6

Conclusion

DUNE is the next-generation neutrino experiment being built with the goal of searching for proton decay and CP violation in the lepton sector which could help understand the dominance of matter over antimatter, detecting neutrinos from supernova bursts, and many more mysterious phenomena. DUNE is planned to begin data taking in 2026 and will consist of 4 massive detectors which will be built in stages. The first of the 4 massive detectors will use liquid argon time projection chamber technology (LArTPC). DUNE is an experiment funded by the US Department of Energy and hosted by Fermi National Accelerator Laboratory near Chicago. Considering the amount of resources and time that will go into DUNE, it was considered necessary to build a prototype of the detector which gave birth to ProtoDUNE-SP and ProtoDUNE-DP detectors. The ProtoDUNE-SP uses the same technology that will be used in the DUNE far detector first module.

The major goals of the ProtoDUNE-SP experiment are to provide a testbed for detector elements and technology that will be eventually used in DUNE, study the detector response for different test beam particles, exhibit long-term stability of the detector and measure hadron-argon cross sections. ProtoDUNE-SP started taking data in Sept 2018 and took beam data for 3 months, while continuing to take cosmic data over an extended period. The detector operated for over 600 days until it was taken down for rerunning with some upgrades. The $\sim$ 600 days of successful operation exhibited the long-term stability of the detector.

ProtoDUNE-SP uses LArTPC detector technology. When a particle passes through the liquid argon it causes ionization producing electron-ion pairs, the electrons drift towards the anode under the action of the electric field applied between the cathode and the anode. The 3D particle trajectory is reconstructed by using the ionization charge collected at the anode. The y and z position of ionization is determined by the location at which electrons are collected at the anode, and the x position of ionization is reconstructed using the signal arrival times and drift velocity. Thus, for a LArTPC, precise measurement of drift velocity is very important for position and energy reconstruction. Space charge effect (SCE), which is the buildup of excess positive charge in a LArTPC over time, distorts the applied drift electric field (consequently drift velocity) in ProtoDUNE-SP. I developed a novel technique to measure the SCE distorted drift velocity using anode-cathode-anode crossing tracks. Track start and endpoints are un-distorted for such tracks. I remove any transverse spatial distortion using an SCE distortion map I developed using anode-cathode-anode tracks. Drift distance for each hit is measured using hit wire position. Local drift velocity is then determined by taking the ratio of the change in drift distance to the change in drift time as a function of drift distance. Electric field variation of within 20 % of the nominal value is observed using this technique.

LArTPC provides excellent position and energy reconstruction of charged particles. The energy reconstruction is carried out based on the charge deposited(dQ/dx). However, factors including Space Charge Effect (SCE), attenuation due to electronegative impurities, diffusion, and inactive wires, lead to non-uniform charge deposition in various parts of the detector. One of the goals of the ProtoDUNE-SP experiment is to understand the detector response for different test beam particles which will be useful for DUNE. For understanding the detector response, we need to calibrate the measured charge into energy. The detector calibration consists of two steps, firstly removing the non-uniformity in charge deposition and secondly determining a calibration factor to convert the charge into energy. I use the detector response for energetic through-going cosmic ray muons as a data-driven correction to remove non-uniformity in dQ/dx. I then perform the energy scale calibration using a sample of stopping cosmic ray muons for which theoretical dE/dx is well known as a function of residual range. In this method, the correction factors to remove non-uniformity in dQ/dx in each part of the detector and in time are calculated. After removing the non-uniformity in charge deposition, dQ/dx is converted to dE/dx using a recombination model with a calibration constant as a free parameter. The final calibration constant is calculated comparing measured dE/dx with theoretical prediction under χ^2 minimization. Cosmic muon-based calibration constants are used for beam p, π^+, K^+, e^+,μ^+ with excellent data-simulation agreement.

ProtoDUNE-SP collected close to three months of test beam data. One of the long-term goals of the ProtoDUNE-SP experiment is to measure the hadron-argon cross sections. Pions are final state products in most neutrino interaction processes including coherent pion production, resonant scattering, deep inelastic scattering. It is very important to model their behavior inside the target nucleus and during its propagation inside the detector medium. Experimental measurements of the pion-argon cross section on Liquid Argon are rare or non-existent. Predictions are made based on the pion-argon cross-section on the heavier and lighter target nucleus. I used the Geant4 reweighting technique to measure the π^+-argon cross section. The π^+-argon reaction cross section measured using the Geant4 reweighting technique is in good agreement with Geant4 π^+-argon cross section prediction. The measured π^+-argon total elastic cross section however does not agree with the Geant4 prediction. We will need to do some more study to better understand the π^+-argon elastic cross section, including a scattering angle-dependent elastic scaling factor. The reaction cross-section study is done for 1 GeV/c momentum beam π^+. The technique could be extended to all available beam momentum (1-7 GeV) in ProtoDUNE-SP. The results of the cross-section study provide important input for various models (such as Geant4, GENIE) used to generate and propagate particles through matter.

My other major contributions in ProtoDUNE-SP include a study of longitudinal diffusion of electrons in liquid argon, wire plane transparency studies, and Cathode Plane Assembly (CPA) misalignment study. The various studies carried out in ProtoDUNE-SP will benefit all LArTPC experiments in general and DUNE in particular.

Bibliography

[1] Mark Thomson. *Modern particle physics*. Cambridge University Press, New York, 2013. ISBN 9781107034266. URL `http://www-spires.fnal.gov/spires/find/books/www?cl=QC793.2.T46::2013`.

[2] Wikipedia. Standard Model, 2021. URL `https://en.wikipedia.org/wiki/Standard_Model`. online accessed 21-Feb-2021.

[3] CERN. The Standard Model. URL `https://home.cern/science/physics/standard-model`.

[4] G. Aad et al. Observation of a new particle in the search for the Standard Model Higgs boson with the ATLAS detector at the LHC. *Physics Letters B*, 716(1):1–29, 2012. ISSN 0370-2693. doi: https://doi.org/10.1016/j.physletb.2012.08.020. URL `https://www.sciencedirect.com/science/article/pii/S037026931200857X`.

[5] S. Chatrchyan et al. Observation of a new boson at a mass of 125 GeV with the CMS experiment at the LHC. *Physics Letters B*, 716(1):30–61, 2012. ISSN 0370-2693. doi: https://doi.org/10.1016/j.physletb.2012.08.021. URL `https://www.sciencedirect.com/science/article/pii/S0370269312008581`.

[6] The DUNE collaboration. An International Experiment for Neutrino Science. URL `https://www.dunescience.org/`. online accessed 21-Feb-2021.

[7] Bruce T. Cleveland, Timothy Daily, Jr. Raymond Davis, James R. Distel, Kenneth Lande, C. K. Lee, Paul S. Wildenhain, and Jack Ullman. Measurement of the Solar Electron Neutrino Flux with the Homestake Chlorine Detector. *The Astrophysical Journal*, 496(1):505–526, mar 1998. doi: 10.1086/305343. URL `https://doi.org/10.1086/305343`.

[8] Wikipedia. Solar neutrino problem. URL https://en.wikipedia.org/wiki/Solar_neutrino_problem. online accessed 21-Feb-2021.

[9] K. S. Hirata et al. Observation of a small atmospheric muon-neutrino / electron-neutrino ratio in Kamiokande. *Phys. Lett. B*, 280:146–152, 1992. doi: 10.1016/0370-2693(92)90788-6.

[10] Herbert H. Chen. Direct approach to resolve the solar-neutrino problem. *Phys. Rev. Lett.*, 55:1534–1536, Sep 1985. doi: 10.1103/PhysRevLett.55.1534. URL https://link.aps.org/doi/10.1103/PhysRevLett.55.1534.

[11] M. Tanabashi et al. Review of Particle Physics. *Phys. Rev. D*, 98:030001, Aug 2018. doi: 10.1103/PhysRevD.98.030001. URL https://link.aps.org/doi/10.1103/PhysRevD.98.030001.

[12] Don Lincoln. Neutrinos: Majorana or dirac?, 2012. URL https://news.fnal.gov/2012/09/neutrinos-majorana-or-dirac/. online accessed 24-Feb-2021.

[13] NBC News. Sterile neutrinos, 2018. URL https://www.nbcnews.com/mach/science/major-physics-experiment-just-detected-particle-shouldn-t-exist-ncna879616. online accessed 24-Feb-2021.

[14] Wikipedia. Sterile neutrinos, 2021. URL https://en.wikipedia.org/wiki/Sterile_neutrino. online accessed 21-Feb-2021.

[15] C Athanassopoulos, L.B Auerbach, D Bauer, R.D Bolton, R.L Burman, I Cohen, D.O Caldwell, B.D Dieterle, J.B Donahue, A.M Eisner, and et al. The liquid scintillator neutrino detector and LAMPF neutrino source. *Nuclear Instruments and Methods in Physics Research Section A: Accelerators, Spectrometers, Detectors and Associated Equipment*, 388(1-2):149172, Mar 1997. ISSN 0168-9002. doi: 10.1016/s0168-9002(96)01155-2. URL http://dx.doi.org/10.1016/S0168-9002(96)01155-2.

[16] A.A. Aguilar-Arevalo, B.C. Brown, L. Bugel, G. Cheng, J.M. Conrad, R.L. Cooper, R. Dharmapalan, A. Diaz, Z. Djurcic, D.A. Finley, and et al. Significant excess of elec-

tronlike events in the miniboone short-baseline neutrino experiment. *Physical Review Letters*, 121(22), Nov 2018. ISSN 1079-7114. doi: 10.1103/physrevlett.121.221801. URL http://dx.doi.org/10.1103/PhysRevLett.121.221801.

[17] J. H. Christenson, J. W. Cronin, V. L. Fitch, and R. Turlay. Evidence for the 2π decay of the k_2^0 meson. *Phys. Rev. Lett.*, 13:138–140, Jul 1964. doi: 10.1103/PhysRevLett.13.138. URL https://link.aps.org/doi/10.1103/PhysRevLett.13.138.

[18] CP violation. URL https://www.nevis.columbia.edu/daedalus/motiv/cp.html. online accessed 21-Feb-2021.

[19] K. Abe et al. Constraint on the matter-antimatter symmetry-violating phase in neutrino oscillations. *Nature*, 580(7803):339–344, 2020. ISSN 1476-4687. doi: 10.1038/s41586-020-2177-0. URL https://doi.org/10.1038/s41586-020-2177-0.

[20] Hyper-Kamiokande. Neutrino Mass Hierarchy. URL http://www.hyper-k.org/en/physics/phys-hierarchy.html. online accessed 21-Feb-2021.

[21] C. Andreopoulos, A. Bell, D. Bhattacharya, F. Cavanna, J. Dobson, S. Dytman, H. Gallagher, P. Guzowski, R. Hatcher, P. Kehayias, A. Meregaglia, D. Naples, G. Pearce, A. Rubbia, M. Whalley, and T. Yang. The GENIE Neutrino Monte Carlo Generator, 2009.

[22] S. Agostinelli et al. GEANT4–a simulation toolkit. *Nucl. Instrum. Meth. A*, 506: 250–303, 2003. doi: 10.1016/S0168-9002(03)01368-8.

[23] CERN. FLUKA. URL https://fluka.cern/. online accessed 02-MAR-2021.

[24] Elena Gramellini. *Measurement of the Negative Pion and Positive Kaon Total Hadronic Cross Sections on Argon at the LArIAT Experiment*. PhD thesis, Yale U., 2018. URL http://lss.fnal.gov/archive/thesis/2000/fermilab-thesis-2018-24.pdf.

[25] Gregory Pulliam. *π^+ Cross Section on Argon for the LArIAT Experiment*. PhD

thesis, Syracuse U., 2019. URL http://lss.fnal.gov/archive/thesis/2000/fermilab-thesis-2019-10.pdf.

[26] B. Abi et al. First results on ProtoDUNE-SP liquid argon time projection chamber performance from a beam test at the CERN Neutrino Platform. *JINST*, 15:P12004, 2020. doi: 10.1088/1748-0221/15/12/P12004.

[27] A. S. Carroll, I. H. Chiang, C. B. Dover, T. F. Kycia, K. K. Li, P. O. Mazur, D. N. Michael, P. M. Mockett, D. C. Rahm, and R. Rubinstein. Pion-nucleus total cross sections in the (3,3) resonance region. *Phys. Rev. C*, 14:635–638, Aug 1976. doi: 10.1103/PhysRevC.14.635. URL https://link.aps.org/doi/10.1103/PhysRevC.14.635.

[28] D Ashery. Pion nucleus reactions. *Nuclear Physics A354pp555c-576c.*

[29] D. Ashery, I. Navon, G. Azuelos, H. K. Walter, H. J. Pfeiffer, and F. W. Schlepütz. True absorption and scattering of pions on nuclei. *Phys. Rev. C*, 23:2173–2185, May 1981. doi: 10.1103/PhysRevC.23.2173. URL https://link.aps.org/doi/10.1103/PhysRevC.23.2173.

[30] A. Saunders, S. Høibråten, J. J. Kraushaar, B. J. Kriss, R. J. Peterson, R. A. Ristinen, J. T. Brack, G. Hofman, E. F. Gibson, and C. L. Morris. Reaction and total cross sections for low energy π^+ and π^- on isospin zero nuclei. *Phys. Rev. C*, 53:1745–1752, Apr 1996. doi: 10.1103/PhysRevC.53.1745. URL https://link.aps.org/doi/10.1103/PhysRevC.53.1745.

[31] H.J. Wenzel. G4HadStudies. URL https://github.com/hanswenzel/G4HadStudies.

[32] Babak Abi et al. Volume I. Introduction to DUNE. *JINST*, 15(08):T08008, 2020. doi: 10.1088/1748-0221/15/08/T08008.

[33] Babak Abi et al. Deep Underground Neutrino Experiment (DUNE), Far Detector Technical Design Report, Volume II DUNE Physics. 2 2020.

[34] Babak Abi et al. Volume III. DUNE far detector technical coordination. *JINST*, 15 (08):T08009, 2020. doi: 10.1088/1748-0221/15/08/T08009.

[35] Babak Abi et al. Volume IV. The DUNE far detector single-phase technology. *JINST*, 15(08):T08010, 2020. doi: 10.1088/1748-0221/15/08/T08010.

[36] B. Abi et al. The Single-Phase Technical Design Report. 2017.

[37] B. Abi et al. The DUNE Far Detector Interim Design Report, Volume 3: Dual-Phase Module, 2018.

[38] CERN. Charge readout and dual-phase readout technology for large scale cryogenic liquid detectors. URL `https://twiki.cern.ch/twiki/bin/view/AIDA2020WP8/ChargeReadout`. online accessed 27-Feb-2021.

[39] S. Amerio et al. Design, construction and tests of the ICARUS T600 detector. *Nucl. Instrum. Meth. A*, 527:329–410, 2004. doi: 10.1016/j.nima.2004.02.044.

[40] C Anderson, M Antonello, B Baller, T Bolton, C Bromberg, F Cavanna, E Church, D Edmunds, A Ereditato, S Farooq, and et al. The ArgoNeuT detector in the NuMI low-energy beam line at Fermilab. *Journal of Instrumentation*, 7(10):P10019P10019, Oct 2012. ISSN 1748-0221. doi: 10.1088/1748-0221/7/10/p10019. URL `http://dx.doi.org/10.1088/1748-0221/7/10/P10019`.

[41] R. Acciarri et al. The Liquid Argon In A Testbeam (LArIAT) experiment. *Journal of Instrumentation*, 15(04):P04026–P04026, apr 2020. doi: 10.1088/1748-0221/15/04/p04026. URL `https://doi.org/10.1088/1748-0221/15/04/p04026`.

[42] R. Acciarri et al. "design and construction of the MicroBooNE detector". *Journal of Instrumentation*, 12(02):P02017–P02017, feb 2017. doi: 10.1088/1748-0221/12/02/p02017. URL `https://doi.org/10.1088/1748-0221/12/02/p02017`.

[43] Matthew Chalmers and Stefania Pandolfi. Reporting on international high-energy

physics, 2016. URL https://cerncourier.com/a/neutrinos-take-centre-stage/. online accessed 28-Feb-2021.

[44] D Montanari, J Bremer, A Gendotti, M Geynisman, S Hentschel, T Loew, D Mladenov, C Montanari, S Murphy, M Nessi, B Norris, F Noto, A Rubbia, R Sharma, D Smargianaki, J Stewart, C Vignoli, P Wilson, and S Wu. Development of membrane cryostats for large liquid argon neutrino detectors. *IOP Conference Series: Materials Science and Engineering*, 101:012049, dec 2015. doi: 10.1088/1757-899x/101/1/012049. URL https://doi.org/10.1088/1757-899x/101/1/012049.

[45] Noble P G 2009 A short history of LNG shipping 1959-2009, Texas Section, SNAME.

[46] D Montanari, J Bremer, A Gendotti, M Geynisman, S Hentschel, T Loew, D Mladenov, C Montanari, S Murphy, M Nessi, B Norris, F Noto, A Rubbia, R Sharma, D Smargianaki, J Stewart, C Vignoli, P Wilson, and S Wu. Development of membrane cryostats for large liquid argon neutrino detectors. *IOP Conference Series: Materials Science and Engineering*, 101:012049, dec 2015. doi: 10.1088/1757-899x/101/1/012049. URL https://doi.org/10.1088/1757-899x/101/1/012049.

[47] Jonathan Asadi. Liquid argon time projection chambers, 2017. URL https://npc.fnal.gov/wp-content/uploads/2017/06/NuPhysSymposium_Asaadi.pdf. online; accessed 02-Mar-2019.

[48] P. Benetti et al. Argon purification in the liquid phase. *Nucl. Instrum. Meth. A*, 333: 567–570, 1993. doi: 10.1016/0168-9002(93)91209-6.

[49] Wikipedia. Time Projection Chamber. URL https://en.wikipedia.org/wiki/Time_projection_chamber. online accessed 28-Feb-2021.

[50] Carlo Rubia. The Liquid-Argon Time Projection Chamber:A New Concept For Neutrino Detectors, 1977. URL https://lartpc-docdb.fnal.gov/cgi-bin/ShowDocument?docid=7. online accessed 28-Feb-2021.

[51] S. Amoruso et al. Study of electron recombination in liquid argon with the icarus tpc. *Nucl. Instrum. Meth. A*, 523:275–286, 2004. doi: 10.1016/j.nima.2003.11.423.

[52] G Giacomelli. The CNGS neutrino beam. *Journal of Physics: Conference Series*, 116: 012004, jun 2008. doi: 10.1088/1742-6596/116/1/012004. URL `https://doi.org/10.1088/1742-6596/116/1/012004`.

[53] Fabio Acerbi and Stefan Gundacker. Understanding and simulating SiPMs. *Nucl. Instrum. Meth. A*, 926:16–35, 2019. doi: 10.1016/j.nima.2018.11.118.

[54] R. Herbst et al. Design of the SLAC RCE Platform: A general purpose ATCA based data acquisition system. In *2014 IEEE Nuclear Science Symposium and Medical Imaging Conference and 21st Symposium on Room-Temperature Semiconductor X-ray and Gamma-ray Detectors*, page 7431254, 2016. doi: 10.1109/NSSMIC.2014.7431254.

[55] Tsang, K.V., Convery, M., Graham, M., Herbst, R., and Russell, J. The SLAC RCE Platform for ProtoDUNE. *EPJ Web Conf.*, 214:01025, 2019. doi: 10.1051/epjconf/201921401025. URL `https://doi.org/10.1051/epjconf/201921401025`.

[56] J. Anderson, K. Bauer, A. Borga, H. Boterenbrood, H. Chen, K. Chen, G. Drake, M. Dnszelmann, D. Francis, D. Guest, B. Gorini, M. Joos, F. Lanni, G. Lehmann Miotto, L. Levinson, J. Narevicius, W. Panduro Vazquez, A. Roich, S. Ryu, F. Schreuder, J. Schumacher, W. Vandelli, J. Vermeulen, D. Whiteson, W. Wu, and J. Zhang. FELIX: a PCIe based high-throughput approach for interfacing front-end and trigger electronics in the ATLAS Upgrade framework. *Journal of Instrumentation*, 11(12):C12023–C12023, dec 2016. doi: 10.1088/1748-0221/11/12/c12023. URL `https://doi.org/10.1088/1748-0221/11/12/c12023`.

[57] A. Borga, E. Church, F. Filthaut, E. Gamberini, P. de Jong, G. Lehmann Miotto, F. Schreuder, J. Schumacher, R. Sipos, M. Vermeulen, K. Wierman, and L. Wood. Felix-based readout of the single-phase protodune detector. *IEEE Transactions on Nuclear Science*, 66(7):993–997, 2019. doi: 10.1109/TNS.2019.2904660.

[58] J. S. Marshall and M. A. Thomson. The Pandora Software Development Kit for Pattern Recognition. *Eur. Phys. J.*, C75(9):439, 2015. doi: 10.1140/epjc/s10052-015-3659-3.

[59] R. Acciarri et al. The Pandora multi-algorithm approach to automated pattern recognition of cosmic-ray muon and neutrino events in the MicroBooNE detector. *Eur. Phys. J.*, C78(1):82, 2018. doi: 10.1140/epjc/s10052-017-5481-6.

[60] N. Charitonidis and I. Efthymiopoulos. Low energy tertiary beam line design for the CERN neutrino platform project. *Phys. Rev. Accel. Beams*, 20:111001, Nov 2017. doi: 10.1103/PhysRevAccelBeams.20.111001. URL `https://link.aps.org/doi/10.1103/PhysRevAccelBeams.20.111001`.

[61] A. C. Booth, N. Charitonidis, P. Chatzidaki, Y. Karyotakis, E. Nowak, I. Ortega-Ruiz, M. Rosenthal, and P. Sala. Particle production, transport, and identification in the regime of $1-7\ \mathrm{GeV}/c$. *Phys. Rev. Accel. Beams*, 22:061003, Jun 2019. doi: 10.1103/PhysRevAccelBeams.22.061003. URL `https://link.aps.org/doi/10.1103/PhysRevAccelBeams.22.061003`.

[62] LArSoft collaboration, Software for LArTPCs, . URL `https://larsoft.org/`. online accessed 28-Feb-2021.

[63] ROOT data analysis framework. URL `https://root.cern.ch/`. online accessed 28-Feb-2021.

[64] The art Event Processing Framework. URL `http://art.fnal.gov/`. online accessed 28-Feb-2021.

[65] Jerome Verbeke Doug Wright Chris Hagmann, David Lange. Proton-induced Cosmic-ray Cascades in the Atmosphere. URL `https://nuclear.llnl.gov/simulation/doc_cry_v1.7/cry.pdf`.

[66] D. Heck, J. Knapp, J. N. Capdevielle, G. Schatz, and T. Thouw. CORSIKA: A Monte Carlo code to simulate extensive air showers. 2 1998.

[67] S. Agostinelli et al. Geant4a simulation toolkit. *Nuclear Instruments and Methods in Physics Research Section A: Accelerators, Spectrometers, Detectors and Associated Equipment*, 506(3):250–303, 2003. ISSN 0168-9002. doi: https://doi.org/10.1016/S0168-9002(03)01368-8. URL https://www.sciencedirect.com/science/article/pii/S0168900203013688.

[68] General Geometry Description (GGD). URL https://github.com/brettviren/gegede. online accessed 28-Feb-2021.

[69] J. B. Birks. The Theory and practice of scintillation counting, 1964. URL http://www.slac.stanford.edu/spires/find/books/www?cl=QCD928:B52.

[70] M Szydagis, N Barry, K Kazkaz, J Mock, D Stolp, M Sweany, M Tripathi, S Uvarov, N Walsh, and M Woods. NEST: a comprehensive model for scintillation yield in liquid xenon. *Journal of Instrumentation*, 6(10):P10002–P10002, oct 2011. doi: 10.1088/1748-0221/6/10/p10002. URL https://doi.org/10.1088/1748-0221/6/10/p10002.

[71] C. Adams, M. Alrashed, R. An, J. Anthony, J. Asaadi, A. Ashkenazi, S. Balasubramanian, B. Baller, C. Barnes, G. Barr, and et al. Calibration of the charge and energy loss per unit length of the MicroBooNE liquid argon time projection chamber using muons and protons. *Journal of Instrumentation*, 15(03):P03022P03022, Mar 2020. ISSN 1748-0221. doi: 10.1088/1748-0221/15/03/p03022. URL http://dx.doi.org/10.1088/1748-0221/15/03/P03022.

[72] Cosmic rays at the surface. URL https://pdg.lbl.gov/2011/reviews/rpp2011-rev-cosmic-rays.pdf.

[73] W. Walkowiak. "drift velocity of free electrons in liquid argon". *Nucl. Instrum. Meth. A*, 449:288–294, 2000. doi: 10.1016/S0168-9002(99)01301-7.

[74] LArSoft collaboration. Drift velocity as a function of electric field and temperature, . URL https://nusoft.fnal.gov/larsoft/doxsvn/html/classdetinfo_1_1DetectorPropertiesStandard.html#a21a284c550d2f03bc193b1b43ab8e13e.

[75] T.J. Lewis H. Dey. Ion mobility and liquid motion in liquefied argon. *J.Phys. D:Applied Physics*, 1:1068, 1968.

[76] M. Torti. Search for space charge effects in the ICARUS T600 LAR-TPC. *Poster at the 4thInternational Conference on New Frontiers in Physics*, 2015.

[77] R. Santorelli, S. di Luise, E. Sanchez Garcia, P. Garcia Abia, T. Lux, V. Pesudo, and L. Romero. Impact of the positive ion current on large size neutrino detectors and delayed photon emission. *Journal of Instrumentation*, 13(04):C04015C04015, Apr 2018. ISSN 1748-0221. doi: 10.1088/1748-0221/13/04/c04015. URL `http://dx.doi.org/10.1088/1748-0221/13/04/C04015`.

[78] L. Onsager. Initial recombination of ions. *Phys. Rev.*, 54:554–557, Oct 1938. doi: 10.1103/PhysRev.54.554. URL `https://link.aps.org/doi/10.1103/PhysRev.54.554`.

[79] R. Acciarri et al. A study of electron recombination using highly ionizing particles in the ArgoNeuT liquid argon TPC. *Journal of Instrumentation*, 8(08):P08005–P08005, aug 2013. doi: 10.1088/1748-0221/8/08/p08005. URL `https://doi.org/10.1088/1748-0221/8/08/p08005`.

[80] J. B. Birks. Scintillations from Organic Crystals: Specific Fluorescence and Relative Response to Different Radiations. *Proc. Phys. Soc. A*, 64:874–877, 1951. doi: 10.1088/0370-1298/64/10/303.

[81] Paticle Data Group. Atomic and nuclear properties of liquid argon. URL `https://pdg.lbl.gov/2020/AtomicNuclearProperties/HTML/liquid_argon.html`.

[82] ROOT-CERN. Convoluted Landau and Gaussian Fitting Function. URL `https://root.cern.ch/root/html/tutorials/fit/langaus.C.html`.

[83] R. Acciarri et al. Design and construction of the MicroBooNE detector. *Journal of Instrumentation*, 12(02):P02017–P02017, feb 2017. doi: 10.1088/1748-0221/12/02/p02017. URL `https://doi.org/10.1088/1748-0221/12/02/p02017`.

[84] Pedro A.N. Machado, Ornella Palamara, and David W. Schmitz. The Short-Baseline Neutrino Program at Fermilab. *Annual Review of Nuclear and Particle Science*, 69(1): 363387, Oct 2019. ISSN 1545-4134. doi: 10.1146/annurev-nucl-101917-020949. URL http://dx.doi.org/10.1146/annurev-nucl-101917-020949.

[85] Sandro Palestini, Kirk T. McDonald. Space charge in ionization detectors. URL https://physics.princeton.edu//~mcdonald/examples/spacecharge.pdf.

[86] C. D. Child. Discharge From Hot CaO. *Phys. Rev. (Series I)*, 32:492–511, May 1911. doi: 10.1103/PhysRevSeriesI.32.492. URL https://link.aps.org/doi/10.1103/PhysRevSeriesI.32.492.

[87] Irving Langmuir. The effect of space charge and residual gases on thermionic currents in high vacuum. *Phys. Rev.*, 2:450–486, Dec 1913. doi: 10.1103/PhysRev.2.450. URL https://link.aps.org/doi/10.1103/PhysRev.2.450.

[88] Liquid Argon Properties, . URL http://atlas.web.cern.ch/Atlas/GROUPS/LIQARGEXT/TDR/html.1812/LARG-TDR-690.html.

[89] J. S. Marshall and M. A. Thomson. The pandora software development kit for pattern recognition. *The European Physical Journal C*, 75(9), Sep 2015. ISSN 1434-6052. doi: 10.1140/epjc/s10052-015-3659-3. URL http://dx.doi.org/10.1140/epjc/s10052-015-3659-3.

[90] E. L. Snider and G. Petrillo. LArSoft: Toolkit for Simulation, Reconstruction and Analysis of Liquid Argon TPC Neutrino Detectors. *J. Phys. Conf. Ser.*, 898(4):042057, 2017. doi: 10.1088/1742-6596/898/4/042057.

[91] P. Abratenko et al. Measurement of space charge effects in the MicroBooNE LArTPC using cosmic muons. *Journal of Instrumentation*, 15(12):P12037–P12037, dec 2020. doi: 10.1088/1748-0221/15/12/p12037. URL https://doi.org/10.1088/1748-0221/15/12/p12037.

[92] C. Adams et al. A method to determine the electric field of liquid argon time projection chambers using a UV laser system and its application in MicroBooNE. *Journal of Instrumentation*, 15(07):P07010–P07010, jul 2020. doi: 10.1088/1748-0221/15/07/p07010. URL https://doi.org/10.1088/1748-0221/15/07/p07010.

[93] Wikipedia. Uncertainty in median. URL https://en.wikipedia.org/wiki/Median#Sampling_distribution.

[94] CERN-ROOT. Quantiles of a distribution. URL https://root.cern.ch/root/html524/TMath.html#TMath:Quantiles.

[95] F. Cavanna et al. Report for the SPSC Annual Review - 2019, 2019. URL https://cds.cern.ch/record/2669536/files/SPSC-SR-252.pdf.

[96] LArSoft. BackTracker Service Class Reference. URL https://nusoft.fnal.gov/larsoft/doxsvn/html/classcheat_1_1BackTrackerService.html.

[97] A. Reynolds. *Evaluating the low-energy response of the ProtoDUNE-SP detector using Michel electrons.* PhD thesis, University of Oxford, 2020.

[98] Oscar Miyamoto Gomez. Speak physics: What is a cross section? URL https://www.symmetrymagazine.org/article/speak-physics-what-is-a-cross-section.

[99] J. Calcutt. Geant4Reweight For ProtoDUNE-SP, 2020. URL https://indico.fnal.gov/event/24286/contributions/76084/attachments/47348/56838/Geant4Reweight_for_ProtoDUNE.pdf.

[100] Nikolaos Charitonidis, Ilias Efthymiopoulos, and Yannis Karyotakis. Beam performance and instrumentation studies for the ProtoDUNE-DP experiment of CENF. Technical Report CERN-ACC-NOTE-2016-0052. 27, CERN, Geneva, Jul 2016. URL https://cds.cern.ch/record/2202366. Comments: CERN ATS Note.

[101] G. Bohm and G. Zech. Statistics of weighted poisson events and its applications. *Nuclear Instruments and Methods in Physics Research Section A: Accelerators, Spec-*

trometers, Detectors and Associated Equipment, 748:16, Jun 2014. ISSN 0168-9002. doi: 10.1016/j.nima.2014.02.021. URL http://dx.doi.org/10.1016/j.nima.2014.02.021.

[102] B. Efron. Bootstrap Methods: Another Look at the Jackknife. *The Annals of Statistics*, 7(1):1 – 26, 1979. doi: 10.1214/aos/1176344552. URL https://doi.org/10.1214/aos/1176344552.

[103] W.H. Press et al. *Numerical Recipes in C.* Cambridge University Press, 1992.

[104] K. G. Boyer, W. J. Braithwaite, W. B. Cottingame, S. J. Greene, L. E. Smith, C. Fred Moore, C. L. Morris, H. A. Thiessen, G. S. Blanpied, G. R. Burleson, J. F. Davis, J. S. McCarthy, R. C. Minehart, and C. A. Goulding. Pion elastic and inelastic scattering from ^{40,42,44,48}Ca and ^{54}Fe. *Phys. Rev. C*, 29:182–194, Jan 1984. doi: 10.1103/PhysRevC.29.182. URL https://link.aps.org/doi/10.1103/PhysRevC.29.182.